

GPO PRICE \$ _____

CFSTI PRICE(S) \$ _____

Hard copy (HC) 4.00

Final Report

Microfiche (MF) 175

653 July 65

INFRARED SENSOR FOR APOLLO REENTRY
(1 July 1964 - 30 December 1964)

Contract No. NAS5-9703

Prepared by
WESTINGHOUSE ELECTRIC CORPORATION
Aerospace Division
Baltimore, Maryland

for
NATIONAL AERONAUTICS AND SPACE ADMINISTRATION
Goddard Space Flight Center
Greenbelt, Maryland

FACILITY FORM 602

N66 30289

113

(PAGES)

OR-62570

(NASA OR ORTX OR AD-111-581)

(THRU)

1

(PAGE)

14

(CATEGORY)

Final Report

**INFRARED SENSOR FOR APOLLO REENTRY
(1 July 1964 - 30 December 1964)**

Contract No. NAS5-9703

**Prepared by
WESTINGHOUSE ELECTRIC CORPORATION
Aerospace Division
Baltimore, Maryland**

**for
NATIONAL AERONAUTICS AND SPACE ADMINISTRATION
Goddard Space Flight Center
Greenbelt, Maryland**

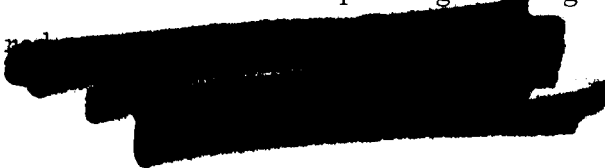


ABSTRACT

30289

When the Apollo reentry vehicle enters the earth's atmosphere with lunar return velocity, the air surrounding the vehicle should ionize to such an extent that radio frequency communications with the ground tracking stations will be seriously impaired during the critical initial phase of deceleration to sub-orbital velocity. Infrared tracking could augment the RF tracking during the blackout period by angle tracking the reentry vehicle induced radiation thereby providing angle position data for immediate reacquisition by the RF tracking systems following blackout. A feasibility study conducted by Goddard Space Flight Center indicated that a combination of airborne, high resolution, passive infrared detection systems would be required to detect the reentry vehicle induced radiation. The objective of this contract was to perform the design studies and develop an engineering model to demonstrate the capabilities of this detection approach.

The design studies consisted of evaluating the components contributing to the reentry induced infrared radiation (surface emission, shock wave radiation ablation product emission) as a function of position along the trajectory. These radiance values were then modified in accordance with the atmospheric attenuation to be encountered from a platform at an altitude of 40,000 feet and look angles from 0 to 30 degrees from the horizontal. Line-of-sight ranges were then derived, and irradiance levels at the plane of the detection system were computed. Within this report sources of background interference are analyzed and suppression techniques evaluated. System design considerations peculiar to the reentry detection problem and discrimination logic are discussed. The hardware comprising the engineering model is described and its measurement



The pertinent results of this effort are:

- a. The maximum line-of-sight range at reentry is 1062 kilometers corresponding to a ground range of 564 nautical miles.
- b. The detection sensitivity required is $2 \times 10^{-12} \text{ w/cm}^2$ in the 2- to 3-micron band.
- c. Digital space correlation is the preferred background discrimination technique.
- d. The engineering model sensitivity was measured to be $2 \times 10^{-13} \text{ w/cm}^2$ which is sufficient to meet the requirement in (b) above with a large enough S/N to ensure high probability of detection at a low false-alarm rate.
- e. The engineering model proves the possibility of realizing high resolution infrared systems comprised of detector arrays, molecular amplifiers, and commutator sampling.

TABLE OF CONTENTS

<u>Section</u>	<u>Page</u>
1 INTRODUCTION	1-1
2 DESIGN SPECIFICATIONS	2-1
3 TARGET DEFINITION	3-1
3.1 Reentry Radiation	3-1
3.1.1 Surface Emission	3-3
3.1.2 Shock Wave Radiation	3-16
3.1.3 Ablation Product	3-18
3.2 Atmospheric Transmission	3-22
3.3 Range Relations	3-24
3.4 Infrared Irradiance Levels	3-26
4 BACKGROUND INTERFERENCE	4-1
4.1 Photon Noise	4-1
4.2 Scan Modulation	4-2
4.3 Scanning Noise	4-2
4.4 Background Discrimination Techniques	4-3
4.5 Spatial Discrimination	4-4
4.6 Digital Space Correlation	4-7
5 DESIGN CONSIDERATIONS	5-1
5.1.1 Concept of Operation	5-1
5.1.2 Practical Considerations	5-4
5.1.3 Multiple Thresholds	5-5
5.1.4 Series-Parallel Processing	5-7

<u>Section</u>	<u>Page</u>
5.1.5 False Targets	5-10
5.2 Threshold Levels	5-11
5.3 Electronic Filter	5-13
5.3.1 High-Frequency Corner	5-14
5.3.2 Low-Frequency Corner	5-15
5.4 Commutation Limitations	5-17
5.5 Spectral Filtering	5-19
5.6 Detector	5-19
5.7 Sensitivity Prediction	5-20
6 SYSTEM MECHANIZATION	6-1
6.1 Parabola	6-1
6.2 Flat	6-7
6.3 Turntable	6-7
6.4 Spectral Filter	6-7
6.5 Detector	6-7
6.6 Molecular Preamplifiers	6-8
6.7 Commutator	6-16
6.8 Delay Line Logic	6-21
6.8.1 Timing	6-21
6.8.2 Discrimination	6-23
6.9 Miscellaneous	6-25
6.10 Time Relationships	6-25
7 PERFORMANCE	7-1
7.1 Recovery Time	7-1
7.2 Optical Resolution	7-3
7.3 Detector	7-6
7.4 Sensitivity	7-8
7.5 Optical Crosstalk	7-10

<u>Section</u>	<u>Page</u>
7.6 Delay Line Discrimination	7-10
8 NEW TECHNOLOGY	8-1
9 REFERENCES	9-1
10 SYMBOL GLOSSARY	10-1

LIST OF ILLUSTRATIONS

<u>Figure</u>	<u>Page</u>
1 Apollo Vehicle Entry Velocity Profiles	1-2
2 Typical Reentry Trajectories	2-2
3 Apollo Type Reentry Stagnation Point Heating Rates	3-4
4 1959 ARDC Standard Atmospheric Density	3-5
5 Shock Layer Temperature Transition	3-7
6 Equilibrium Radiation	3-9
7 Nonequilibrium Radiation	3-11
8 Apollo Reentry Temperature Profiles	3-13
9 Stagnation Point Radiation	3-14
10 Stagnation Point Radiation	3-15
11 Apollo Vehicle Reentry Radiation	3-22
12 Atmospheric Transmission	3-24
13 Range Geometry	3-25
14 Range Relations	3-26
15 Wavelength Functions	3-28
16 Digital Space Correlation	4-9
17 Space Matrix and Delay Line Concept	5-2
18 Delay Line Logic	5-6
19 Multiple Thresholds	5-7
20 Projecting Cloud Edge	5-8

<u>Figure</u>	<u>Page</u>
21 Series - Parallel Logic	5-10
22 Detection Probability	5-13
23 High-Frequency Criterion	5-15
24 Low Frequency Criterion	5-16
25 Feasibility Model	6-2
26 Feasibility System	6-3
27 Engineering Model Block Diagram	6-4
28 System Wiring Diagram	6-5
29 Radiometer	6-6
30 Array Detector	6-9
31 Detector Electrode Connection	6-10
32 Detector-Amplifier Mount	6-11
33 Molecular Amplifier Schematic	6-13
34 Molecular Amplifier	6-14
35 Commutator Schematic	6-17
36 Commutator Block Diagram	6-19
37 Commutator Timing Diagram	6-21
38 Discrimination Circuit Block Diagram	6-22
39 Timing Diagram of Logic Functions	6-24
40 Discrimination Circuit Schematic	6-27
41 Power Supply Wiring Diagram	6-31
42 Large Signal Recovery Time	7-2
43 Extended Area Recovery Time	7-4
44 Target Stretching	7-5
45 Extended Area Target	7-11
46 Exotic Target	7-12

LIST OF TABLES

<u>Table</u>	<u>Page</u>
1 Ablation Product Radiative Heating Rates	3-20
2 Molecular Amplifier Performance Characteristics	6-15
3 Detector Characteristics	7-7

1. INTRODUCTION

When the Apollo command module enters the Earth's atmosphere from its lunar mission, it must dissipate a considerable amount of kinetic energy (on the order of 27,000 Btu/lb) to land safely. Most of this energy is transformed into heat by compression in the stagnation region. Temperatures in the heat cap become sufficient to cause dissociation and ionization of the surrounding air causing it to become highly conductive resulting in marked attenuation or blackout of RF signals. This is illustrated in figure 1 for some typical re-entry trajectories.

This same phenomenon which severely limits radio communications with the reentry vehicle also manifests itself in the form of infrared radiation. Thus, it was suggested that infrared tracking could augment the RF tracking during the blackout period by angle tracking the reentry vehicle induced radiation and thereby provide angle position data for immediate reacquisition by the RF tracking systems following blackout (reference 1). An infrared system could therefore assist in the ground support of the reentering Apollo vehicle if it could detect the radiation induced by the vehicle during those portions of the trajectory where RF blackout occurs.

A feasibility study was conducted by Goddard Space Flight Center which indicated that a high-resolution infrared system on an airborne platform could detect the reentering Apollo vehicle.

The work performed under this contract consisted of making design studies and developing an engineering model to demonstrate the feasibility of this approach. The design analysis and system mechanization are reported herein.

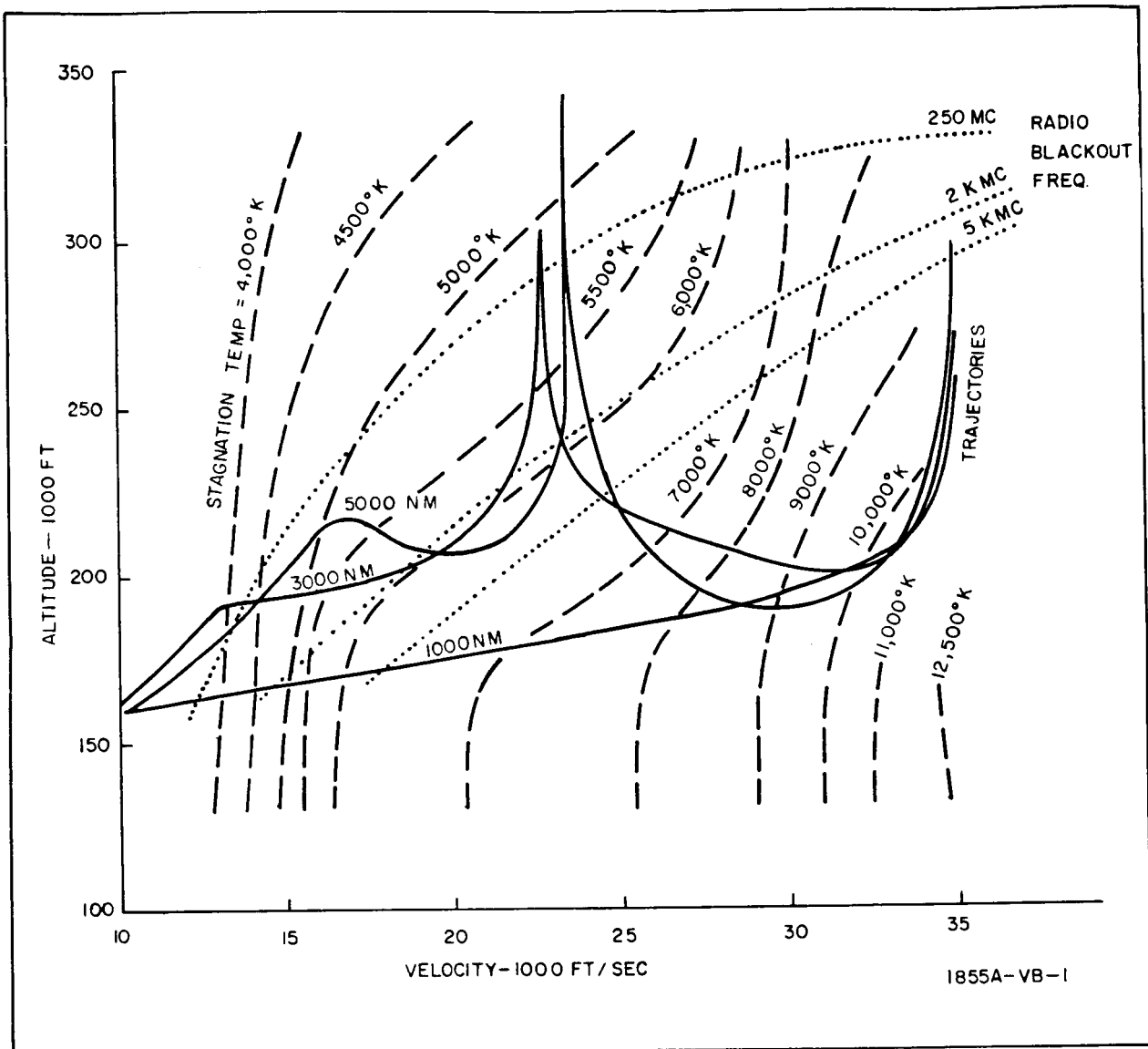


Figure 1. Apollo Vehicle Entry Velocity Profiles

Laboratory performance evaluation of the engineering model indicates that the detection sensitivity required is obtained and that a system comprised of high-resolution detector arrays, molecular amplifiers, and commutation readout techniques is a practical implementation.

2. DESIGN SPECIFICATIONS

The scope of this work was to perform the design studies necessary and to develop a high-resolution infrared scanning system to demonstrate the feasibility of detecting the Apollo vehicle during reentry. A feasibility study conducted at the Goddard Space Flight Center indicated that the major problem to be encountered was that of acquisition against a daylight background. The study further indicated that the most promising solution was in the use of high-resolution detector arrays.

The feasibility model developed under this contract implements these findings and is intended to be used to evaluate the feasibility of the approach. The detection studies conducted in parallel with the model fabrication both amplify and refine problem areas outlined in the study, such as target radiance and atmospheric attenuation.

Specifications peculiar to the model are:

Detector array	-	10 elements
Detector type	-	uncooled PbS
Collector	-	12 inch f/1 reflective
Field of view	-	1 mr/element
Scan rate	-	360 deg/sec azimuth

Additional specifications which were given to assist as a design and study guide are:

Total field of view	-	0 to 30 degrees elevation 360 degrees azimuth
Target altitude	-	300,000 ft
Receiver altitude	-	40,000 ft
Slant range	-	1,000 km

Target area - 10 m^2

Target temperature - $11,000^\circ\text{K}$ max

The trajectory data shown in figures 1 and 2, obtained from references 2 and 3, were also used as typical reentry trajectories.

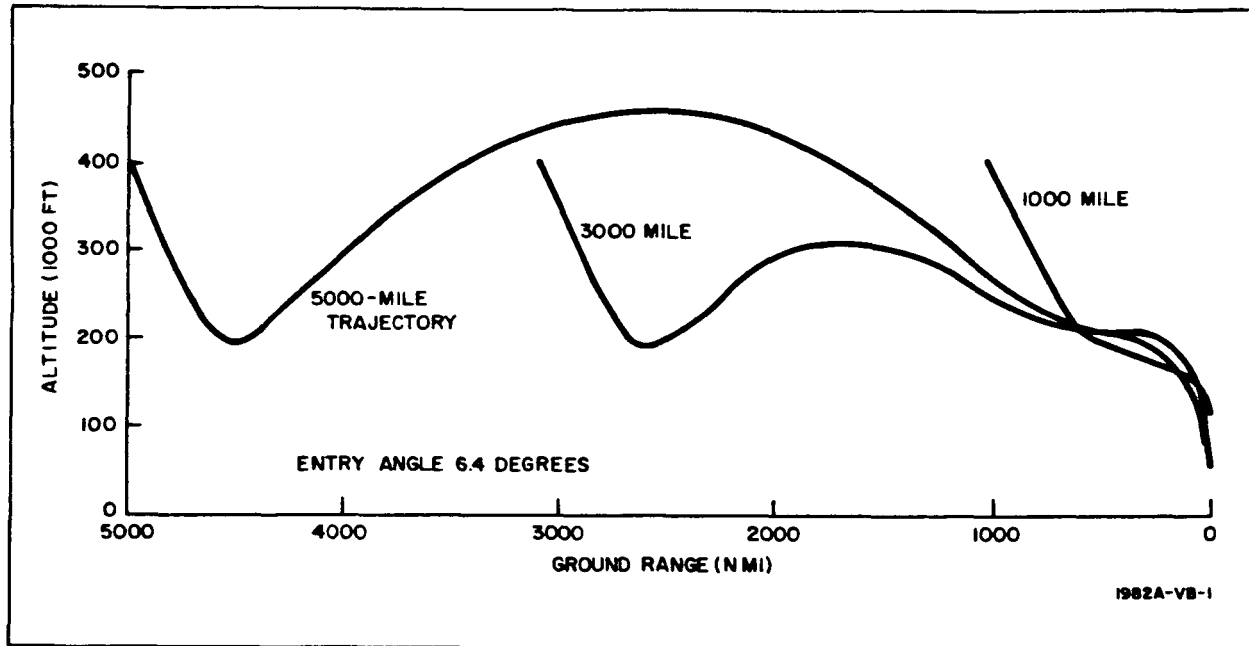


Figure 2. Typical Reentry Trajectories

3. TARGET DEFINITION

The infrared system sensitivity required for the detection of the Apollo vehicle at reentry is established to a large extent by the effective irradiance at the plane of the irdome due to the radiation induced by the reentering Apollo vehicle. Thus, it is necessary to determine the nature of this induced radiation, the path length over which it may be viewed, and the absorption of the intervening atmosphere.

3.1 REENTRY RADIATION

A literature survey was conducted in an effort to obtain the best estimate of reentry radiation. The results of this survey showed that no direct measurements have been made on an actual vehicle for the Apollo vehicle reentry conditions. However, considerable experimental data has been obtained and sufficient theory generated so that a fairly good prediction of the reentry radiation can be made.

There are potentially three interdependent sources of infrared radiation associated with the Apollo vehicle at reentry. They are surface emission, due to vehicular heating, shock wave radiation, and ablation product emission. Of these three, the least certainty is associated with the ablation product emission. This is partly because shock tube tests using the Apollo ablative material either have not been conducted or the data have not been made available at this time. This is not a serious limitation because data have been obtained on a similar material. The major uncertainty is due to the interaction of these three sources with one another and the fact that each scales as a different function of the vehicle diameter. This could lead to a result for full scale entry quite different from that extrapolated from small scale shock tube measurements.

Because of the above uncertainty, the approach taken in this analysis was to establish boundary values for the maximum and minimum infrared radiation that the Apollo vehicle could generate. A typical value based on extrapolations of measurements of similar ablative materials is then compared to the boundary values. This approach yields the maximum and minimum irradiance for evaluating the detection system performance as well as a probable value for typical operation.

The boundary values are established by making certain idealistic assumptions about the Apollo vehicle surface material. The maximum value is obtained by assuming a perfect radiative heat shield wherein all heat inputs are completely absorbed and radiated out. It is assumed that no heat is conducted into the vehicle and that the shield has no thermal capacity. These conditions result in an equilibrium temperature which is quite high and constitutes the "hottest" target possible. The minimum value is obtained by assuming a perfect ablative heat shield wherein all heat inputs are absorbed until the surface reaches 1000°K at which time the material ablates trading mass for thermal energy with no further increase in surface temperature and no re-radiation by the ablative products. Thus, the temperature of the minimum target would not exceed 1000°K .

Of course, neither of these idealistic heat shields exists in theory or practice but they do represent limiting characteristics of the ablative process. As the Apollo vehicle enters the atmosphere, the heating process commences and the surface temperature rises. When it reaches ablation temperature, further heat inputs are absorbed in changing the state of the ablation matter, say from solid to gas, which in turn is ejected into the boundary layer and carried away. If this process was ideal, the surface would remain at the ablation temperature. However, it is not ideal as the ablation temperature varies with reentry conditions and the ablation products injected into the boundary layer re-radiate at temperatures ranging from the ablation temperature to the stagnation temperature. Consequently, the infrared radiation can be expected to exceed that based on the ablation

temperature alone once the ablation temperature is reached. As the ablation process proceeds, the ablative material recedes from the surface leaving behind a char. This char acts like a radiative heat shield in that it has low thermal capacity and poor thermal conductivity. Consequently, the char surface becomes hotter than the ablation temperature and radiates away some of the heat input. It is obvious that the equilibrium temperature of the char will not reach that of the ideal radiative heat shield because some of the heat input is absorbed in the ablation process. Consequently, the infrared radiation can be expected to be less than that based on the equilibrium temperature of an ideal radiative heat shield.

The following analysis therefore endeavors to calculate the total heat input due to convective and radiative processes and from this determine the equilibrium temperature. The equilibrium and ablation temperature are then used to compute the boundary infrared radiation limits. The ablation radiation is calculated from extrapolated shock tube test data and represents the probable infrared radiation value. The shock wave is evaluated for its contribution to the infrared radiation and is merely added on to the above values. All calculations are based on stagnation point conditions for the Apollo size vehicle.

3.1.1 Surface Emission

There are two primary sources of heat transfer to a vehicle entering the earth's atmosphere at lunar return velocities. They are convective heating, due to direct contact of the vehicle with air molecules, and radiative heating, due to the high temperature air in the shock wave irradiating the vehicle. These sources are analyzed separately.

3.1.1.1 Convective Heating

Little (reference 4) cites a number of methods for calculating laminar stagnation point convective heating, and points out that most are too unwieldy for approximate heating analyses. He gives as a noteworthy exception the approximation of Lees (reference 5) which has been found to produce results

close to the numerical mean of all methods considered for dissociating gases.

$$q_c = 23.6 \sqrt{\frac{P_\infty}{R_o}} u_\infty^3 \times 10^{-9} \text{ w/cm}^2 \quad (1)$$

This equation was used for calculating the laminar stagnation point convective heating rates for the Apollo size reentry vehicle, and the results are plotted in figure 3.

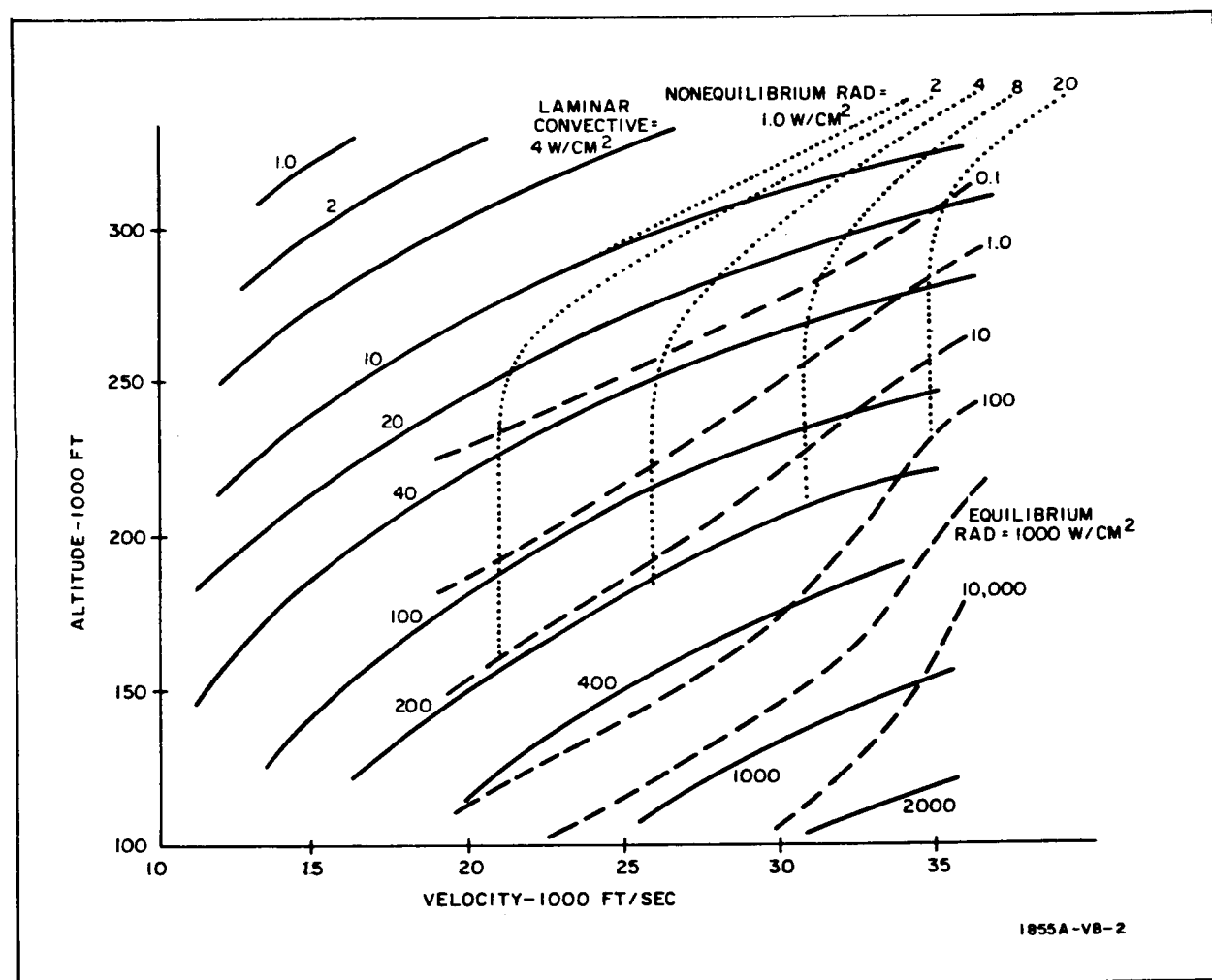


Figure 3. Apollo Type Reentry Stagnation Point Heating Rates

The data in figure 3 have been plotted as a function of altitude and velocity so that the heating rates for any reentry trajectory may be obtained directly.

To perform the calculations it is necessary to know the vehicle nose radius and free-stream density. The nose radius was taken to be 6.5 feet as given in trade magazines for the command module. The free-stream density is based on the 1959 ARDC standard atmosphere and is plotted in figure 4.

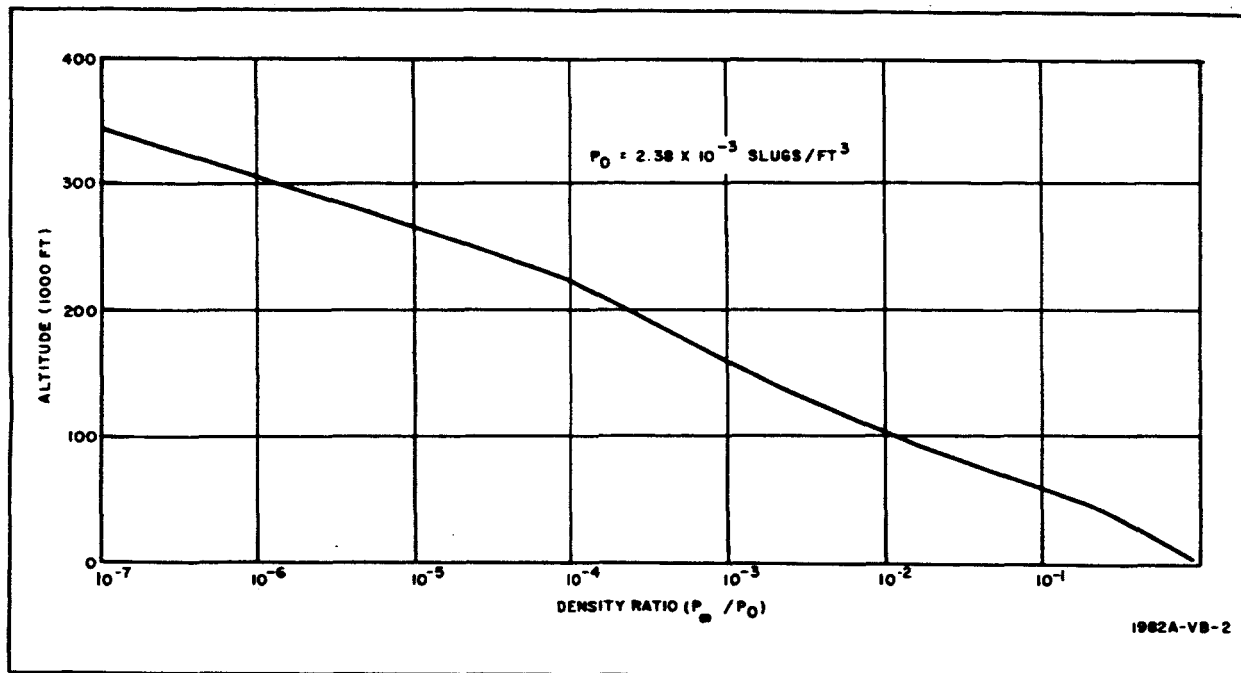


Figure 4. 1959 ARDC Standard Atmospheric Density

A sample calculation is given below.

Given: Altitude = 200,000 ft
 Velocity = 30,000 ft/sec
 $R_o = 6.5$ ft

The free-stream density is obtained by multiplying the sea-level density, $P_0 = 2.38 \times 10^{-3}$ slugs/ft³, by the density ratio, $P_\infty/P_0 = 2.5 \times 10^{-4}$, as read off the curve of figure 4 corresponding to the given altitude of 200,000 feet.

$$P_{\infty} = P_{\infty}/P_0 \times P_0 = 2.5 \times 10^{-4} \times 2.38 \times 10^{-3} = 5.95 \times 10^{-7} \text{ slugs/ft}^3$$

Inserting these values in equation 1 yields the laminar stagnation point convective heat rate for the given conditions.

$$q = 23.6 \sqrt{\frac{5.95 \times 10^{-7}}{6.5}} \times (3 \times 10^4)^3 \times 10^{-9} = 193 \text{ w/cm}^2$$

3.1.1.2 Radiative Heating

Figure 1 shows that the reentering Apollo vehicle will encounter high shock layer temperatures. Thus, the emissivity of heated air becomes significant so that radiative heating from the shock layer becomes an important contributor.

There is a finite time for gas to react chemically to changes in temperature and, although small, is sometimes significant when compared to the time required for gas particles to move through the shock layer of a hypervelocity vehicle. This reaction zone is referred to as a region of nonequilibrium. It constitutes a transition period between air at atmospheric temperature and density to air at shock layer temperature and density equilibrium, and thus exists at the forefront of all hypersonic shock waves.

Page (reference 6) refers to two distances into the forefront of the shock layer (δ_e , the excitation distance and δ_r , the relaxation distance) which describe the depth of the nonequilibrium state. Page describes a model of the nonequilibrium state wherein there exists a temperature overshoot at δ_e resulting in the integral of radiation taken over the distance δ_r being larger than the radiation from an equivalent depth of equilibrium shock layer. Further, his model indicates that the integral of radiation taken over the depth δ_r is a constant independent of density.

Both results are pertinent to any radiative heating analysis as may be better understood from the following relations. Figure 5 illustrates the temperature transition phenomenon as described above. The depth of the shock layer is designated by δ_s and approximated by Page as

$$\delta_s = 3/4 \frac{R_0}{P/P_{\infty}} \quad (2)$$

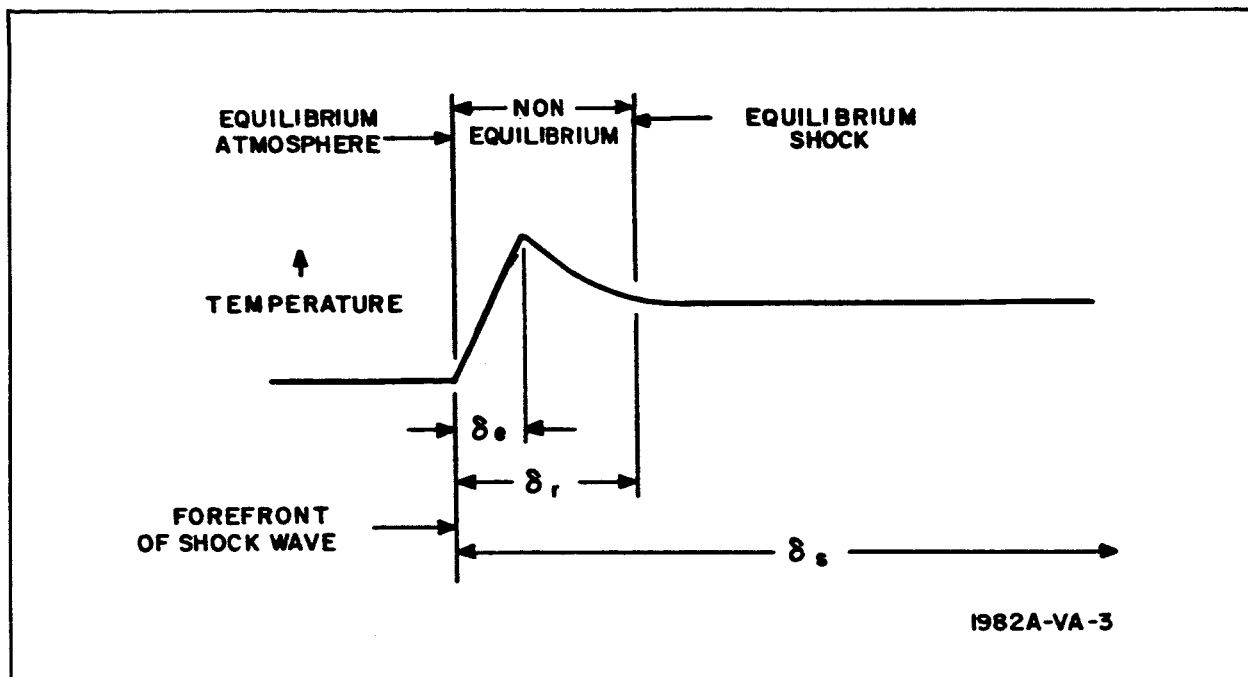


Figure 5. Shock Layer Temperature Transition

It can be seen that δ_s increases with density and size of the vehicle. Inasmuch as the equilibrium radiation is proportional to this depth, it will likewise increase with density and vehicle size. The nonequilibrium radiation in Page's model, however, is fixed and independent of both these factors so long as $\delta_s > \delta_r$. Consequently, if the density and size are such that $\delta_s > \delta_r$, then the equilibrium radiation will constitute the principal source of radiation heating. If, on the other hand, these factors are such that δ_s approaches δ_r , then the nonequilibrium radiation will constitute the principal radiative heating source.

Any excited air which passes completely through the shock layer is expected to be quickly quenched. Therefore, if the flow time from the shock to the stagnation point is less than the relaxation time, the nonequilibrium radiation will be significantly reduced. This effect is called truncation.

In general, as a hypersonic velocity vehicle enters the atmosphere one can expect a nonequilibrium component of radiation to develop which will be an increasing function of density until such a density is reached that the shock layer thickness, δ_s , exceeds the relaxation distance, δ_r . This nonequilibrium component of radiation will then remain constant for all further density increases. However, as the density continues to increase with continual descent in altitude, the shock wave thickness, δ_s will approach in value where the equilibrium radiation equals the nonequilibrium value. Up to the time that this density was approached, the nonequilibrium component of radiation comprised the major source of radiative heating. From this corresponding density on to increasing values (or, conversely, altitude, on to decreasing values), the equilibrium radiation will continue to increase swamp- ing out the fixed nonequilibrium component and thus prevail as the dominant radiative heating source. The magnitude of equilibrium radiation will be an increasing function of vehicle velocity and size. The magnitude of the non- equilibrium component will also be an increasing function of velocity but in- dependent of vehicle size. However, the altitude or density at which the non- equilibrium component reaches full maturity will be a function of vehicle size, since the shock standoff distance is proportioned to vehicle size.

3.1.1.2.1 Equilibrium Radiation - Kivel (reference 7) presents data on the equilibrium radiation of hot air. Figure 6 taken from reference 8 gives the amount of radiation toward a body per cubic centimeter of air as a function of velocity and altitude. Also given is the stagnation point density ratio.

The equilibrium radiation heat rate is computed by selecting the radiation value per cubic centimeter from figure 6 and multiplying this by the shock wave depth as determined from equation 2. These results are also plotted in figure 3.

A sample calculation is given below.

Given: altitude = 200,000 ft
 velocity = 30,000 ft/sec
 $R_o = 6.5$ ft

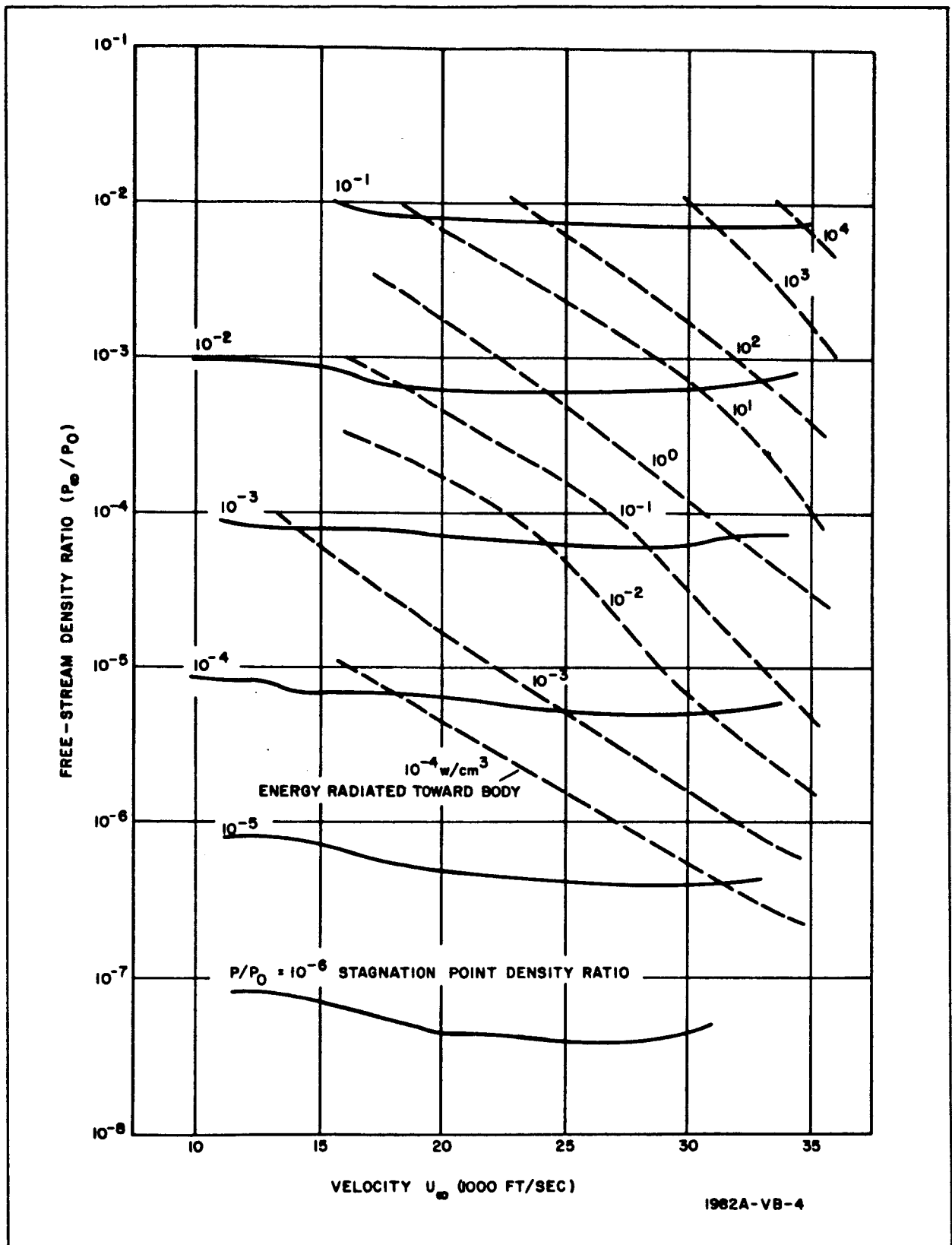


Figure 6. Equilibrium Radiation

The free-stream density ratio corresponding to the given altitude is obtained from figure 4.

$$P_{\infty} / P_o = 2.5 \times 10^{-4}$$

The stagnation point density ratio corresponding to this free-stream density ratio and the given velocity is obtained from figure 6.

$$P/P_o = 4 \times 10^{-3}$$

The ratio of stagnation point density to free-stream density is then

$$P/P_{\infty} = \frac{P}{P_o} \times \frac{P_o}{P_{\infty}} = \frac{4 \times 10^{-3}}{2.5 \times 10^{-4}} = 16$$

Inserting this ratio and R_o (6.5 ft = 198 cm) into equation 2 yields the shock thickness.

$$\delta_s = \frac{0.75 \times 198}{16} = 9.3 \text{ cm}$$

The energy radiated toward the body for the given altitude and velocity is obtained from figure 6 and is seen to be approximately 3 watt/cm³. Multiplying this by the shock wave thickness yields the stagnation point equilibrium radiation heating rate.

$$q_r = 3 \times 9.3 = 28 \text{ w/cm}^2$$

3.1.1.2.2 Nonequilibrium Radiation - Page (reference 6) has obtained measurements of total radiation for several velocities as a function of free-stream density. As a result, he was able to determine the free-stream density associated with each velocity at which the shock standoff distance just equaled the nonequilibrium relaxation distance, and consequently, the magnitude of the nonequilibrium radiation.

His measured data are shown by the solid curves in figure 7. The dashed lines in figure 7 are the predicted equilibrium radiation values. The difference between the measured total radiation and the predicted equilibrium radiation gives the nonequilibrium component.

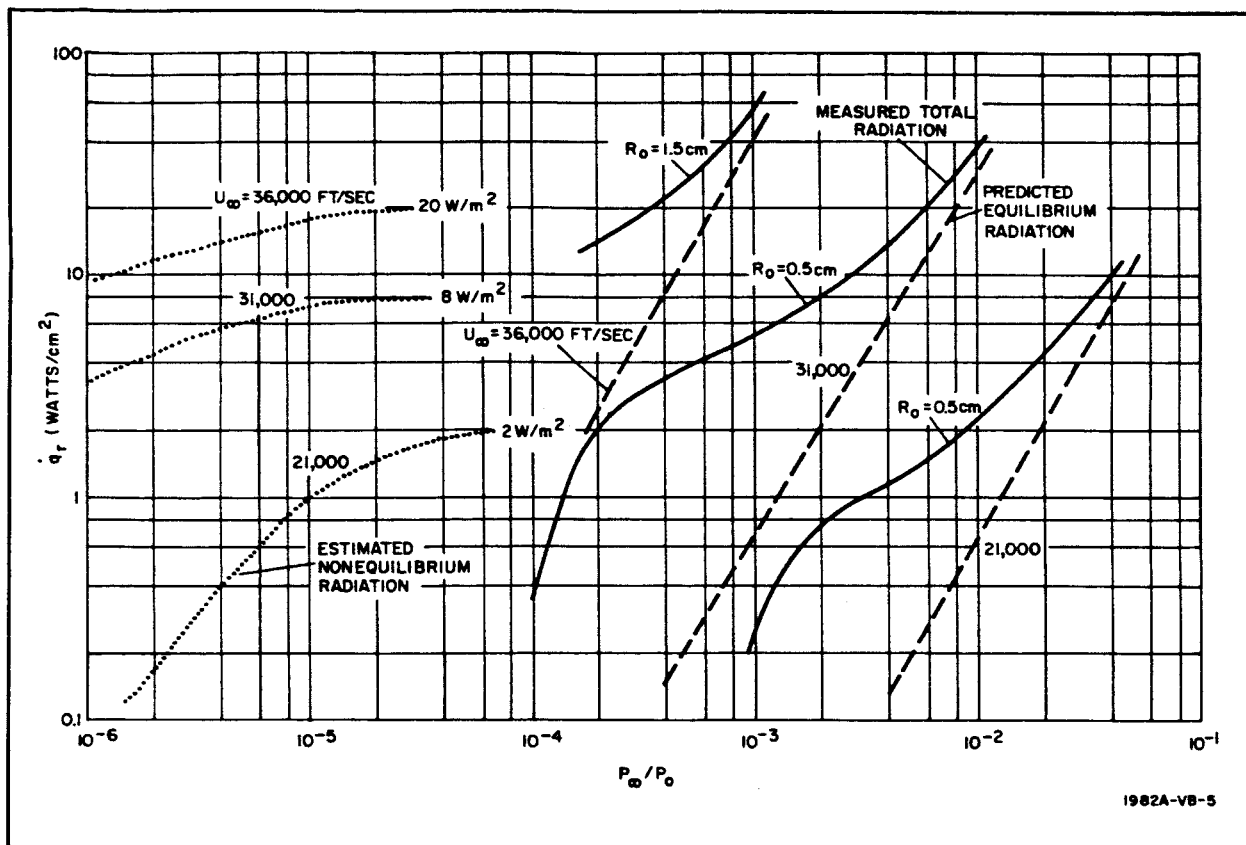


Figure 7. Nonequilibrium Radiation

In accordance with Page's theory discussed earlier, this nonequilibrium component remains constant at any given velocity and is not a function of body size except for truncation effects. The width of the nonequilibrium zone is proportional to density, and the shock width is proportional to nose radius. Therefore, to determine the density at which the nonequilibrium component develops in the Apollo case, it is necessary to translate Page's nonequilibrium measurements by the ratio of the model nose radius to the Apollo vehicle nose radius. These results are shown as the dotted curves in figure 7.

Using these curves as a basis, extrapolations of nonequilibrium radiation as a function of velocity and altitude are obtained and plotted in figure 3.

A sample calculation for the model is given below.

$$\begin{aligned}\text{Given: } R_o &= 0.5 \text{ cm} \\ U_\infty &= 31,000 \text{ ft/sec} \\ P_\infty/P_o &= 2 \times 10^{-3}\end{aligned}$$

The total radiation measured by Page shown in the solid curve of figure 7 for these conditions is

$$I_T = 8 \text{ w/cm}^2$$

The predicted component of equilibrium radiation from the dashed curve of figure 7 is

$$I_e = 2 \text{ w/cm}^2$$

Therefore, the nonequilibrium component is

$$I_T - I_e = I_n = 8 - 2 = 6 \text{ w/cm}^2$$

Now the Apollo vehicle nose radius is approximately 200 cm while the model radius is only 0.5 cm. Therefore, the density at which this 6 w/cm^2 value of nonequilibrium radiation would be obtained in the Apollo case is 400 times lower than the given density or

$$P_\infty/P_o (\text{Apollo}) = 2 \times 10^{-3} \times \frac{0.5}{200} = 5 \times 10^{-6}$$

Hence, 6 w/cm^2 is plotted at this density in the dotted curve.

3.1.1.3 Surface Radiation Limits

The boundary values of surface emission may now be obtained. The re-entry trajectory is first superimposed on figure 3 and the total heat inputs are summed up for every point on the trajectory. The equilibrium temperature is then determined by solving Plank's black body equation.

$$T_{eq} = \sqrt[4]{\frac{q_{Total}}{\sigma \epsilon}} \quad ^\circ K \quad (3)$$

For comparison purposes, this result, along with the stagnation temperature obtained from figure 1, is plotted in figure 8 for the 5000-nautical-mile trajectory of figure 2, considered typical at the time. Thus, the upper limit of radiation is set by a black body at this equilibrium temperature and the lower limit is set by a black body at $1000^\circ K$, the ablation temperature.

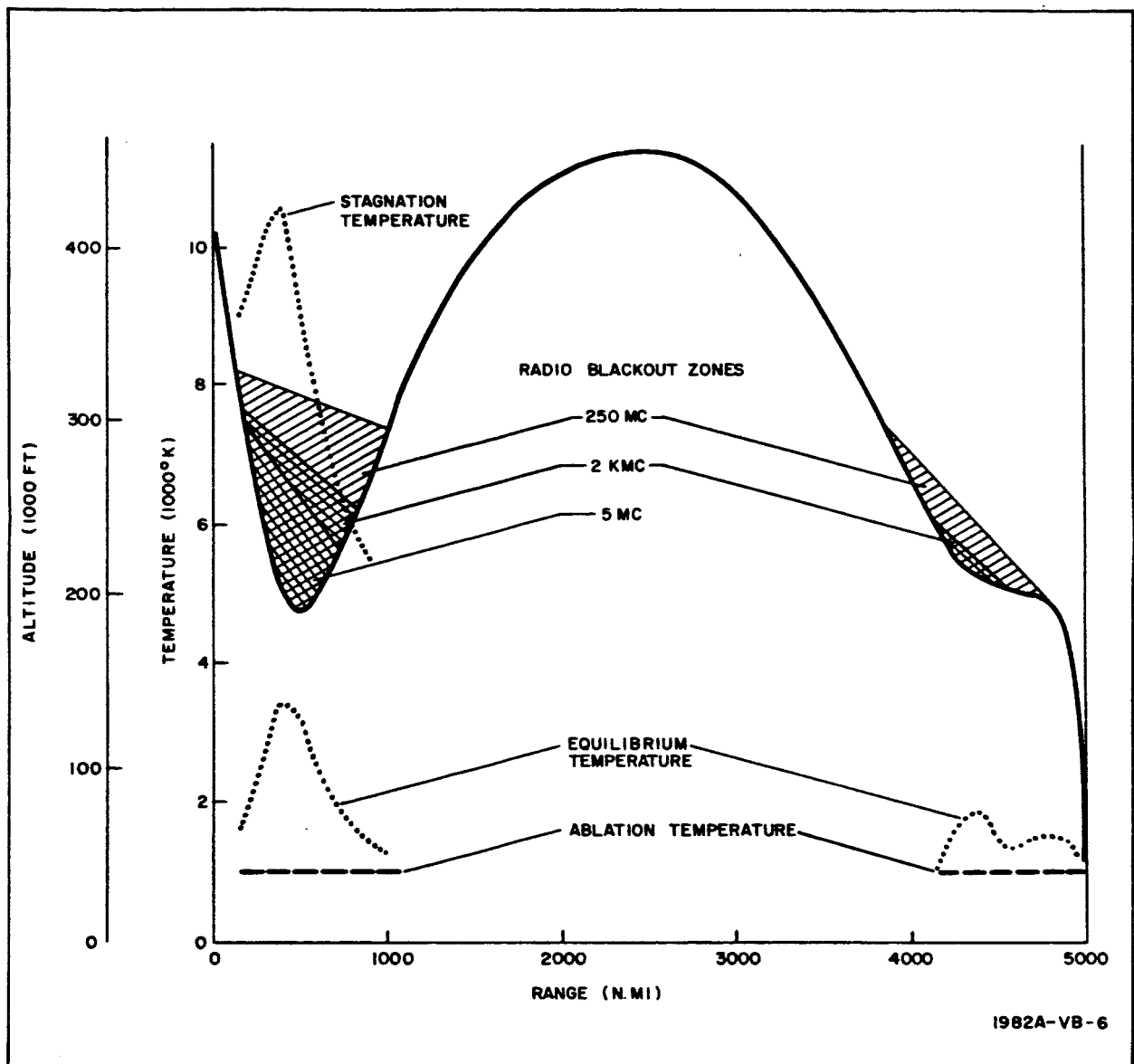


Figure 8. Apollo Reentry Temperature Profiles

The spectral distributions of these two boundary limits are shown in figures 9 and 10 for two points in the trajectory corresponding to the region where radio blackout commences and the region of maximum heating.

A sample calculation is given below.

Given: Altitude = 200,000 ft
Velocity = 30,000 ft/sec

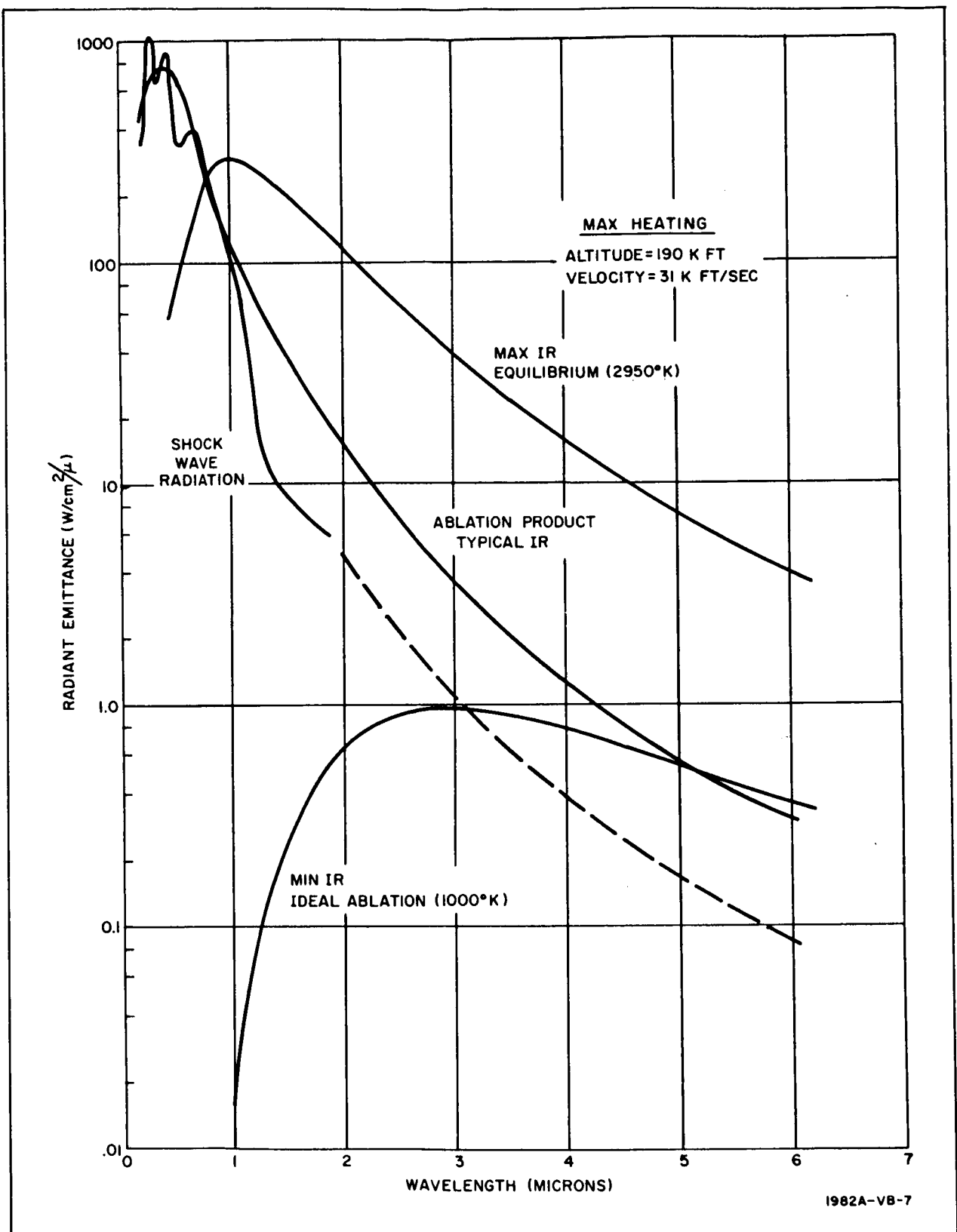


Figure 9. Stagnation Point Radiation

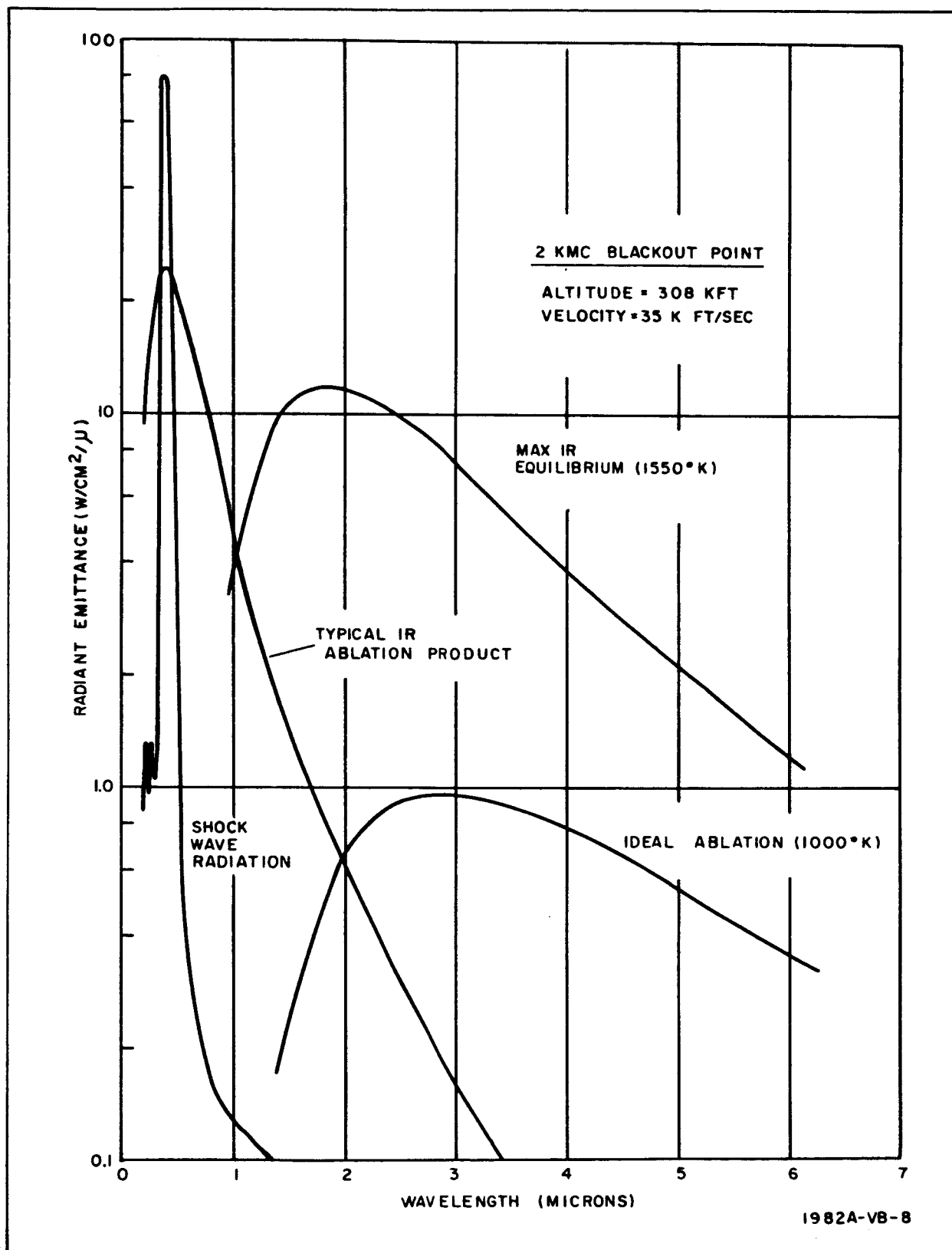


Figure 10. Stagnation Point Radiation

From figure 3 the input heat rates are:

convective	$\dot{q}_c = 193 \text{ w/cm}^2$
equilibrium	$\dot{q}_e = 28 \text{ w/cm}^2$
nonequilibrium	$\dot{q}_n = 7.5 \text{ w/cm}^2$
	<hr/>
Total	$\dot{q}_T = 228.5 \text{ w/cm}^2$

The equilibrium temperature from equation 3 is

$$T_{eq} = \sqrt[4]{\frac{228.5}{5.7 \times 10^{-12}}} = 2500^\circ\text{K}$$

3.1.2 Shock Wave Radiation

Examination of possible Apollo vehicle entry trajectories indicates that a considerable portion of the vehicular heating can be attributed to shock wave radiation. Thus, one might expect the shock wave to serve as an infrared source suitable for detection. This does not appear to be the case.

A reentering lunar vehicle possesses a kinetic energy on the order of 27,000 Btu/lb, most of which must be dissipated in the form of heat. No known material can absorb this much energy and survive. Consequently, reentering vehicles are designed to both radiate and ablate in an effort to expel this heat. The shock wave becomes a minor source of detectable infrared radiation because it is overshadowed by these vehicular emissions.

Examination of the trajectory data shows the equilibrium temperature to exceed 1000°K throughout the course of the trajectory of interest (radio blackout region). Thus, as a reference condition for comparison we can assume an ablation temperature of 1000°K corresponding to the minimum vehicular radiation throughout the trajectory. This yields a value of $\sigma \epsilon T^4$ or 5.7 w/cm^2 total black body radiation of which 20 percent is effective in the 2- to 3-micron region or approximately 1 w/cm^2 .

If we take the product of the shock wave radiation and the percent effective in the 2- to 3-micron region based on a gray body distribution at the stagnation temperature (i. e., a constant emissivity) we find that the shock wave

radiation would also be on the order of 1 w/cm^2 over the following range:

$$30,000 < v_{\infty} < 34,000 \text{ ft/sec}$$

$$8,000 < T_{st} < 12,000^{\circ}\text{K}$$

$$160,000 < \text{alt} < 220,000 \text{ ft}$$

Meyerott (reference 8) gives the spectral absorption coefficients for various temperatures and pressures but does not go beyond 2 microns. His results do indicate, however, a rising absorptivity at the longer wavelengths due to free electrons.

Wentink (reference 9) cites measurements in the near infrared for the conditions:

$$T_{st} = 8000^{\circ}\text{K}$$

$$P/P_0 = 0.85$$

from which the emissivity may be obtained as approximately 1.5×10^{-2} over the 2- to 3-micron band. The total emissivity for these conditions is given by Kivel (reference 10) as being 5×10^{-2} . This result implies that the emissivity is some 3 times less in the 2- to 3-micron band than the average, and hence the gray body assumption used above would be optimistic by a factor of 3.

Meyerott's (reference 8) data indicates that at higher temperatures and lower densities which are more typical of reentry conditions than Wentink's measurement conditions, the longer wavelength emissivity may predominate. Thus, the gray body assumption may be pessimistic. This area of uncertainty may not be resolved until further measurements have been obtained for the reentry conditions. In view of this, the gray body assumption seems as valid as any.

For the ablation temperature assumed, it is seen that the shock wave will at most only double the total available radiation in the 2- to 3-micron region. It will be observed, however, that the portion of the trajectory when the shock wave radiation is a maximum also corresponds to the portion where maximum heating occurs. Thus, it is quite likely that a char has formed and the

ablation temperature is closer to the equilibrium temperature which is on the order of 3000°K. At this temperature the vehicular emission is several orders of magnitude above the shock radiation in the 2- to 3-micron region.

In view of the above considerations, it is believed reasonable to ignore the shock wave radiation as a significant infrared source for detection in the 2- to 3-micron region. Further, because of its low absorptivity it cannot be considered as a serious detriment to the transmission of infrared radiation through the shock layer.

Spectral distributions of the shock wave corresponding to two selected points in the trajectory are shown in figures 9 and 10. They were obtained by multiplying the spectral emissivity per cm of shock wave (reference 8) by the shock wave thickness and multiplying by a suitable scale factor such that the integral agrees with the radiation heat rates of figure 3.

3.1.3 Ablation Product

The prediction of a typical value of infrared radiation from the stagnation region of an ablating Apollo vehicle reentering the earth's atmosphere is based on measurements and suggested extrapolations by Craig and Davey (reference 11). From the materials they evaluated, lexan was selected for this estimate since it is a polycarbonate resin and there is some indication that it is similar to what may be used on the Apollo vehicle. As a result of their report, the following expression may be used for extrapolating the local heating \dot{q}_a due to radiation by ablation products of lexan in the boundary layer.

$$\dot{q}_a = \dot{q}_{\text{ref}} \left(\frac{U_\infty}{U_{\text{ref}}} \right)^{2.6} \left(\frac{P_\infty}{P_{\text{ref}}} \right)^{.67} \left(\frac{R}{R_{\text{ref}}} \right)^{.5} \text{ w/cm}^2 \quad (4)$$

where

$$\begin{aligned} R_{\text{ref}} &= 5\text{m} = 16.4 \text{ ft} \\ P_{\text{ref}} &= 8 \times 10^{-5} \text{ (70 km = 230,000 ft alt.)} \\ U_{\text{ref}} &= 7 \text{ km/sec} = 23,000 \text{ ft/sec} \\ \dot{q}_{\text{ref}} &= 24 \text{ w/cm}^2 \end{aligned}$$

It should be noted that these reference conditions have already been extrapolated from the measurement conditions by three orders of magnitude in both size and density.

Using this expression, the local heating due to ablation was calculated for several points along the 5000-mile trajectory and are tabulated in table 1. The Apollo vehicle nose radius was taken as 6.5 feet. It will be noted that these densities are extrapolated two orders of magnitude from the reference density for a combined five orders of magnitude beyond the experimental conditions.

The local heating \dot{q}_a calculated in equation 4 is based on the results of measurements made over the 0.45- to 1.1-micron region; hence, it only represents that portion of the total heating within this band. To equate this selected band value to the total and/or some other selected band it is necessary to know something about the spectral distribution.

Craig and Davey assumed that the ablation products were contained within and uniformly distributed throughout the boundary layer. They further assumed that the wall temperature for lexan was 1000°K and that the temperature gradient across the boundary layer was linear, terminating at the stagnation temperature at the boundary layer edge. Further, their measurements indicated that the wall itself contributed a negligible amount of radiation in their selected measurement band.

Using this model, the source of the ablation product radiation may be thought of as infinitesimal layers of distributed particles of ablated products whose temperature is that prescribed by the position of the layer along the temperature gradient. It may further be assumed that the density of particles is sufficiently sparse that the integrated density of all layers is not sufficient to obscure radiation from any one layer. Therefore, the local heating due to ablation product radiation may be obtained by integrating Planck's equation over the temperature interval and spectral band of interest.

$$\dot{q} = A \int_{1000^{\circ}}^{T_e} \int_{\lambda_1}^{\lambda_2} C_1 \lambda^{-5} \left(\frac{C_2}{e^{\frac{1}{\lambda T}} - 1} \right)^{-1} d\lambda dT \text{ w/cm}^2 \quad (5)$$

TABLE 1.
ABLATION PRODUCT RADIATIVE HEATING RATES

Alt. (1000 ft)	P_{∞}/P_o	U_{∞} (1000 ft/sec)	T_e (°K)	0.45					0					2				
				\dot{q}_a (w/cm ²)	\dot{q}_a (w/cm ²)	\dot{q}_c (w/cm ²)	\dot{q}_r (w/cm ²)	\dot{q}_a^2 (w/cm ²)	∞	∞	∞	∞	∞	∞	∞	∞	∞	∞
330	4×10^{-7}	35	8500	1.2	2.4	9	6	0.14										
205	2×10^{-4}	33	11000	70	182	250	100	8.0										
188	4×10^{-4}	30	9300	80	176	300	70	9.2										
197	2.5×10^{-4}	28	8200	60	120	200	15	9.0										
295	2.5×10^{-6}	23.5	5200	2	3.4	7	1	.4										
207	1.7×10^{-4}	21	6100	20	34	70	2	2.6										
185	4×10^{-4}	13.5	4250	10	20	30	0	3.0										

A is a constant, dependent upon the free stream velocity and density, which is proportional to the density of particles in any given layer. This equation was used to calculate the local heating for the trajectory conditions listed in table 1 corresponding to the measurement pass band of 0.45 to 1.1 microns. Comparing these results with those obtained from equation (4) yields the appropriate constant A to be used in equation (5).

Equation (5) was then used to calculate the total heating, $\lambda_1 = 0$ to $\lambda_2 = \infty$, and the infrared radiation, $\lambda_1 = 2$ to $\lambda_2 = 3$ microns. Also included is the stagnation temperature.

It is of interest to compare the total local heating due to ablation products with the normal convective and radiative heat inputs. These values are given in table 1 as \dot{q}_c and \dot{q}_r adjacent to \dot{q}_a ($\lambda_1 = 0$ to $\lambda_2 = \infty$). The numerical values are obviously comparable and may impose a restriction on the efficiency of the ablation material.

The IR radiation in the 2- to 3-micron band, as shown in the last column of table 1, is large compared to the minimum target limit of 1 w/cm^2 at 1000°K , except for the highest altitude cases. It should be noted that in the spectrum of measurements by Craig and Davey, only 1.5 percent of a 1000°K black body radiation is available, which yields 0.083 w/cm^2 as compared to 1.2 measured. Consequently, the wall could be a black body at 1000°K with unit emissivity and have little or no effect on their measurements. Therefore, the results obtained in table 1 are considered to be due solely to the ablation products injected into the boundary layer and not from the wall. These results must be added to the minimum target value of 1 w/cm^2 to yield a typical IR target value for the 2- to 3-micron band.

These results are plotted as a function of position along the trajectory in figure 11. Also included are the maximum and minimum radiation values along with the 250-mc (worst case) blackout zone.

The spectral distribution may be obtained from equation (5) by dropping the wavelength integral. This was done for two points in the trajectory and plotted in figures 9 and 10.

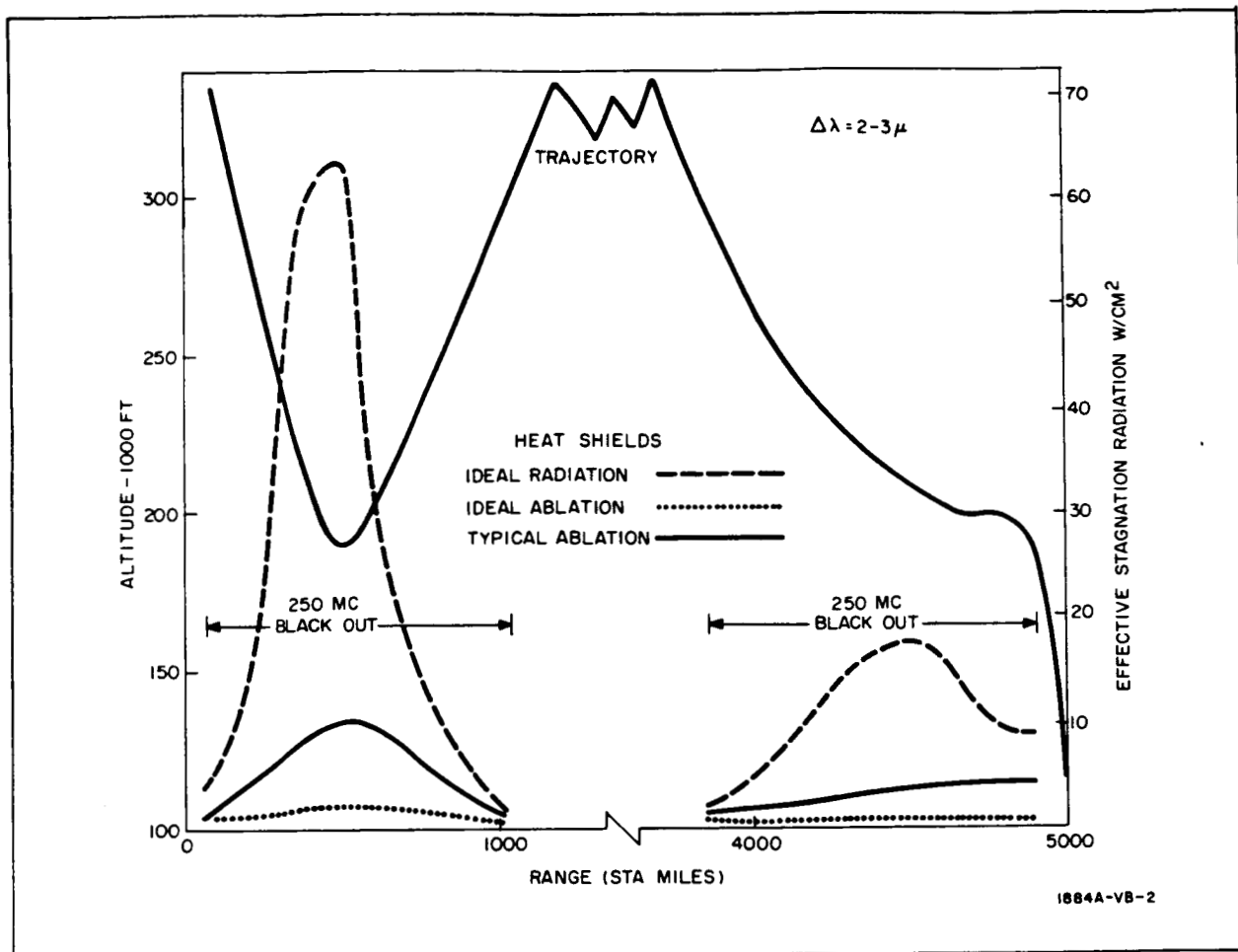


Figure 11. Apollo Vehicle Reentry Radiation

3.2 ATMOSPHERIC TRANSMISSION

The atmospheric transmission is calculated by procedures established by Altshuler (reference 12). He considers a model consisting of infrared absorbing atmospheric constituents CO_2 , O_3 , N_2O , CH_4 , CO , and water vapor and their variation in accordance with temperature and pressure changes with altitude based upon the 1959 ARDC model atmosphere. He also takes into account the Earth's curvature and refraction of infrared in the Earth's atmosphere.

Of the absorbers considered, it turns out that O_3 is significant only beyond 4.3 microns and N_2O beyond 3.8 microns; CH_4 and CO are sufficiently

weak compared to the others and hence can be ignored. Consequently, the only significant absorbers in the spectral region of interest are CO₂ and water vapor.

Consideration of the relative distribution with altitude above 40,000 feet of the CO₂ and water vapor absorbers as derived from Altshuler indicates that the bulk of the absorber exists below 100,000 feet. Consequently, since radio blackout occurs above 100,000 feet, it is sufficient to calculate the atmospheric transmission between the altitudes of 40,000 and 100,000 feet as a function of look angle ($0^\circ < \alpha < 90^\circ$) and apply the results directly to the Apollo case regardless of the Apollo vehicle altitude.

Based on the above considerations, Altshuler's procedures were used to calculate the spectral transmission of CO₂ and water vapor as a function of look angle from 0 to 90 degrees from a 40,000-foot platform. These results are plotted in figure 12.

To check the applicability of these results to the actual case, Altshuler's results were compared with experimental measurements. Murcray (reference 13) has made measurements with a balloon of the atmospheric transmission as a function of altitude. A set of his data obtained at 40,000 feet with a look angle of 60.5 degrees is also shown in figure 5. Although his data show higher resolution, they are in good agreement with the curves of figure 12; consequently, they provide confidence that the curves of figure 12 are both realistic and applicable.

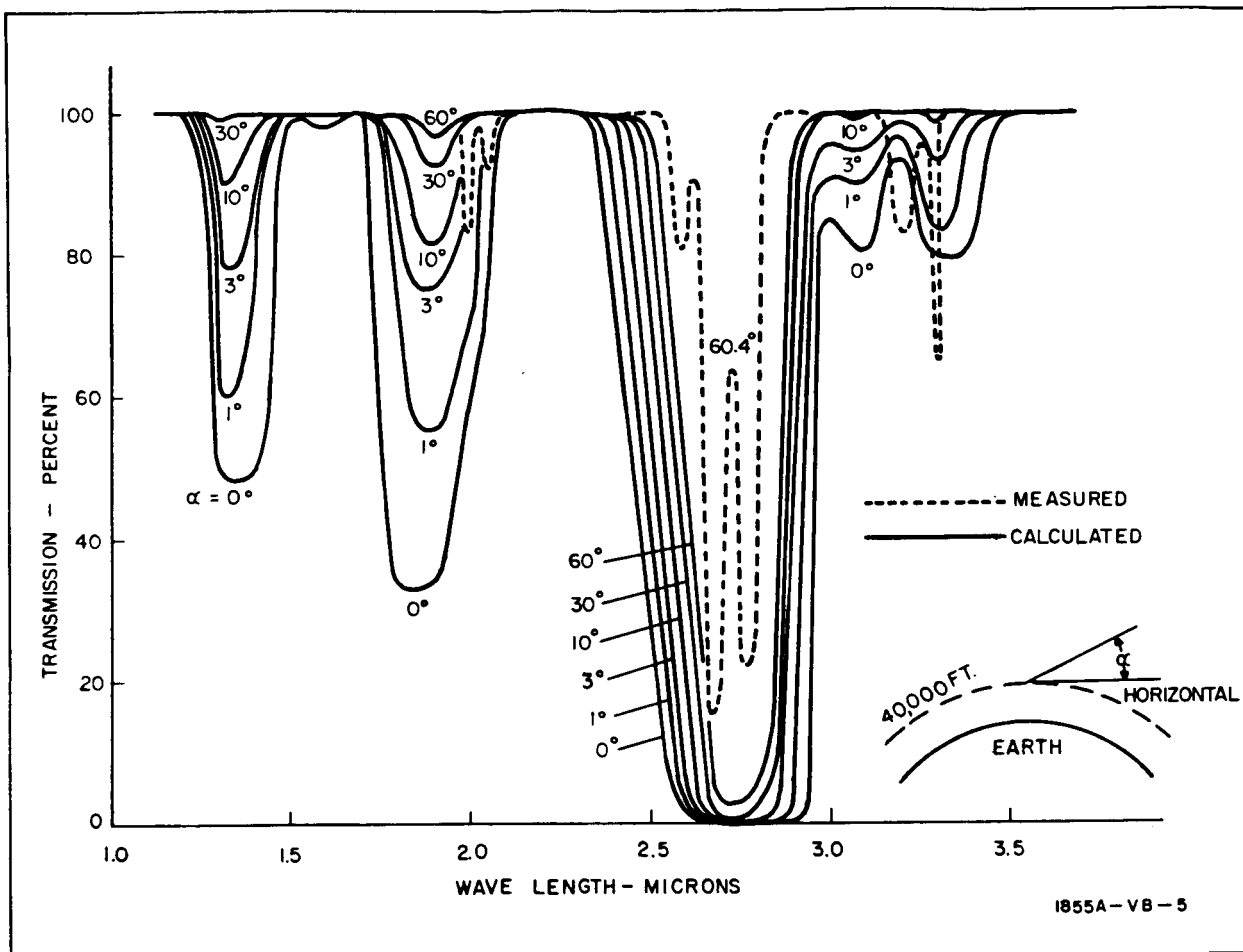


Figure 12. Atmospheric Transmission

3.3 RANGE RELATIONS

To compute the irradiance at the receiver, it is necessary to know the line-of-sight range between the target and the receiver, commonly referred to as the slant range. Further, it is desirable to know distance along the reentry range track corresponding to a particular slant range, referred to herein as ground range.

These relationships are given in the equations below and are derived from the geometry of figure 13.

$$S = r_e \theta \quad (6)$$

$$\cos \theta = \frac{(r_e + h_o)^2 + (r_e + h_t)^2 - R^2}{2(r_e + h_o)(r_e + h_t)} \quad (7)$$

$$R = - (r_e + h_o) \sin \alpha + \sqrt{(r_e + h_t)^2 - (r_e + h_o)^2 \cos^2 \alpha} \quad (8)$$

The results of these calculations are shown in figure 14 for three target altitudes of interest. The observer altitude is 40,000 feet. The solid curves give ground range in nautical miles and the dotted curves give slant range in kilometers, both as functions of the look angle, α .

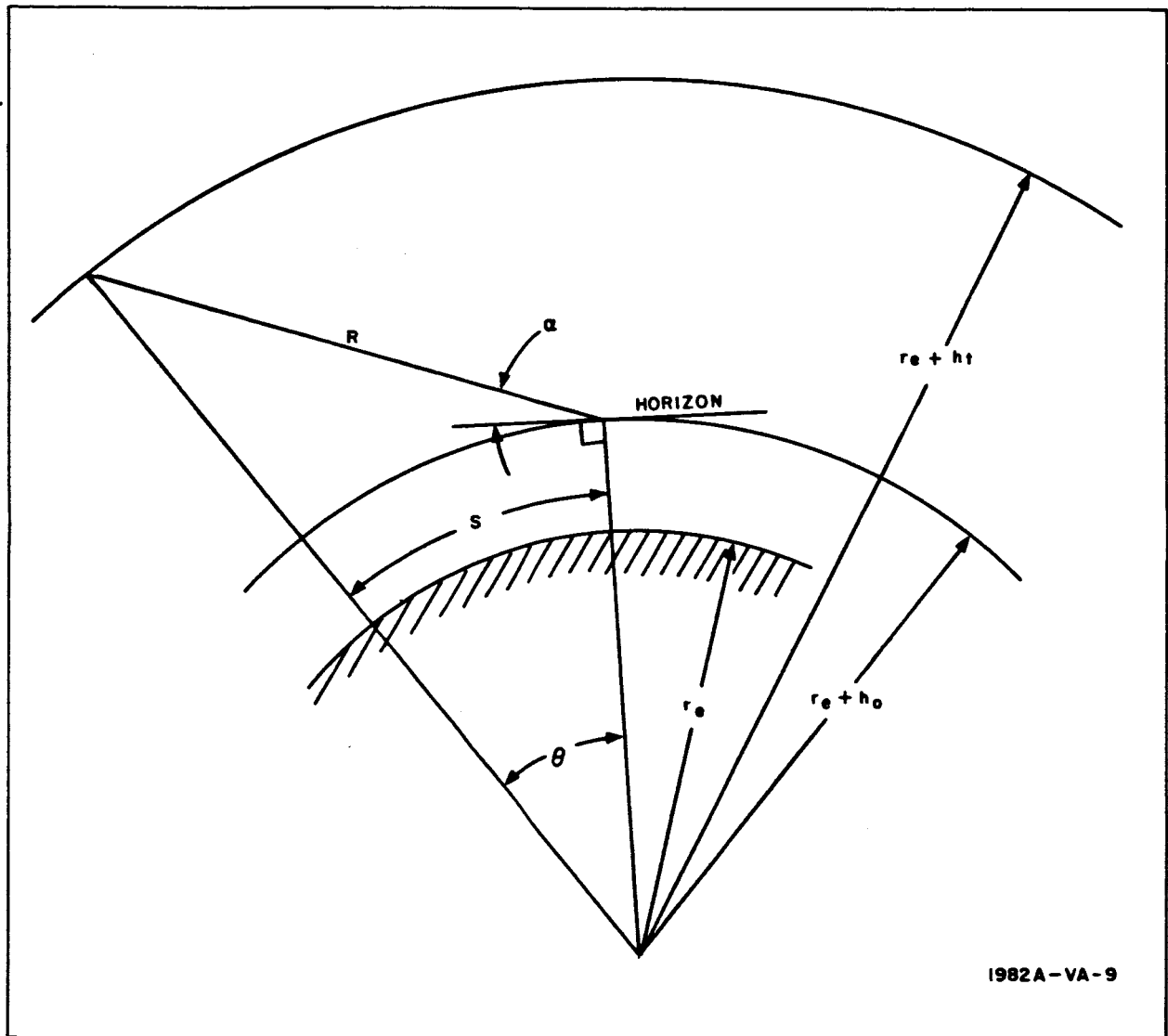


Figure 13. Range Geometry

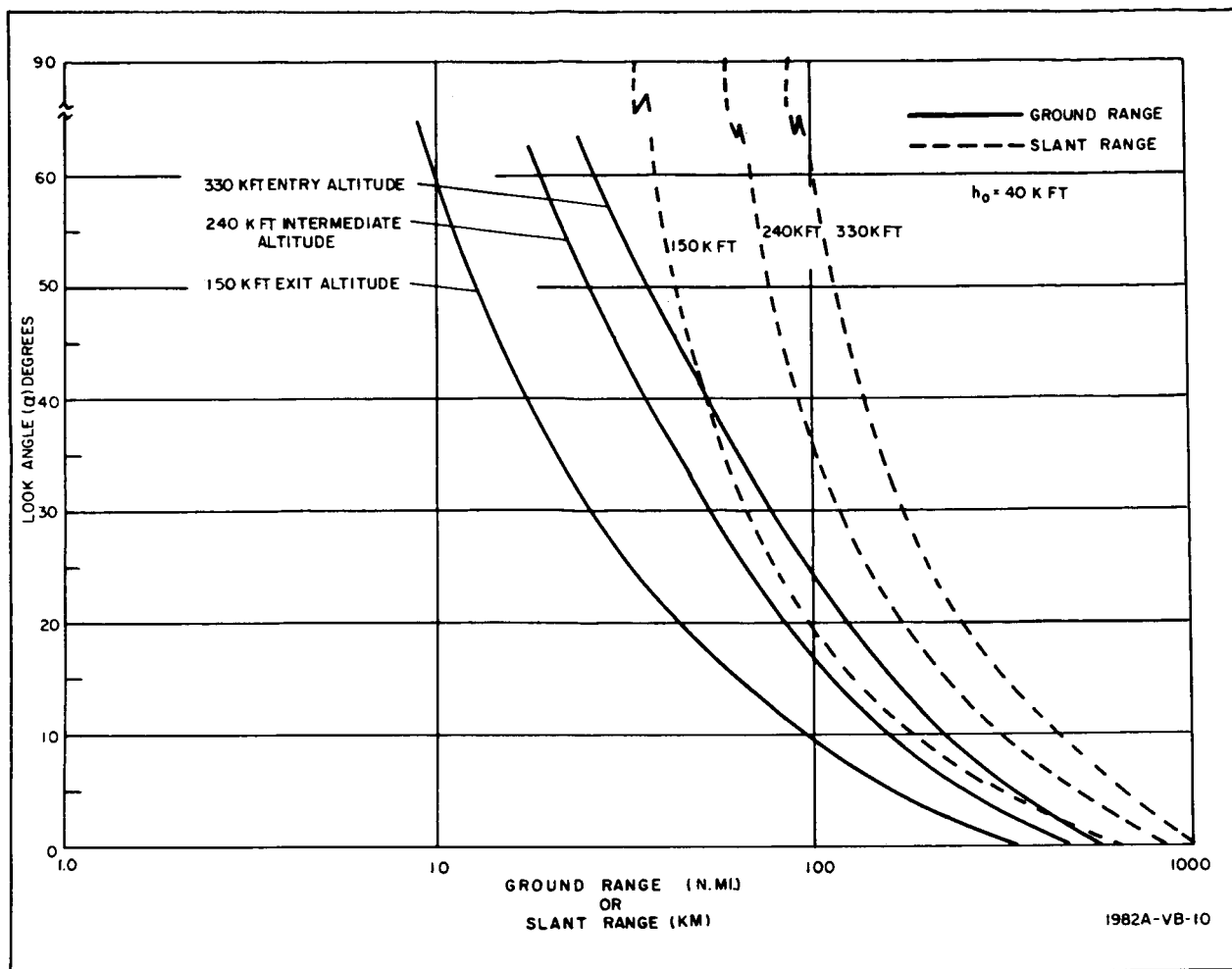


Figure 14. Range Relations

3.4 INFRARED IRRADIANCE LEVELS

The infrared radiation emanating from the stagnation point was calculated by methods outlined earlier and plotted in figures 9, 10, and 11. To calculate the total energy radiated by the Apollo vehicle, it is necessary to consider the distribution over the face of the vehicle. This distribution is influenced by angle of attack, nose curvature, wall temperature, and surface smoothness. Several measurements have been made on this distribution at Ames Research Center and are given in references 14 and 15. This data is classified and hence cannot be applied here. Inasmuch as the estimates contained herein are based on maximum and minimum temperature

considerations and in view of the large influence on the radiation estimates by the ablation products, as reported by Craig and Davey (reference 11), it does not appear that unreasonable error will arise if the stagnation conditions are assumed to hold over the entire Apollo vehicle face. On this basis, the area of the Apollo vehicle face is taken to be $1.25 \times 10^5 \text{ cm}^2$ corresponding to a 13-foot diameter.

Examination of the equilibrium temperatures over the course of the trajectory (see figure 8) indicates that at no point in the radio blackout zone will the equilibrium temperature be less than 1000°K . Thus, in accordance with our original postulation we can assume a minimum target temperature to be 1000°K corresponding to the ablation temperature.

A 1000°K black-body distribution, along with a lead sulfide detector response, is shown in figure 15. It may be further stated that the minimum irradiance will be obtained at the maximum range which would correspond to a 0-degree look angle. Therefore, the atmospheric transmission curve for a 0-degree look angle from figure 12 may be used in conjunction with the detector and 1000°K black-body distribution of figure 15 to obtain the minimum apparent target radiant intensity in the 2- to 3-micron band.

$$J_{\min} = \frac{A}{\pi} \int_2^3 T_{\lambda} D_{\lambda} W_{\lambda} d_{\lambda} = 25 \text{ kw/steradian} \quad (9)$$

The maximum range would correspond to the case where radio blackout just commences and the Apollo vehicle first enters the atmosphere. From figure 8, this is seen to be at 330,000 feet as observed from a 0-degree look angle from a 40,000-foot platform. This range turns out to be 1061.9 km as may be seen in figure 14. Thus, the minimum target irradiance and consequently minimum detection sensitivity becomes

$$H_{\min} = \frac{J_{\min}}{R^2} = 2.16 \times 10^{-12} \text{ w/cm}^2 \quad (10)$$

The maximum target irradiance is based on the highest equilibrium temperatures as seen from the shortest range corresponding to a look angle of 30 degrees. From figure 8, this temperature is seen to be approximately 3000°K at an altitude of 200,000 feet. This corresponds to a range of 96.4 km.

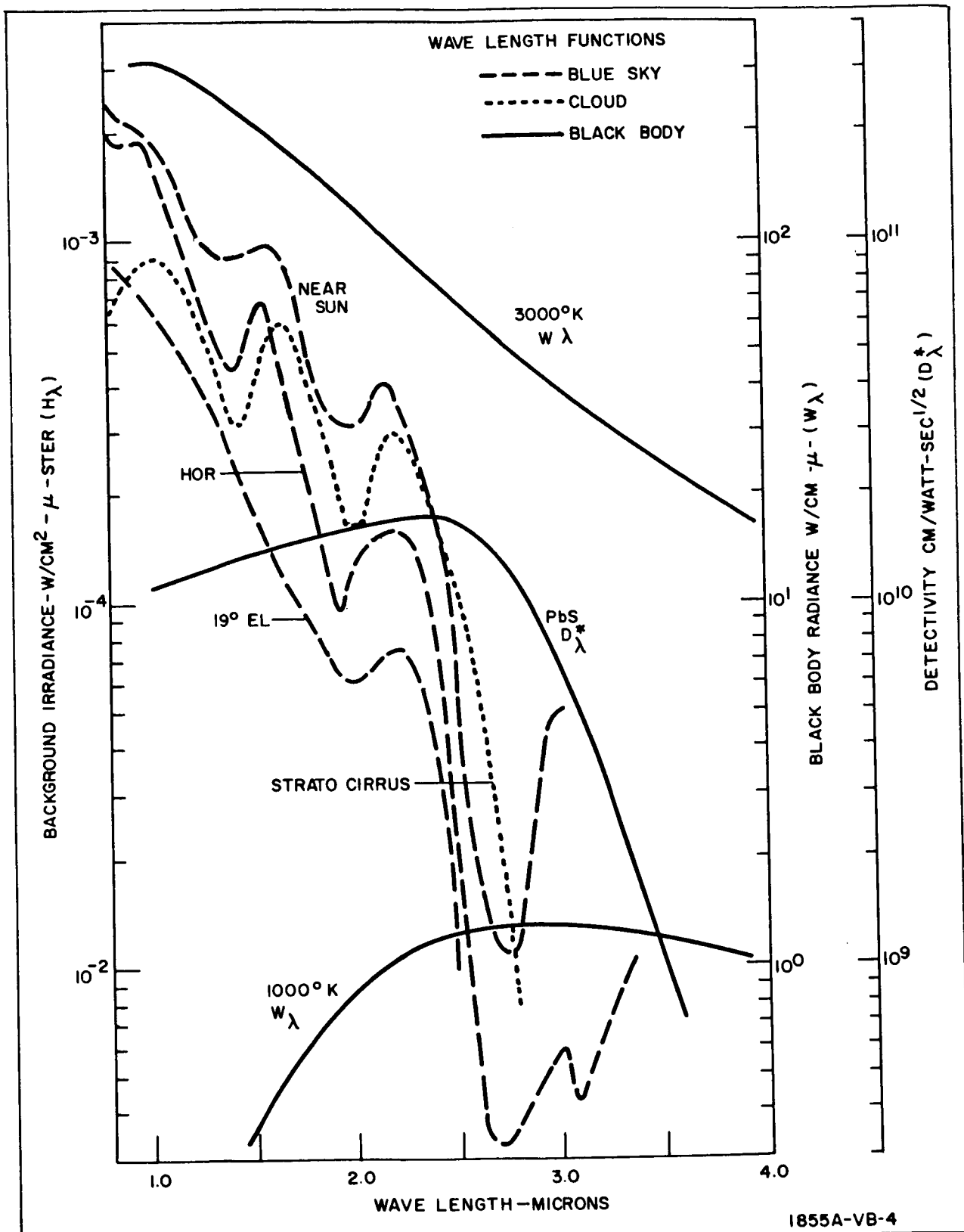


Figure 15. Wavelength Functions

Again, using the curves of figures 12 and 15 and equations 9 and 10, the following maximum values are obtained:

$$J_{\max} = 2.8 \times 10^6 \text{ w/steradian}$$

$$H_{\max} = 3.05 \times 10^{-8} \text{ w/cm}^2$$

The significance of the minimum value is that it establishes the least possible irradiance to be expected and thus serves as a basis for specifying the minimum detection sensitivity.

The significance of the maximum value is that it establishes the largest conceivable irradiance level that might be encountered, so that the dynamic range requirements for the electronics may be specified. From the foregoing numbers this irradiance level is seen to be of the order of 10^4 .

4. BACKGROUND INTERFERENCE

The spatial and spectral intensity distributions throughout the background may be of such a nature as to interfere with the reliable detection of the desired target. This interference may arise in a variety of ways but only three forms will be considered here which, in this application, encompass the worst cases. They will be referred to as photon noise, scan modulation, and scanning noise.

4.1 PHOTON NOISE

Photon noise (reference 16) is the name given to the generation-recombination noise induced in the detector by the random arrival of photons from the background. Because of its uncorrelated nature it is proportional to the square root of the incident background photon flux. Thus, at some background flux level the photon noise will exceed the internal noises of the detector and consequently reduce its sensitivity.

The photon noise limited detectivity may be expressed as (reference 17):

$$D_{\lambda}^* = \frac{\lambda}{2} \frac{10^{19}}{\sqrt{Q_B}} \text{ cm/watt-sec}^{1/2} \quad (11)$$

Q_B is the effective background flux density and may be calculated from the following expression:

$$Q_B = \frac{10^{19}}{2} \int_{\lambda} \eta_{\lambda} W_{\lambda(BG)} d_{\lambda} \text{ photons/sec-cm}^2 \quad (12)$$

Where $W_{\lambda(BG)}$ is the background flux density incident on the detector. In an f/l optical system, the angle of acceptance at the detector is approximately 1 steradian; therefore, the value of $W_{\lambda(BG)}$ can be obtained directly from the ordinate H_{λ} in figure 15 where background spectral distributions as measured by Vandehei (reference 18) are given.

Taking the "near sun" distribution as the worst case, the integral of equation 12 yields $Q_B = 1.5 \times 10^{16}$ photons/sec-cm². Inserting this value into equation 11 and solving for the photon limit detectivity at 2.5 microns yields $D^* \approx 10^{11}$ cm/watt-sec^{1/2}.

Comparing this value with the measured D^* curve of PbS on figure 6 shows that the measured value is less; therefore, one can conclude that photon noise will not be a background problem in this application.

4.2 SCAN MODULATION

The average background radiance can vary as one scans a complete circle in azimuth. This variation in average radiance with scan position gives rise to a low-frequency signal which, if large enough, can cause limiting in the preamplifier and thus in effect cause modulation of any real signals present.

Measurements of sky luminance taken at 20,000 feet by Duntley (reference 19) indicate this maximum value to be on the order of 200 to 1. Thus, all electronics prior to the signal filter must be capable of accepting this range without distorting real signals which may be riding on it.

4.3 SCANNING NOISE

Scanning noise is the name given to the signals induced in the detector by undesired background discontinuities such as clouds. Such signals are transient in nature and thus contain frequencies characteristic of the Apollo target signal.

Discrimination techniques based on spatial and/or spectral differences are required to reject these undesirable targets. Figure 15 indicates that there is insufficient difference in the spectral distribution of a hot target (3000°K) and a stratocirrus cloud to facilitate effective spectral discrimination; therefore, spatial discrimination must be employed. It becomes necessary to know the magnitude of the cloud signal for implementing such a scheme.

Figure 15 shows the irradiance of a stratocirrus cloud in the 2- to 3-micron region to be on the order of 10^{-4} w/cm²-steradian which corresponds to 10^{-10} w/cm² for a 1 mr FOV. This is on the order of 100 times the required detection sensitivity. Inasmuch as this may not be the brightest cloud

to be encountered, a safety factor should be added, and the system should be designed to handle a background dynamic range of at least 10^3 .

4.4 BACKGROUND DISCRIMINATION TECHNIQUES

Passive infrared surveillance systems depend on radiation being emitted by the target to enable detection. All matter above absolute zero temperature emits radiation; consequently, every element in the surveillance field of view competes for detection. To realize a surveillance system which will detect only the desired target and ignore all other unwanted sources which make up the background, it is necessary to incorporate a scheme which discriminates between the two.

Various discrimination techniques have been conceived with different degrees of success in many applications. They are too numerous to digress on here, but all depend on exploiting some characteristic difference between the target and its background. Some typical differences which may exist are listed below along with the categorical type of discrimination.

<u>Type of Discrimination</u>	<u>Characteristic Difference</u>
Spatial	Image size (projected area)
Spectral	Spectral distribution of irradiance
Amplitude	Radiation intensity
Signature	Radiation modulation
Motion	Angular rate
Temporal	Rate of change in intensity

Of the types listed, only spatial discrimination appears to apply in the case of detecting the Apollo reentry vehicle against a sunlit sky background.

Spectral discrimination is precluded because the temperature of the reentry vehicle can approach that of the sun, thus presenting a spectral distribution very similar to the sunlit sky.

The estimated irradiance at the receiver for a 1- milliradian field of view, due to the background, can be approximately 10^3 times larger than that of the Apollo vehicle; therefore, amplitude discrimination cannot be used.

It is anticipated that the aerodynamic heating of the reentry vehicle will result in a smooth, continuous transition in temperature, not giving rise to modulation in infrared radiation unless, of course, turbulence sets in. In this case, the modulation would not be predictable. Consequently, no defined signature is expected.

Over head, the angular rate can be quite large. However, at long ranges near the horizon the angular rate can be insignificant compared to that of adjacent clouds. For this reason, motion discrimination alone would not be a reliable technique.

The intensity of the infrared radiation from the reentry vehicle is a function of position along its reentry trajectory as well as aspect. Consequently, the rate of change of intensity with range may be compensated by these effects. Further, the change in intensity with range at long ranges is almost imperceptible even if the vehicular radiance and aspect were constant. Therefore, temporal discrimination is also unreliable in this application.

Spatial discrimination is particularly lucrative because even at the minimum range of approximately 120,000 feet (overhead case: Apollo at 160,000 feet; scanner at 40,000 feet) the 1-milliradian area projected in space is 120 by 120 feet or approximately 10 times the reentry vehicle diameter. Hence, the target will constitute a point source.

For these reasons spatial discrimination is the preferred type for this application.

4.5 SPATIAL DISCRIMINATION

All spatial discrimination techniques exploit the characteristic difference in size between a point-source target and extended-area background elements. The extent to which this can be achieved is limited by the resolution of the optical system. This is to say that contemporary spatial discrimination techniques cannot reject background elements which subtend an angle comparable to or less than the blur circle size. Thus, fine resolution is a prime prerequisite for good spatial discrimination.

Contemporary spatial discrimination techniques may be classified into four categories as defined by the method used to achieve discrimination.

<u>Technique</u>	<u>Method</u>
Spatial filtering	Reticle averaging
Pulselength discrimination	Electronic filtering
Area cancellation	Detector geometry
Space correlation	Memory comparison

Spatial filtering is effected by employing a reticle with a suitable pattern of many small transparent and opaque apertures. The theory of operation is that point-source targets, being smaller than the apertures, will be chopped and will generate a signal at a finite carrier frequency as determined by the chopping rate. Extended area targets, primarily clouds, will fill many apertures, thus averaging out the radiation reaching the detector and therefore minimizing background-induced signals at the chopping frequency. An advantage of this technique is that it provides filtering in two dimensions. The primary disadvantages are a 50 percent loss in target energy due to the opaque apertures and susceptibility to transients which give rise to frequencies in the signal spectrum when scanning over gradients, cloud edges, etc.

Pulselength discrimination utilizes a small scanning aperture, comparable to the optical resolution. The scene is scanned, generating an electrical wave train whose component amplitudes and widths are proportional to the intensity and dwell time of the background elements imaged on the aperture along the line of scan. The theory of operation is that point-source targets will generate narrow pulsewidths while extended area sources will generate wide pulsewidths. Electronic filtering can then be optimized to accept the target waveshape while all other waveshapes are rejected. This technique utilizes all of the available target energy but is restricted to discrimination in only one dimension, along the line of scan.

Area cancellation is similar to spatial filtering except that it employs a detector whose geometry provides the reticle function. The detector is subdivided into small detector elements, each comparable to the optical

resolution, similar to the aperture size in the reticle case. Where, in the reticle case, apertures are alternately transparent and opaque, area cancellation detector elements are biased alternately positive and negative. When the image of a point source is scanned across the detector, a wave train of positive and negative pulses will be derived. The frequency of this signal will depend on the scan velocity and size of the detector elements. When an extended area background source is scanned across the detector, as many positive elements as negative elements are illuminated on the average and the two opposing induced signals cancel one another. This technique is two-dimensional and utilizes all of the available target signal energy. However, it is restricted by the geometries into which detectors can be fabricated.

Correlation techniques comprise methods where in an element or ensemble of elements in space is compared with its neighbor elements in some space relationship to determine the degree of similarity. For instance, the radiance of each point in space (called reference point) could be compared with the radiance from each immediately adjacent point (hereafter called space sample point) surrounding the reference point. If any one of the sample points had the same radiance as the reference point, the reference point would be rejected as an extended area. If none of the sample points have the same radiance as the reference point, it will be accepted as a point source. Unless the reference point and sample points are viewed simultaneously by separate detectors, some memory device is required to store radiance values from certain points in space so that simultaneous comparison of the points of interest may be facilitated. This technique requires more complexity but offers the advantages of two-dimensional discrimination, full utility of available target energy, and permits a prerogative to be exercised on the type of target acceptance logic used.

Each of the techniques described offers some advantage over the others in some application. No one technique encompasses all of the features of the others. Further, none are perfect against all background types. They will each suppress the background to some extent, permitting better

performance than would be obtained without discrimination but not necessarily as good a performance as in the absence of background signals. Thus, regardless of the technique used, background noise establishes the limit of sensitivity that can be achieved in the presence of background interference. This stems partly from the fact that these techniques are intended to enhance the detection of point sources superimposed in background elements such as clouds, as well as reject false targets, such as cloud edges. Consequently, these techniques do not reject background on a go, no-go basis, but absorb and select signals. In the end, some false alarms will result.

In the Apollo case the reentry vehicle, during periods of ionization, will always be higher than the highest clouds and therefore will never be in front of the clouds as seen by an observer at 40,000 feet. Based on the premise that a cloud dense enough to reflect sufficient sunlight and to cause a background problem is too dense to look through, the reentry vehicle can never be detected with a cloud within the instantaneous field of view. Consequently, whenever a detectable cloud fills the instantaneous field of view, the system can be blacked out with no loss in performance, so far as detecting the vehicle at that instant is concerned.

For these reasons a go, no-go criterion may be used in the discrimination scheme wherein the system is blacked out whenever a cloud signal is present. This approach, which is peculiar to the Apollo vehicle detection case, can be best implemented by digital space correlation techniques.

4.6 DIGITAL SPACE CORRELATION

Digital space correlation is the descriptive name given to the delay line discrimination technique employed in the Apollo reentry vehicle infrared detection system feasibility model breadboard. It consists of dissecting the search field of view into a matrix of elemental fields of view. Each elemental field of view is in turn examined for presence of a signal. If a signal is found to exist on a given element each of its four adjacent matrix neighbors (right, left, above, and below) are examined for presence of a signal. If any one or more of these elements also possesses a signal, the signal on the given element is rejected as that due to an extended area source. If none of the

neighboring elements possess a signal, the signal on the given element is accepted as that due to a point-source target.

This technique, as it is employed in the feasibility breadboard, uses digital methods in the discrimination logic. To be detected, a signal must exceed a threshold. All signals exceeding the threshold are treated as equal and assigned unit values, while those that do not exceed the threshold are treated as nonexistent and assigned zero values. Thus, the radiance distribution in the search field of view may be resolved into a space matrix with zeros assigned to all elements whose radiance is less than the critical amount and ones assigned to all elements whose radiance exceeds the critical value. The foregoing logic can then be employed for selecting point sources; i. e., finding ones surrounded by zeros.

Figure 16a illustrates a search field containing a target and a cloud. Figure 16b shows the same scene in which a space matrix has been superimposed and the corresponding digital values assigned. Figure 16c is the same scene as presented to the logic circuits where only the ones show up. After the logic circuits have correlated the signal on every element with each of its neighbors and accepted only those signals which have zero correlation, the resultant output scene would appear as in figure 16d.

Because of the digital logic, the discrimination scheme is insensitive to amplitude. As a consequence, an extended area source is rejected regardless of the intensity distribution over the area of the source so long as it is sufficient to exceed the threshold value. This means that a target can never be seen in front of a cloud, but by the same token radiance distributions within a cloud which might induce signal frequency spectra similar to a point source will never cause a false alarm.

This result is particularly applicable to the Apollo detection case because the reentry vehicle, during radio blackout, will never be at an altitude below the clouds and consequently never in front of them. Further, one cannot see through clouds dense enough to constitute a background problem; consequently, blanking the system when looking at a cloud cannot degrade the ability to detect the Apollo vehicle but will virtually eliminate false alarms on background elements larger than the instantaneous field-of-view size.

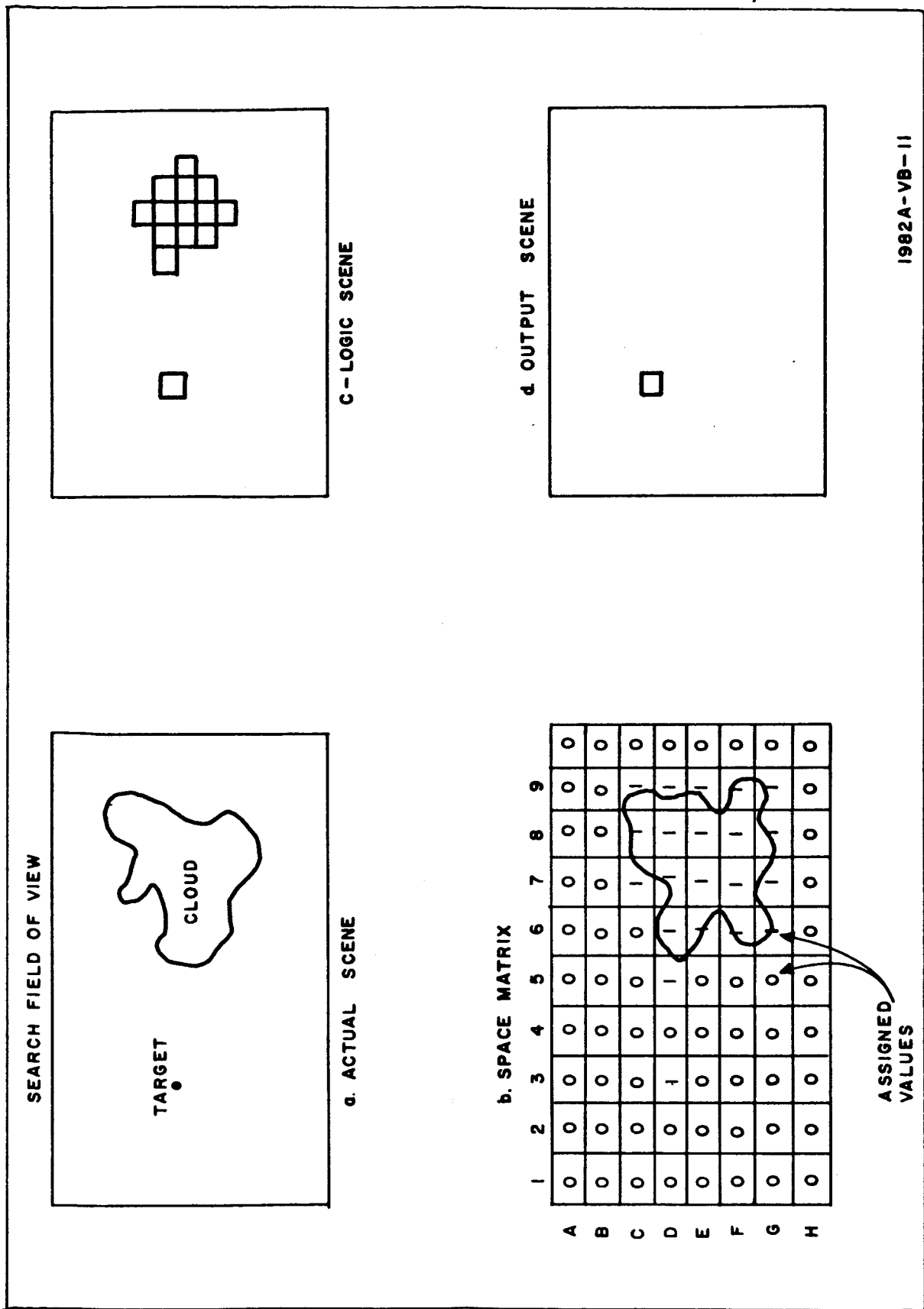


Figure 16. Digital Space Correlation

5. DESIGN CONSIDERATIONS

As per the contractual design specification, the feasibility model is to possess a linear detector array of at least 10 uncooled PbS elements, each subtending a 1-milliradian field of view. The array is to be oriented vertically and scanned horizontally in space at a rate of 360 degrees per second. Each element of the array is to be sampled by a commutator in such a manner that no "holes" are left in the scan pattern. Background discrimination is to be incorporated.

For the most part these general specifications prescribe the scanning operation. The actual mechanization used to implement these requirements is described in detail later. There are, however, some design considerations due to the type of discrimination employed which reflect on other elements of the composite system.

Therefore, the discrimination concept is discussed first and the other system parameters pertinent to performance are developed from that point, culminating in a prediction of detection sensitivity.

5.1 DELAY LINE DISCRIMINATION

Digital space correlation was described in principle earlier in this report. A practical means of implementing this principle is through the use of delay lines. Thus, the functional name given to the digital space correlation technique herein is referred to as delay line discrimination.

5.1.1 Concept of Operation

Consider an infrared system that possesses a detector array containing 10 detector elements which sweep out a volume in space by scanning from left to right as shown in figure 17a.

The outputs of each detector element are sequentially sampled by a commutator from top to bottom at a rate such that each element in the entire

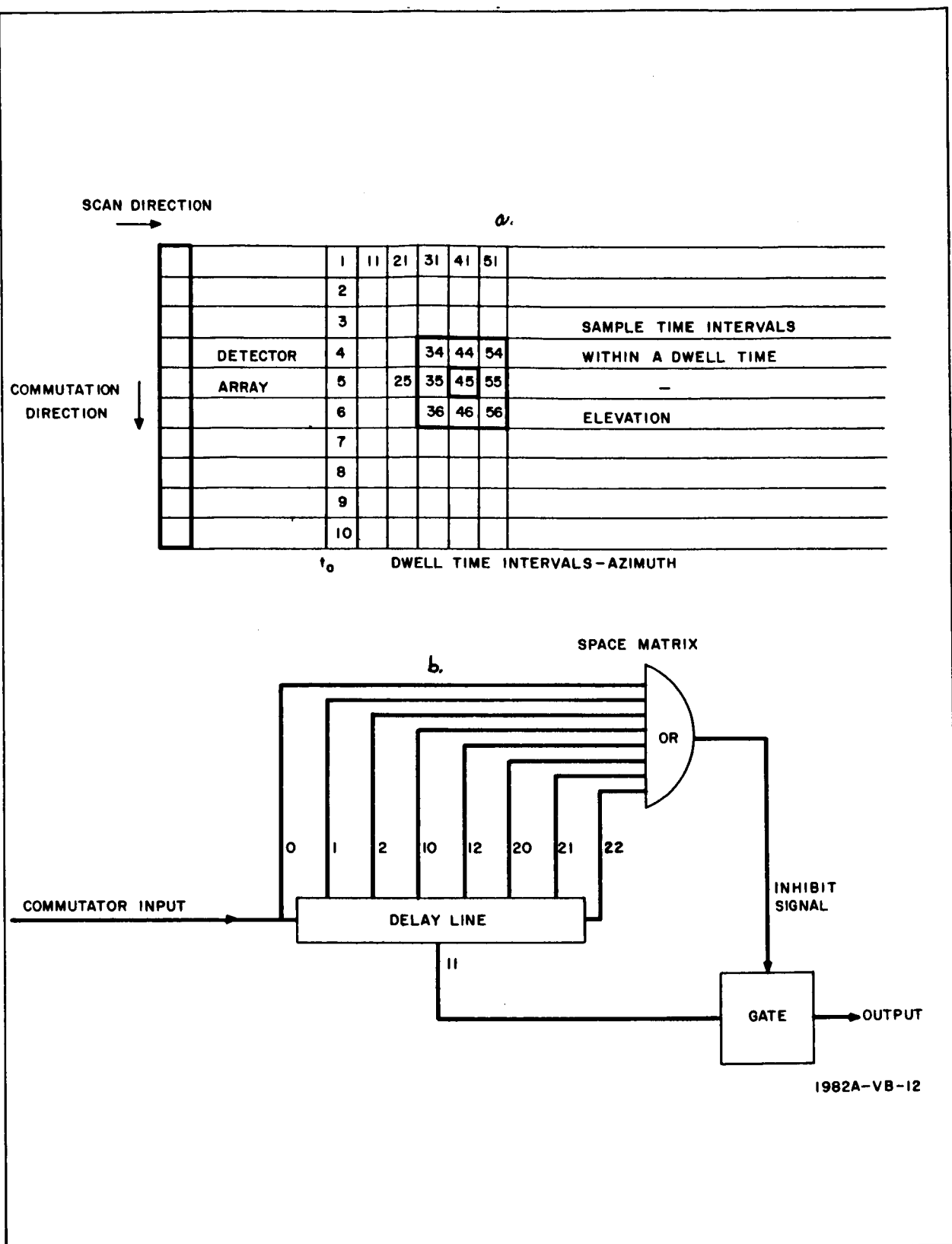


Figure 17. Space Matrix and Delay Line Concept

array is sampled only once in the period of one dwell time. Dwell time by definition is the time required for the detector to pass over a fixed point in space in the direction of scan.

The result of this scanning-commutating combination is to generate a space matrix of samples as shown in figure 17a. Each vertical column of the matrix represents the projection of the array in space at dwell time intervals. It is assumed that the time taken to sample one detector element is $1/10$ of a dwell time; thus, there are ten sample times in one dwell time. Since the electrical output of the commutator presents samples in a consecutive time sequence at one space sample per sample time, the elements of the space matrix may be numbered in terms of the consecutive sample times to facilitate a space-time relationship. For example, element 18 in the space matrix represents the 18th consecutive time sample and contains a measure of the radiant intensity of the scene within the confines of the matrix boundaries for this element at its space coordinates.

The criterion for digital space correlation was that a source of radiation exist on a given element of the space matrix but not on adjacent neighboring elements. If, for example, a source exists on element 45, according to this criterion the ring of elements surrounding element 45, comprised of elements 34, 35, 36, 44, 46, 54, 55, and 56, must not see any sources. This is depicted by the heavy lined rectangle drawn in figure 17a.

Since the matrix numbers in figure 17a represent the sample time sequence, it follows that element 34 will have been sampled 22 sample times before element 56; i. e., $56 - 34 = 22$. Also, element 45 will have been sampled 11 sample times before element 56, etc. To use information on element 56 to gate information on element 45, it is necessary to delay sample 45 until sample 56 is obtained. Thus, a delay line can be used to delay sample 45 for a time period of 11 sample times so it occurs coincident in time with sample 56. This same logic applies to all elements in the ring relative to the center element under evaluation. All delays, however, must be keyed to the last sample taken.

The delays required are computed by subtracting each sample time in turn from the last sample time applicable. For the case of evaluating element 45, the last sample is 56 and the corresponding delays are:

Last Sample	56	56	56	56	56	56	56	56	56
Space Sample	34	35	36	44	45	46	54	55	56
Delay (sample times)	22	21	20	12	11	10	2	1	0

A delay line may now be set up with taps, each occurring at the required delay along the line. All taps, except 11, (11 sample time delay) go to operate an inhibit gate which 11 must pass through to appear at the output. This is shown in figure 17b.

In summation, if a signal exists in space sample 45 and none within the outer ring of elements, the gate will not inhibit and the signal will pass through and constitute a signal from a point-source target lying within element 45. If a signal had also existed on one or more of the elements making up the ring, the gate would be inhibited and the signal on 45 would be blocked from reaching the output and thereby constitute an extended area source.

5.1.2 Practical Considerations

The simple concept described above is generally unsuitable in practice because the detector element size, which in turn sets the space sample, is made on the order of the blur circle size of the optical system used. Consequently, a point in the object plane becomes a blob as large as the element in the image plane. A result of this is that a point source scanned in azimuth develops a signal whose waveform is on the order of two dwell times long. The logic used in the sample theory would reject this case because it in effect covers two space samples. Therefore, it becomes necessary to allow for two space samples in azimuth to constitute point-source targets. Similarly, because the blur circle is comparable to the detector element, the probability of it touching two elements in elevation becomes quite high and it is necessary to allow for two space samples in elevation.

The sum of these effects is that the criterion for rejection is three or more consecutive samples in azimuth or elevation. The target domain

becomes a square comprised of 4 elements and an inhibit ring comprised of 12 elements as shown in figure 18.

At the present state of the art, it becomes impractical to have this many taps on a delay line and to have taps separated by sample time increments and dwell time increments on the same delay line because of the time spread between the two. For these reasons two separate delay lines are used, one tapped at sample time increments for elevation and one tapped at dwell time increments for azimuth. The space pattern for this logic is shown in figure 18b where the squares represent the inhibit samples for the space sample being evaluated shown in the circle. Figure 18c represents the type of signal flow for two lines.

It is believed that the small number of inhibit elements shown in figure 18b is sufficient. However, if this should prove untrue, more elements can be added at the expense of added complexity. It is also believed that one signal element is sufficient. Actually, all four of the center elements could be used for signal detection but it would only yield redundant information at the expense of additional pulse amplifiers.

5.1.3 Multiple Thresholds

All detection systems must have a detection threshold in order to keep the false alarm rate on noise down to some reasonable level. If a system employing delay line discrimination had but one threshold, it is conceivable that the high point of the intensity profile of an extended area target could exceed the threshold for no more than two dwell times and therefore appear as a real target. This is the case illustrated in figure 19 when only one threshold, b_2 , is used.

To circumvent this dilemma, two thresholds are used; b_1 , called the discrimination threshold and b_2 , called the detection threshold. The target detection criterion is then based on a point-source signal exceeding b_2 while the extended area rejection criterion is based on signals exceeding b_1 .

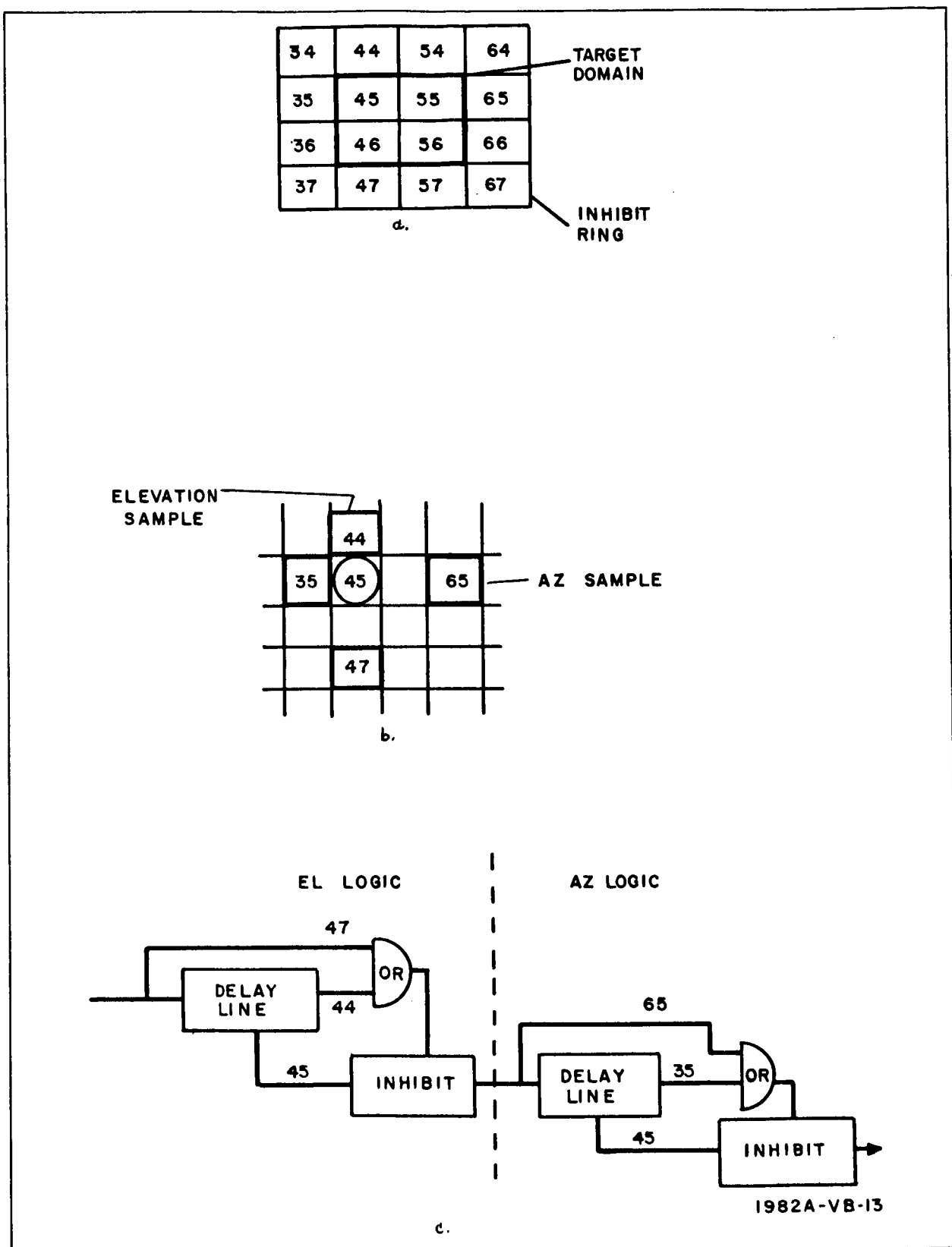


Figure 18. Delay Line Logic

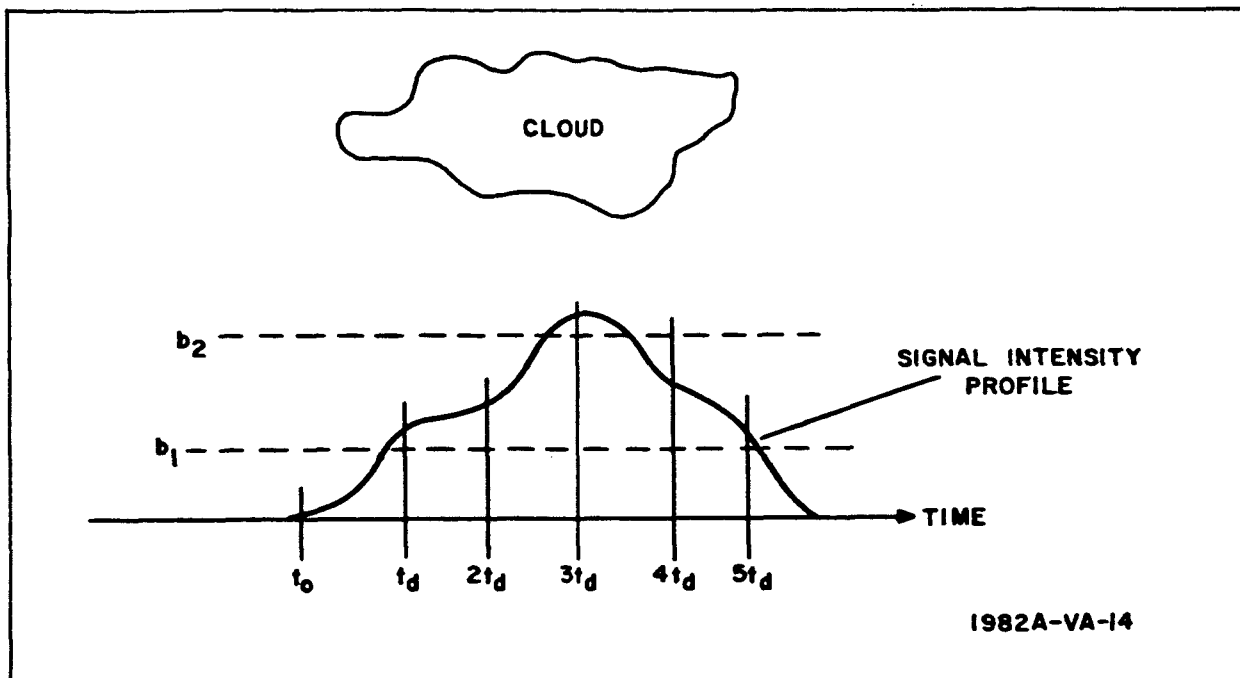


Figure 19. Multiple Thresholds

5.1.4 Series-Parallel Processing

Consideration of the series operation of figure 18c will reveal a serious shortcoming. It will be noted that potential targets are analyzed in elevation or the vertical direction first. If found acceptable, they are then analyzed in azimuth or the horizontal direction. If they again qualify they are displayed as real targets. This method is called series operation.

Consider an extended area source with a projecting edge which images on no more than two elements in elevation at the tip and then diverges into its large body as illustrated in figure 20. When column 3 is processed in elevation by the circuit of figure 18c, it will interpret a real target because only two elements are illuminated and pass on a signal to the azimuth logic. However, when column 4 is processed by the elevation logic it will interpret a false target because more than two elements are illuminated. Consequently, it will inhibit any signal from reaching the azimuth logic. The consequences of this are as follows. A signal from column 3 in figure 20, which is analogous to element 45 in figure 18b, reached the azimuth logic. Now, in

accordance with the logic functions depicted in figures 18b and c, the azimuth logic requires a signal on either element 35 or 65 for rejection. These element numbers correspond to rows 2 and 5 respectively in figure 20. It is obvious from figure 20 that nothing is accepted on row 2 and, although there is something on row 5, it will never reach the azimuth logic because it will be inhibited by the elevation logic being more than two elements high in elevation. Consequently, with no reject signals corresponding to elements 35 and 65, the signal on 45 which was passed by the elevation logic will also be passed by the azimuth logic. As a result, the system would erroneously display this projected edge as a true point-source target.

This deficiency is overcome by using a series-parallel approach wherein the azimuth logic is not deprived information, and the results of each logic output are composed before making a decision.

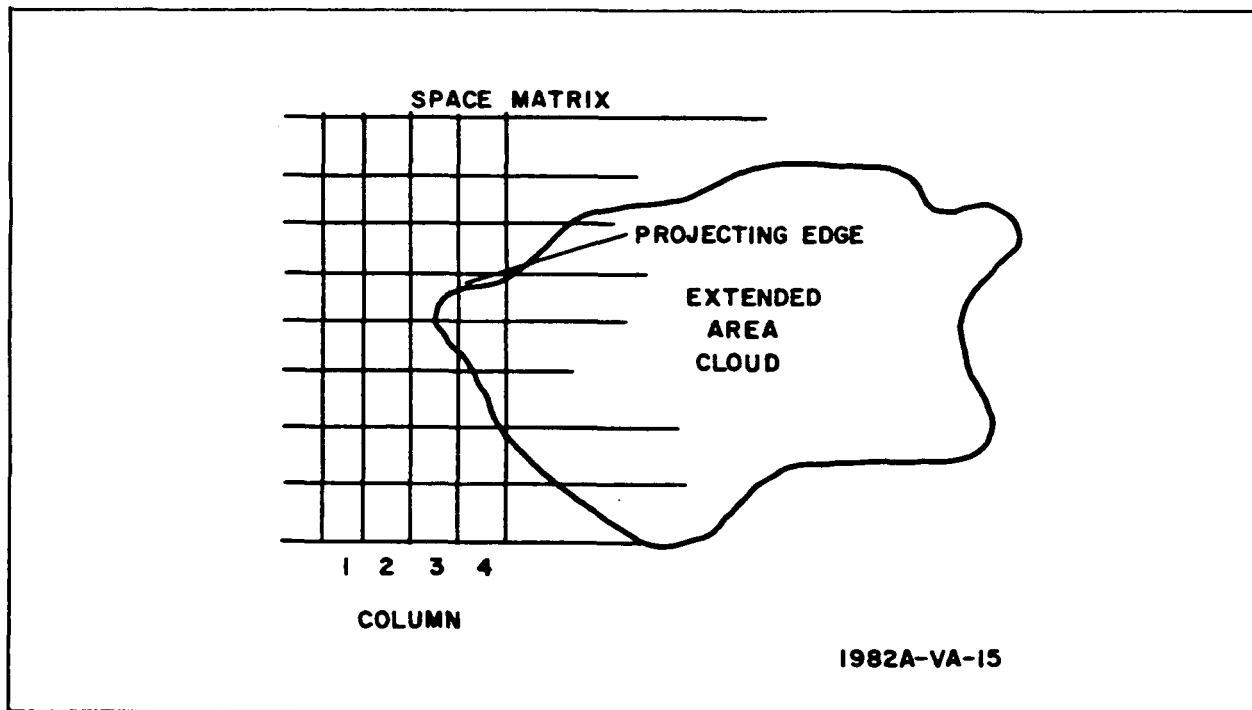


Figure 20. Projecting Cloud Edge

Figure 21 represents the signal flow and logic operations. The commutated signal samples are fed into threshold gates b_1 and b_2 which are sequentially activated in accordance with the timing diagram. Thus, half of each sample is operated on by b_1 and half by b_2 . The resulting outputs are seen to be time displaced in synchronism with A and \bar{A} clock signals respectively. The b_1 outputs are seen to control the elevation inhibit gate by virtue of ANDing with A after the OR gate. Only b_2 outputs leaving the delay line at the signal tap are presented to the inhibit gate by virtue of ANDing with \bar{A} at the AND gate. Any b_1 inhibit signals ANDed with A after the OR gate are stretched so that the inhibit gate remains activated after A ceases so as to block b_2 outputs which commence with \bar{A} . Any b_2 outputs which the elevation logic finds acceptable as targets in the elevation aspect are passed on to the azimuth delay line. The b_1 outputs which occur at the signal tap of the elevation delay line are passed on directly to the azimuth delay line by virtue of ANDing with A at the AND gate.

The azimuth logic processes the b_1 outputs in a similar way to control the final inhibit gate. If a signal is found acceptable as a target in azimuth, the final inhibit gate is left open. If there is a b_2 output present at the signal tap of the azimuth delay line at this instant, it will be passed on to display a real point-source target. The mere existence of a b_2 output at the signal tap of the azimuth delay line infers that it has already been found acceptable in elevation. If no b_2 were present it would mean that the signal was unacceptable in elevation and, even though the azimuth logic found it acceptable in azimuth and did not inhibit the gate, the lack of a b_2 signal leaves nothing to display; hence, no target is indicated. The b_1 outputs leaving the azimuth delay line signal tap are prevented from reaching the output by virtue of the \bar{A} ANDing signal.

In practice, the signal taps on the delay lines are moved just enough so that the b_1 and b_2 signals become coincident where desired and thereby eliminate most of the AND functions.

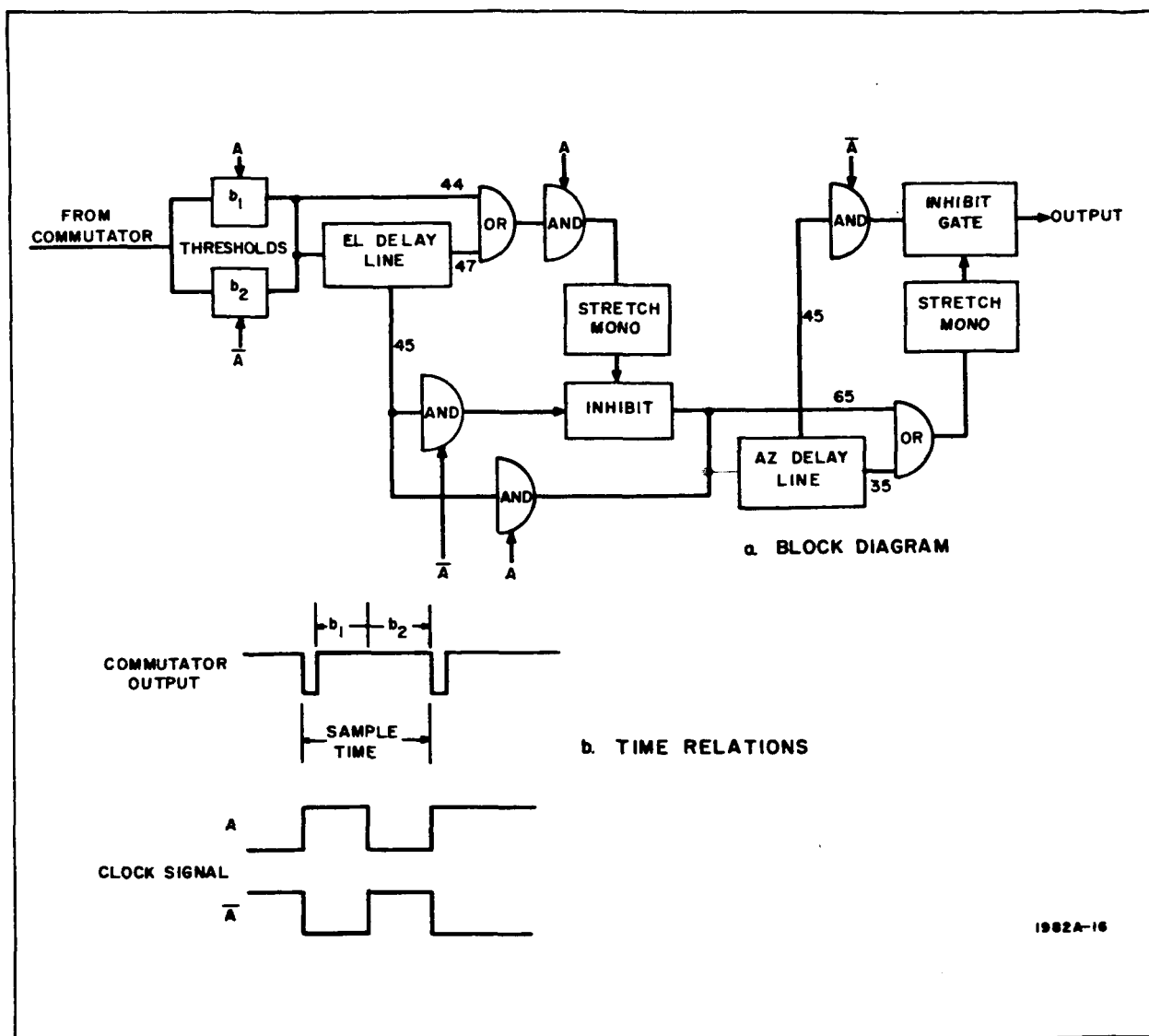


Figure 21. Series - Parallel Logic

5.1.5 False Targets

It will be observed that the sampling sequence shown in figure 17 is such that the samples from the ends of the array are consecutive; i. e., sample 11 from the top of the array follows sample 10 from the bottom of the array. This means that the end array samples are correlated in the logic circuits as though they were adjacent elements in space. This can lead to erroneous decisions. For example, if an extended area target just illuminated elements 9 and 10 because it was mostly out of the field of view, the logic circuits

would interpret this as a point-source target if there were no signals on elements 8 or 11.

To avoid this dilemma, two false targets are generated internally and interposed between the end samples, i.e., between 10 and 11. This eliminates the case cited above, since signals on the end elements will now be interpreted as extended area sources. This has the disadvantage of negating the end elements from ever detecting point sources. However, they are necessary to participate in the logic evaluation of their adjacent elements and, since they are at the ends of the array which could consist of many elements, this is not considered to be a serious disadvantage.

5.2 THRESHOLD LEVELS

It is desirable to keep the detection threshold as high as necessary to ensure a low false alarm rate. It is equally desirable to keep the discrimination threshold as low as practical to maximize the intensity profile gradient required of an extended area source for it to look like a point-source target at marginal intensities. However, if the discrimination threshold is too low, noise alone may induce b_1 inhibit signals which in turn may erroneously inhibit real point-source b_2 signals.

Consequently, the threshold values are chosen on a basis of "what is the probability of detection" versus "what is the probability of rejection if detected."

There is a total of five noise samples to be considered before each target decision. They are the signal sample being evaluated and the four inhibit samples. For a signal to be detected it must exceed the detection threshold b_2 and the inhibit noise samples must not exceed the discrimination threshold b_1 .

Let P_1 be probability that b_1 is exceeded by noise alone in one sample. Then the probability that b_1 is exceeded by at least one of the four inhibit noise samples becomes $1-(1-P_1)^4$.

Let P_2 be the probability that b_2 is exceeded by noise alone in one sample. From probability theory (reference 20) the false alarm probability is expressed as

$$P_{fa} = \frac{\ln 2}{n_{fa}} \left(P_{fa} \ll 1 \right) \quad (13)$$

where the false alarm number is

$$N_{fa} = \frac{\Omega T_{fa}}{\omega T_f} \quad (14)$$

For the breadboard feasibility system we may assume that one false alarm on the average of every hour is tolerable: therefore,

$$T_{fa} = 3600 \text{ seconds}$$

$$T_f = 1 \text{ second}$$

$$\Omega = 62,800 \text{ mr}^2$$

$$\omega = 1 \text{ mr}^2$$

$$N_{fa} = \frac{62,800 \times 3,600}{1 \times 1} = 2.26 \times 10^8$$

It may be seen that the false alarm probability for this system is

$$P_{fa} = P_2 (1 - P_1)^4$$

because $(1 - P_1)^4$ represents the probability that the noise pulse sneaking through the b_2 threshold would be inhibited by a noise pulse sneaking through the b_1 threshold, therefore preventing a false alarm. The effect is to reduce the false alarm number somewhat; however, it is insignificant and will be ignored here.

This false alarm number results in a b_2 threshold value of 5.8 times the rms noise and yields the detection probability curve shown in figure 22.

Since $1 - (1 - P_1)^4$ represents the probability that a detected signal will be inhibited, it is advantageous to keep this value low. Allowing for loss of 1 out of 1000 target samples this expression reduces to

$$1 - (1 - P_1)^4 = 0.001$$

$$P_1 = 1 - \sqrt[4]{0.999} = 0.0001$$

This represents a b_1 threshold value of approximately 3.5 times the rms noise.

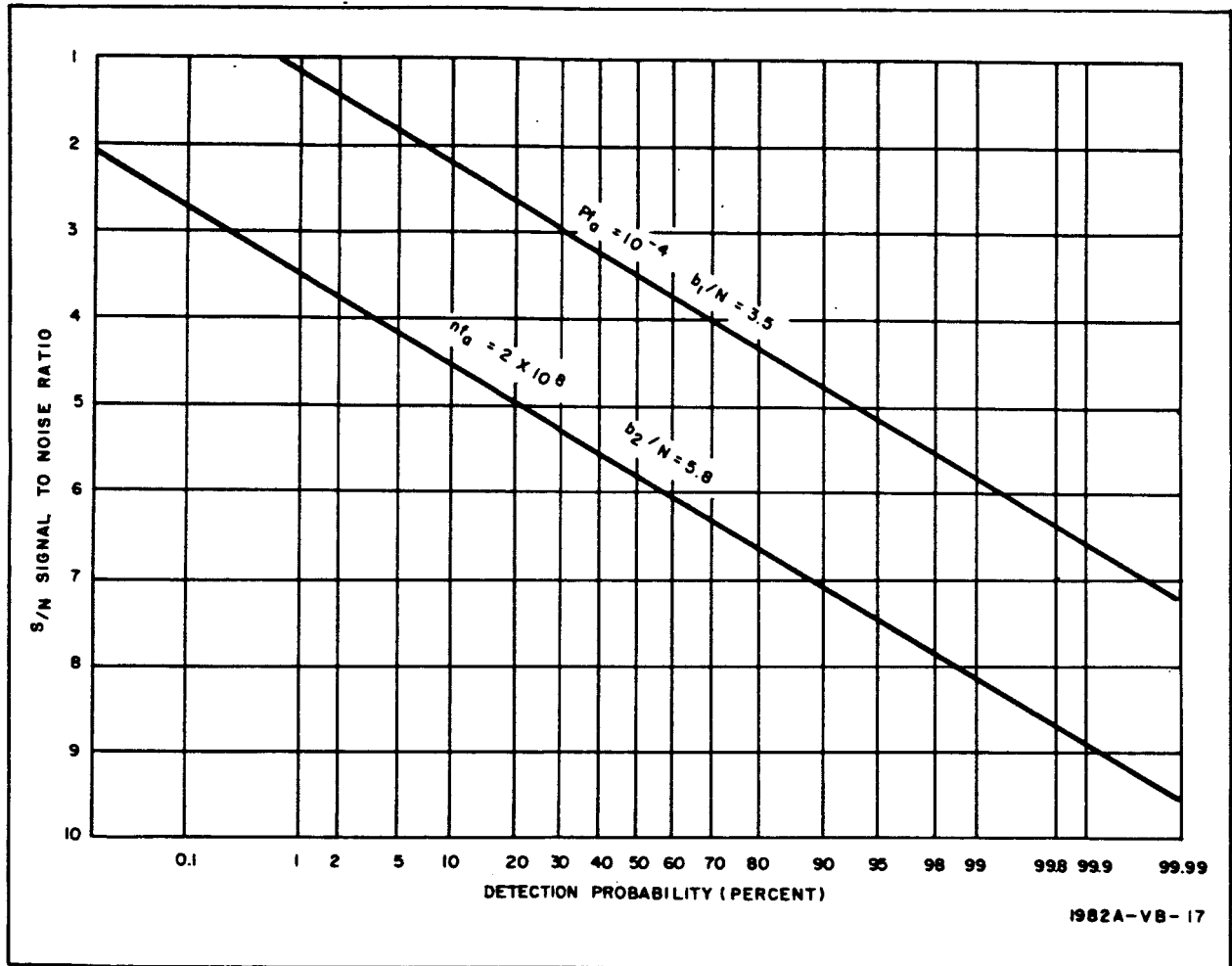


Figure 22. Detection Probability

5.3 ELECTRONIC FILTER

In a passive infrared scanning system the criterion for maximum sensitivity is peak signal to rms noise ratio. The electronic filter is generally optimized to yield the highest possible ratio. However, this is accomplished at the expense of signal fidelity which reflects as degradation in angular

resolution. If resolution is also important, a compromise between sensitivity and resolution must be made. Resolution is important in the feasibility breadboard not only because of trajectory prediction accuracy but because the delay line discrimination logic depends on it.

An exact filter analysis is beyond the scope of this report because it requires certain knowledge about many undefined variables, such as the blur circle distribution, nonlinear input, and impedances. Therefore, the corners are defined herein as a guide and then optimized in the laboratory under dynamic conditions.

5.3.1 High-Frequency Corner

The dynamic range of the Apollo vehicle signal from minimum to maximum irradiance was determined to be on the order of 10^4 . In the preceding section the detection and discrimination thresholds were seen to be approximately 6 and 3 times noise respectively and a signal-to-noise ratio required for a high probability detection, 99.9 percent, was 9. If the system is assumed to be capable of detecting the minimum irradiance value, the maximum signal-to-noise ratio that might be encountered is 9×10^4 . This is some 3×10^4 times larger than the discrimination threshold level. The rejection criterion is based on three or more dwell times, and therefore the real target must not exist for more than two dwell times. Hence, the high-frequency response of the amplifier must be adequate, so as not to stretch the maximum target signal beyond two dwell times. These relations are shown in figure 23.

From figure 23 the following simple single corner RC time constant can be derived.

$$\begin{aligned}
 b_1 &= S e^{-\frac{t_d}{RC}} \\
 e^{\frac{t_d}{RC}} &= 3.33 \times 10^{-5} \\
 \therefore RC &= \frac{t_d}{3.25 \pi} \\
 f_{\text{high}} &= \frac{1}{2\pi RC} = \frac{1.625}{t_d}
 \end{aligned} \tag{15}$$

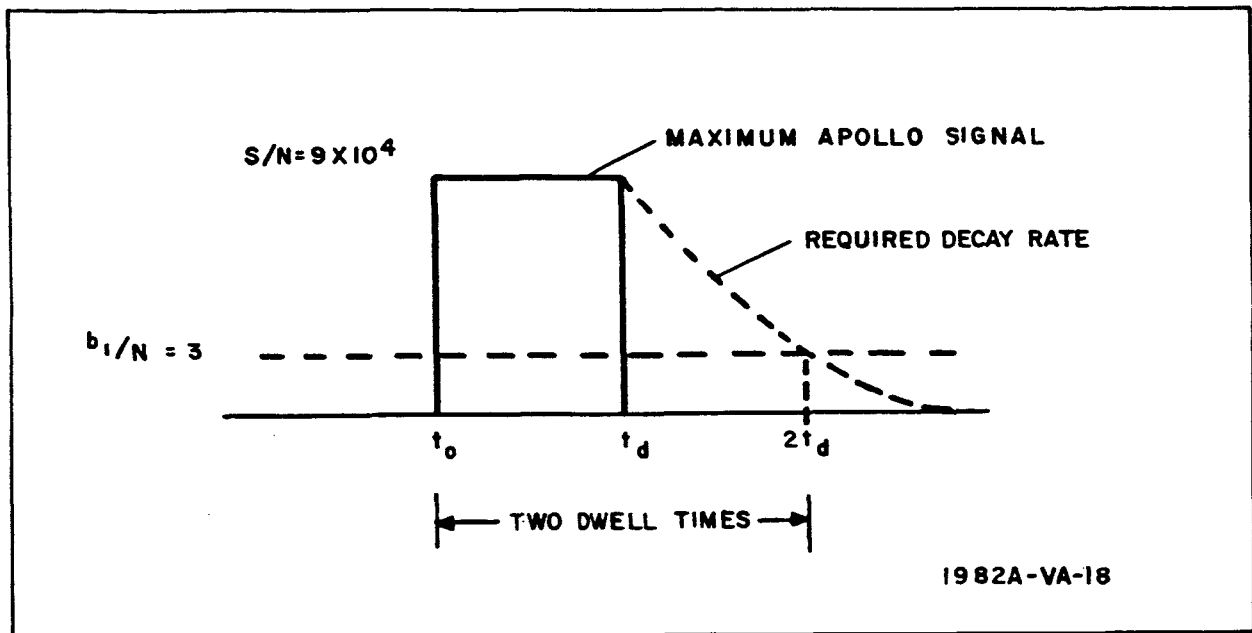


Figure 23. High-Frequency Criterion

5.3.2 Low-Frequency Corner

Since the rejection criterion is three dwell times, the low-frequency corner must be such that when the detector scans onto a cloud just bright enough to exceed the detection threshold, the low-frequency droop is small enough to maintain the signal above the discrimination threshold for at least three dwell times. This is illustrated in figure 24.

From figure 24 the following simple single corner RC time constant can be derived.

$$\begin{aligned}
 b_1 &= b_2 e^{-\frac{3t_d}{RC}} \\
 e^{-\frac{3t_d}{RC}} &= 1/2 \\
 \therefore RC &= 4.3 t_d \\
 f_{\text{low}} &= \frac{1}{2\pi RC} = \frac{1}{8.6\pi t_d}
 \end{aligned}
 \tag{16}$$

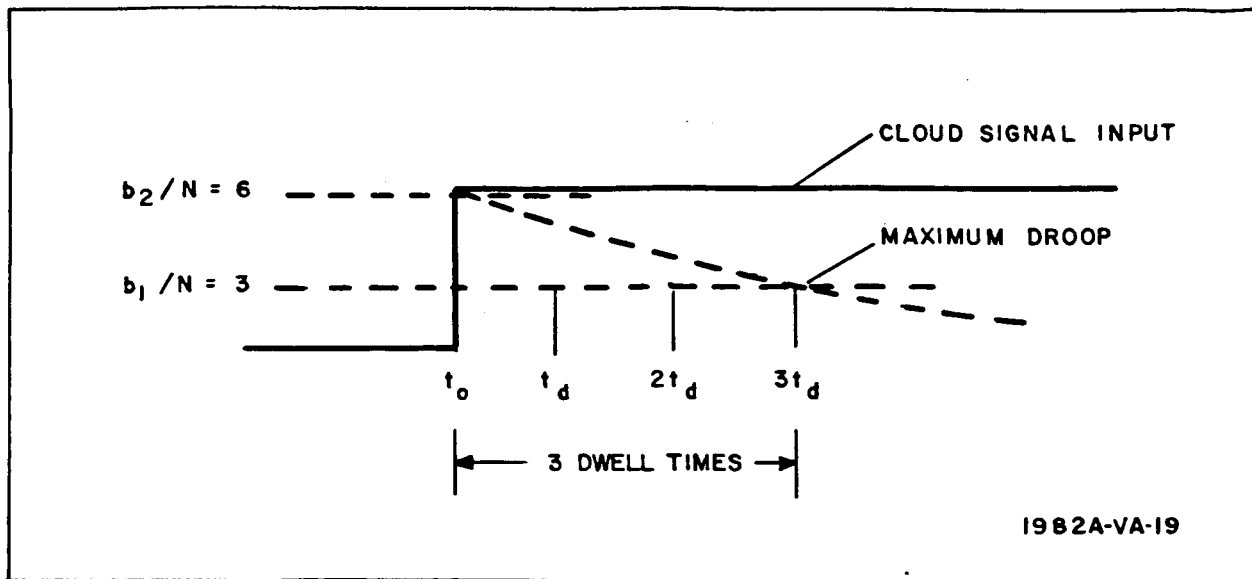


Figure 24. Low-Frequency Criterion

5.3.3 Noise Bandwidth

The 3-db bandwidth from the above considerations is seen to be

$$\Delta f_{3\text{db}} = f_{\text{high}} - f_{\text{low}} = \frac{(1.625 - 0.0373)}{t_d} = \frac{1.6}{t_d}$$

For purpose of comparison, the 3-db bandwidth using a simple RC filter for optimum peak signal-to-noise ratio is (reference 21).

$$\Delta f_{3\text{db}} = \frac{1}{5t_d}$$

Thus, the bandwidth is seen to be increased approximately 10 times for the sake of fidelity. The ratio of the noise bandwidth to the 3-db bandwidth is approximately 3/2 for the simple RC filter. Hence, the noise bandwidth for the feasibility model based on simple corners is

$$\Delta f_N = \frac{1.875}{t_d} \quad (17)$$

An increase in bandwidth of 8 times means an increase in noise of 2.8 times and implies a reduction in sensitivity of the broadband case over the optimum case. However, in the optimum case the peak signal can only reach 70 percent of the maximum because of its relatively narrowband filter. In

the broadband case, the signal reaches 100 percent. Therefore, the overall reduction in signal-to-noise ratio between the broadband and optimum cases is only 2 to 1.

Since S/N is a direct reflection on sensitivity, one can conclude that the penalty paid in sensitivity for fidelity is 50 percent.

5.4 COMMUTATION LIMITATIONS

The design guide specifications call for 1- milliradian resolution and a 360-degree-per-second azimuth scan rate. This means that 6280 elevation sweeps per second are required. The design guide calls for a 3-degree elevation field of view which is 524 elements. Based on these numbers, a commutation rate of $6280 \times 524 = 3,290,000$ bits per second would be required. The engineering feasibility model is required to have 10 elements in elevation and therefore requires a commutation rate of only 62,800 bits per second. Thus, we are concerned with commutator sampling rates of 63 kc to 3.3 mc in this application.

A state-of-the-art survey (reference 22) shows that the best low-noise, high on-off ratio, large dynamic range commutator is the roller deflected pressure contact type, but it is limited to a rate of 10.8 kc. For higher rates, solid-state switching devices must be employed. The highest frequency solid-state commutator on the market is a 50-kc unit made by Dyna Plex. This is hardly sufficient for the engineering model let alone the design guide. Apparently, the primary use of commutators today is in telemetry where 900-cps is the standard rate.

The characteristics of various switching transistors were investigated to ascertain limitations they might impose on commutator designs. The pertinent characteristics for two types which typify the present-day solid-state domain are listed below.

<u>Transistor Type</u>	3N-72	2N-2369A
	<u>Integrated Chopper</u>	<u>Matched Transistor</u>
Offset	50 to 200 μ v	1 to 10 mv
Spike $R_g = 1K R_{CL} = 30K$	50 mv peak-to-peak	30 mv peak-to-peak
Leakage	10^8 ohms	2×10^8 ohms
Max. Signal	10 volts	15 volts
Turnon time	0.2 μ sec	< 50 nsec
Turnoff time	1.0 μ sec	< 50 nsec
Cost	\$25/ea	\$10/ea

The offset voltage is due to the inherent unbalance in the device and, to a first approximation, represents the noise level which must be overcome by signal amplification before commutation. The integrated chopper is seen to be an order of magnitude lower in offset voltage.

The spike is due to the switching transient and may not be significant if it is of short duration. The spike associated with the matched switching transistors can be lower and considerably shorter in duration than the integrated chopper.

Leakage is important only when large numbers of elements are commutated and/or high temperature is encountered. This reflects as a higher noise level to be overcome.

The maximum signal is set by the breakdown ratings of the device and in turn restricts the dynamic range, relative to noise, that the commutator can handle.

The turn-on and -off times set the limits on commutation rates.

From these considerations it may be estimated that reasonably low-noise commutation may be obtained at rates less than 1 mc. Rates in excess of 10 mc may be achieved at somewhat higher noise levels and lower dynamic ranges. These are estimates in the sense that exact limits depend on associated design considerations such as source impedance, common load resistance, and shunt capacity. The estimated values are felt to be typical of these devices when used in the Apollo reentry detection application.

5.5 SPECTRAL FILTERING

Figures 12 and 15 illustrate the key considerations for selecting a spectral filter. The combination of the PbS cutoff wavelength and atmospheric absorption restricts the usable long wavelength cutoff to less than 3 microns. The short wavelength cutoff selection is based on target-to-background contrast. It may be seen that the background irradiance levels increase rapidly with decreasing wavelength while the 1000°K minimum target radiance decreases. Thus, the short wavelength cutoff is taken where the background irradiance increases faster than the target radiance. This occurs at approximately 2 microns, which is coincident with an absorption band. Thus, a long wavelength pass filter with a cuton wavelength of 2 microns is sufficient for this application.

5.6 DETECTOR

The detector specified for use in the engineering model is uncooled lead sulfide. The spectral response of lead sulfide, PbS, is seen to be a good choice in view of the spectral distribution of the reentry radiation shown in figure 10. The magnitude of irradiance was also found to be sufficient not to require cooling. This is quite significant, since it negates the added complexity and reduced reliability attendant with cooling mechanizations. In addition, high-resolution arrays are more readily attainable in thin films using photoetching techniques, thereby reducing detector costs some 10 times or more over single crystal detector types.

In the lead sulfide family there are a variety of detectivities, wavelengths, and time constants available. The reentry detection case should use the fast time constant variety detector.

Using the same theory as was used for determining the upper cutoff frequency wherein the time constant was based on minimum stretching of the maximum signal, the desirable time constant is

$$S = b_1 e^{\frac{t_d}{T}} = 3e^{\frac{t_d}{T}} = 9 \times 10^4$$
$$\therefore T = \frac{t_d}{3.25\pi} = 15.5 \text{ microseconds}$$

Without going into special detector development, the lead sulfide obtained for the engineering model has a time constant of 35 microseconds. In theory this limits the maximum signal to

$$S = 3e^{\frac{159}{35}} = 180 \text{ (S/N ratio)}$$

This is some 500 times smaller than the maximum signal to be encountered. However, this time constant is based on small signal levels and it is characteristic of PbS to exhibit smaller time constants for large signal levels. It is, therefore, anticipated that this will be an acceptable value. If this should not be the case, the time constant can be reduced by some sacrifice in detectivity.

The detectivity of the PbS material received is in excess of 2×10^{10} cm/watt-sec^{1/2}.

5.7 SENSITIVITY PREDICTION

The noise equivalent sensitivity may be defined by the following equation (reference 23):

$$\phi = \frac{4F \alpha \sqrt{\Delta f_n}}{\pi D_o E_{ff} \Gamma D^*} \text{ w/cm}^2 \quad (18)$$

Values for these parameters are given in the section on design specification and design considerations. They are enumerated below.

F = focal ratio = 1

α = field of view = 10^{-3} radian

D_o = aperture diameter = 30.5 cm

E_{ff} = optical efficiency = 50 percent

Γ = signal conversion factor = 1

Δf_n = noise bandwidth = $\frac{1.875}{t_d}$

D^* = detector detectivity = 2×10^{10} cm/watt-sec^{1/2}

The dwell time, t_d , based on the design specifications of 360 degrees per second scan velocity and 1 mr field of view is

$$t_d = \frac{1}{6280}$$

Inserting these values in equation 18 yields

$$\phi = \frac{4 \times 10^{-3} \sqrt{1.875 \times 6280}}{3.14 \times 30.5 \times 0.5 \times 2 \times 10} 10 = 4.6 \times 10^{-13} \text{ w/cm}^2$$

The minimum target irradiance at the maximum line-of-sight reentry range was computed to be $2.16 \times 10^{-12} \text{ w/cm}^2$. The above sensitivity would yield a signal-to-noise ratio of 4.6 for this case. From figure 22 this is seen to correspond to a 11-percent probability of detection. If the sensitivity is doubled the detection probability would become 99.9 percent.

6. SYSTEM MECHANIZATION

The completed engineering model feasibility subsystem is shown in figure 25 and a pictorial drawing of the major components in figure 26.

A parabola is mounted rigidly to an optical bench with the array detector affixed to a support located at the image plane. A flat mirror is rotated by a turntable attached to the opposite end of the optical bench. The rotation of the flat mirror causes the scene to scan by the parabola and hence the image to scan across the detector. This arrangement facilitates generating the desired scanning motion without the attendant problems of moving heavy optics and flexing wires.

The detector array is mounted perpendicular to the direction of scan. Each detector output is applied directly to a molecular preamplifier located on the mount behind the detector. The preamplifier outputs are commutated and processed by the logic circuits wherein the discrimination occurs. The accepted point-source targets are then presented on a display scope. These functions are illustrated in the block diagram of figure 27. Figure 28 illustrates the system wiring diagram.

Only a small portion of the mirror rotation cycle will produce usable scan time because the flat will not fill the parabola over the entire cycle. Keeping the flat within practical dimensions yields a usable scan of approximately $1/2$ radian in azimuth. This is some 50 times longer than the elevation height of 10 milliradians and thus is ample for feasibility study purposes.

6.1 PARABOLA

The primary mirror is a first surface, aluminized and overcoated, 12-inch diameter, $f/1$ parabola fabricated by Tinsley Laboratories on an annealed, $3/4$ -inch-thick vertex substrate specified to possess a maximum on-axis blur circle of 1.5 arc minutes. A photograph of the main deck showing the parabola is given in figure 29.

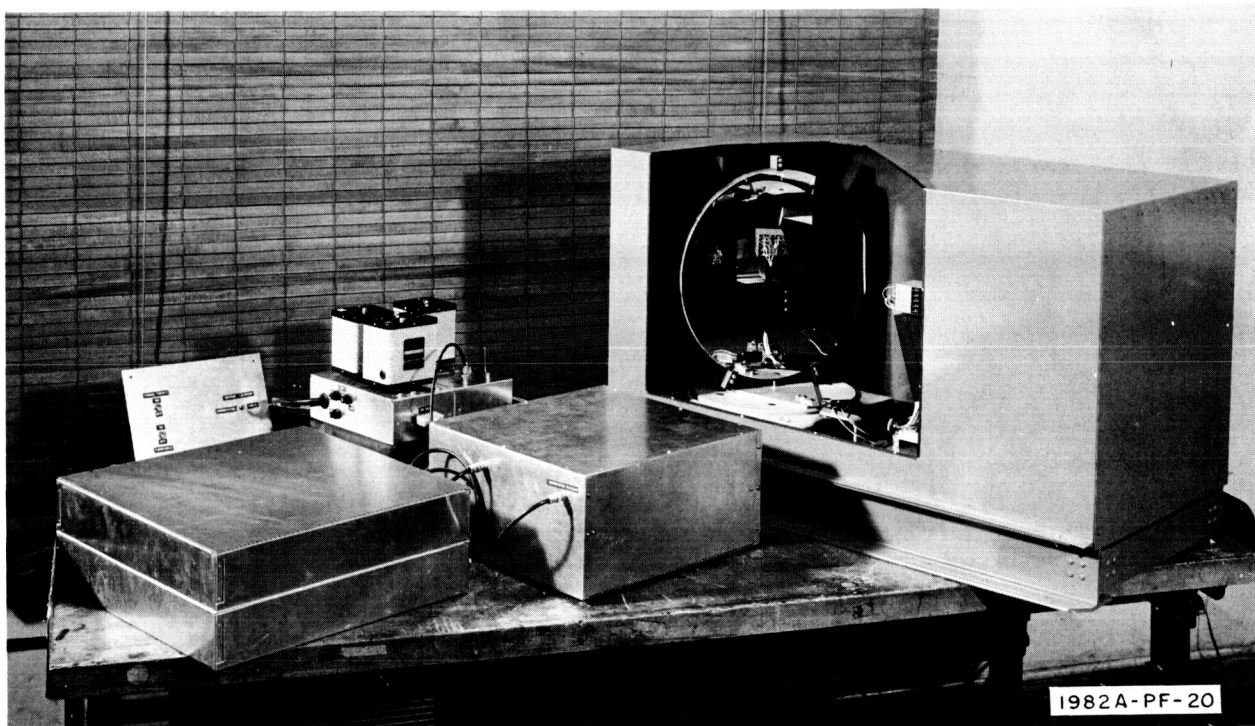


Figure 25. Feasibility Model

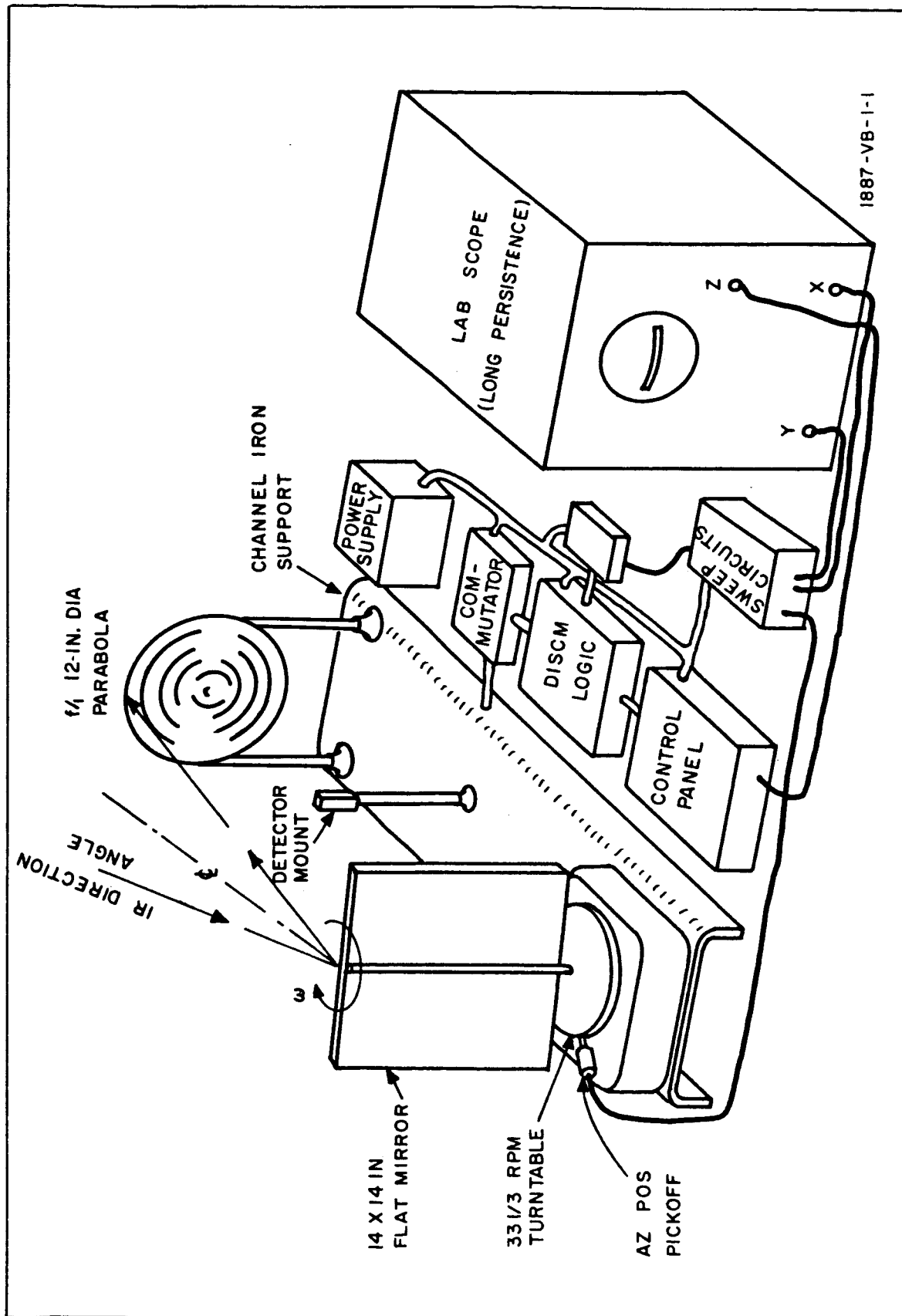


Figure 26. Feasibility System

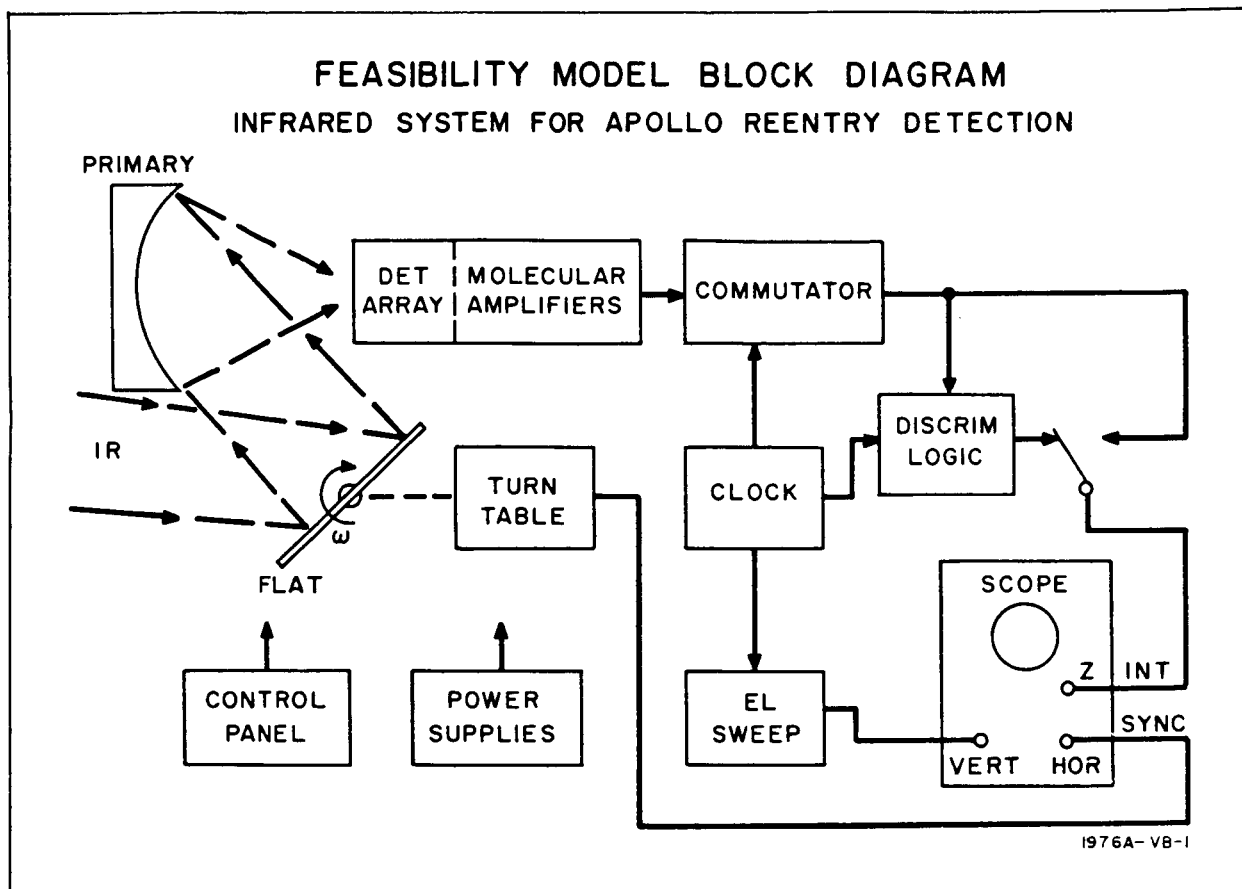


Figure 27. Engineering Model Block Diagram

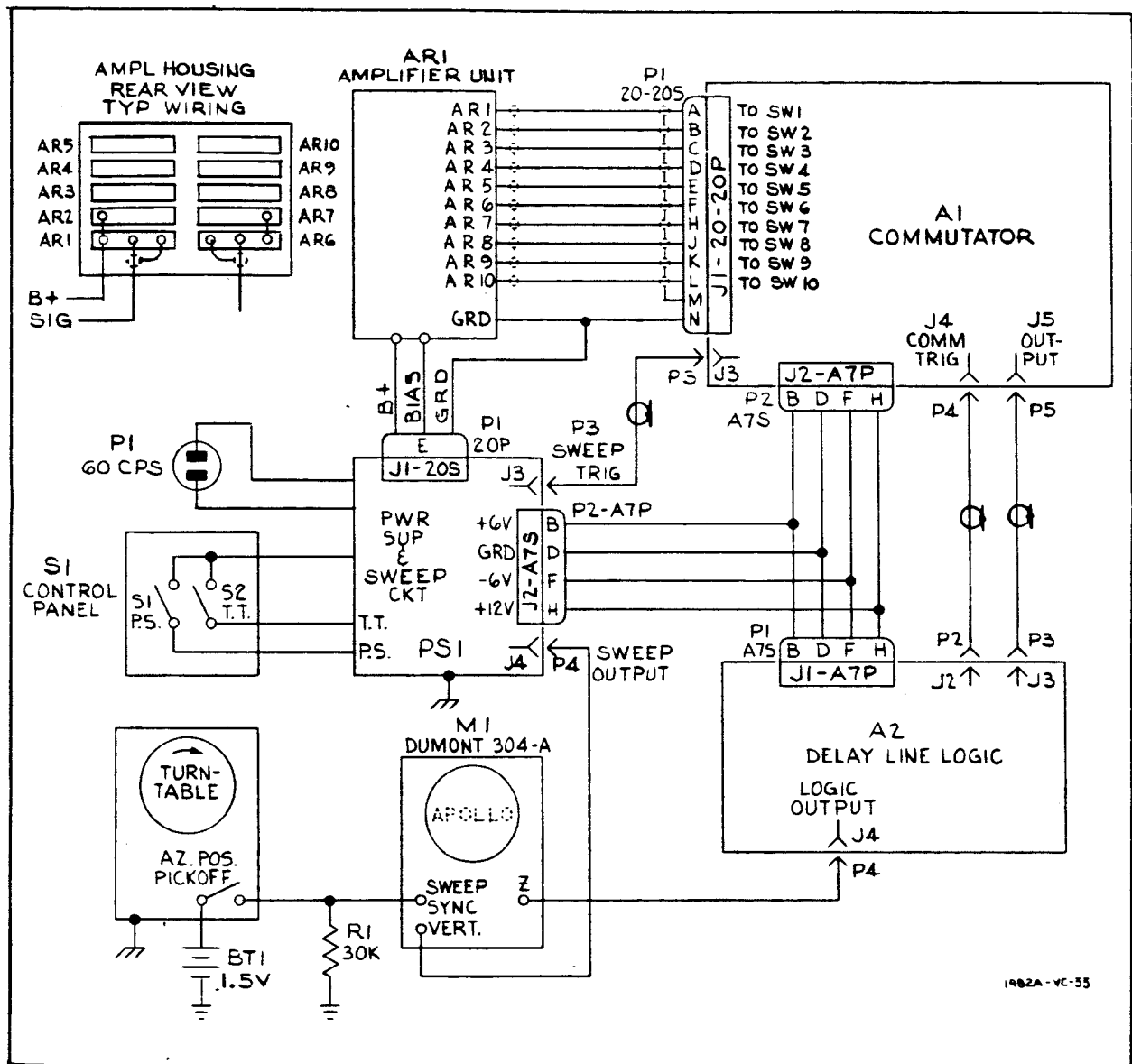


Figure 28. System Wiring Diagram

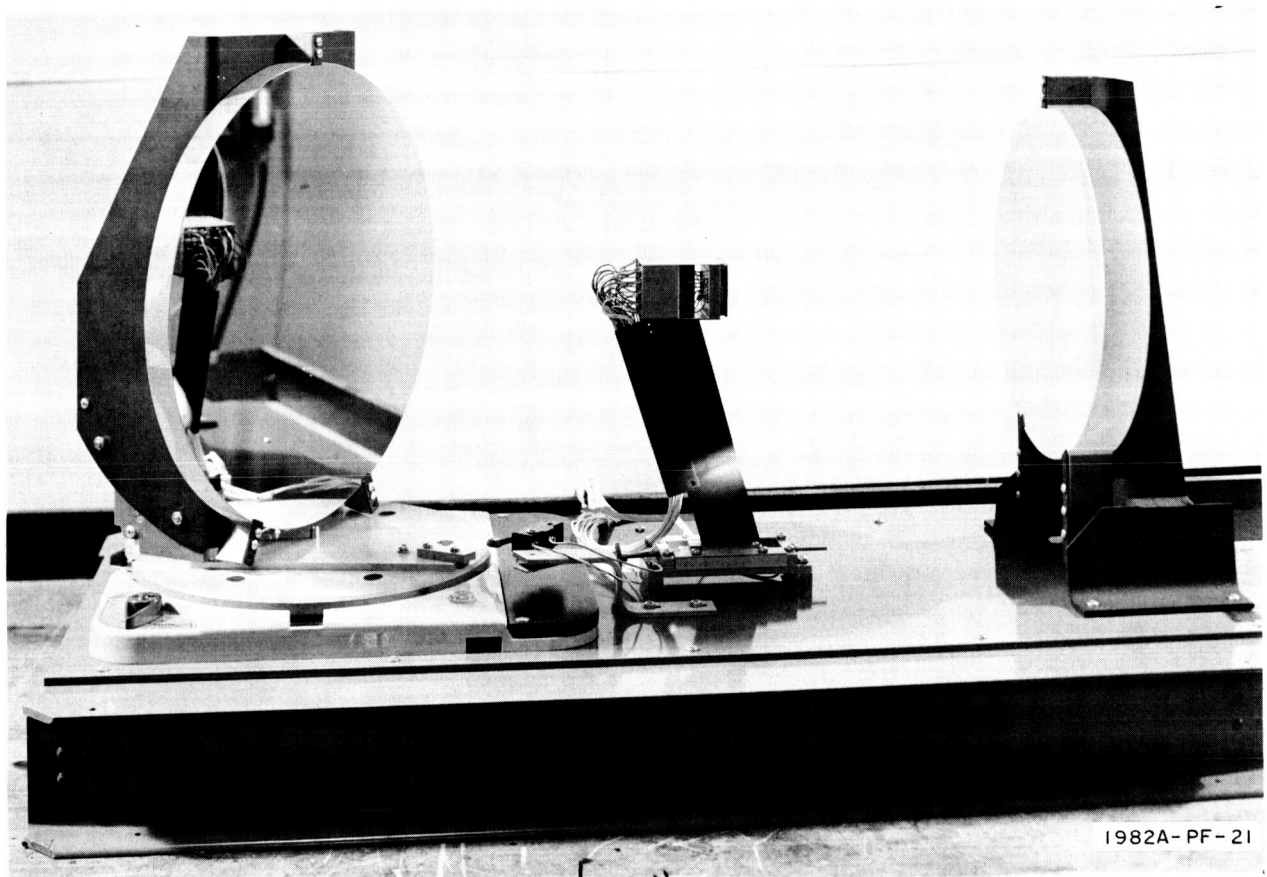


Figure 29. Radiometer

6.2 FLAT

The scanning mirror is a 15-inch-diameter, first surface, aluminized and overcoated, optical flat fabricated by the 3B Optical Company on a 1-inch-thick annealed substrate, specified to be flat within two fringes. The flat is mounted on the turntable with adjustment provided to change the tilt, thereby facilitating a range of elevation look angles without tilting the optical bench. The flat and its mounting are shown in the photograph of figure 29.

6.3 TURNTABLE

A studio-type high-fidelity phonograph turntable (Thorens TD-124) is used for rotating the flat. This type was chosen because it possesses a large inertia (10 pounds table mass) which is desirable to ensure uniform scanning velocity of the relatively heavy flat.

Aside from having four speeds, a vernier speed adjustment is also provided. Thus, the 33-1/3 rpm speed is readily reduced to 30 rpm. Inasmuch as the scan angle at the image plane is twice that of the rotating flat, the turntable speed of 30 rpm or 1/2 cycle per second generates a scan speed of 1 cps at the image plane. This is required to meet the contractual specifications.

The turntable is rigidly attached to the main deck as shown in figure 29.

A microswitch is attached to the turntable to provide a pulse for synchronizing the azimuth sweep of the display scope.

6.4 SPECTRAL FILTER

A 1.9-micron long wavelength pass filter was obtained from Optical Coating Laboratory. It possesses an average transmission in excess of 81 percent between 2.1 and 3.4 microns and is completely attenuated at the short wavelengths. It consists of an interference coating on a 1-inch diameter by 0.03-inch-thick Vycor substrate. The filter is mounted immediately in front of the detector on the detector mount.

6.5 DETECTOR

The detector is a 10-element uncooled PbS array obtained from Eastman Kodak Company and is their type P-3. Each element is 0.012 by 0.012 inch which scales to a 1-milliradian instantaneous field of view when used with the 12-inch-diameter f/1 parabola.

The electrode design was patterned after techniques developed on Air Force contract AF 33(616)8449 wherein high resolution is obtained through photo-etching techniques and electrical isolation is achieved by use of common biasing electrodes. Figure 30 shows a photograph of a completed detector, and figure 31 indicates the wiring connections. The detector is mounted on the front of the detector-amplifier support just behind the spectral filter shown in figure 32.

Typical characteristics of the elements are:

- a. Resistance - 90 to 130 kilohms
- b. Time constant - 35 to 50 microseconds
- c. Detectivity - $3.2 \text{ to } 4.2 \times 10^{10} \text{ cm/watt-sec}^{1/2}$

6.6 MOLECULAR PREAMPLIFIERS

The preamplifier, electronic bandpass filter, and postamplifier have all been integrated into a single package designated as the molecular preamplifier.

The primary function of the molecular preamplifier is to amplify the low-level detector signals to a suitable level for commutation with the least noise insertion. In this application, however, additional requirements are imposed. Because of the multitude of amplifiers that may be required in an operational sensor, upward of a hundred, the power consumption must be small. Second, because of the large dynamic range of signals that may be encountered, on the order of 10^5 , the amplifier must not block or stretch real targets and must still recover rapidly from large signals to maintain full gain and good noise figure for small signals. This latter requirement tends not to be compatible with high gain and good noise figure and low-power consumption, but it has been achieved here without sacrificing these other characteristics through the use of molecular amplifier techniques developed under Air Force Contract AF 33(616)8449.

In an effort to obtain an amplifier design which would recover quickly from these large signal levels, both instantaneous AGC and dc coupling were investigated but both approaches deteriorated the amplifier performance in

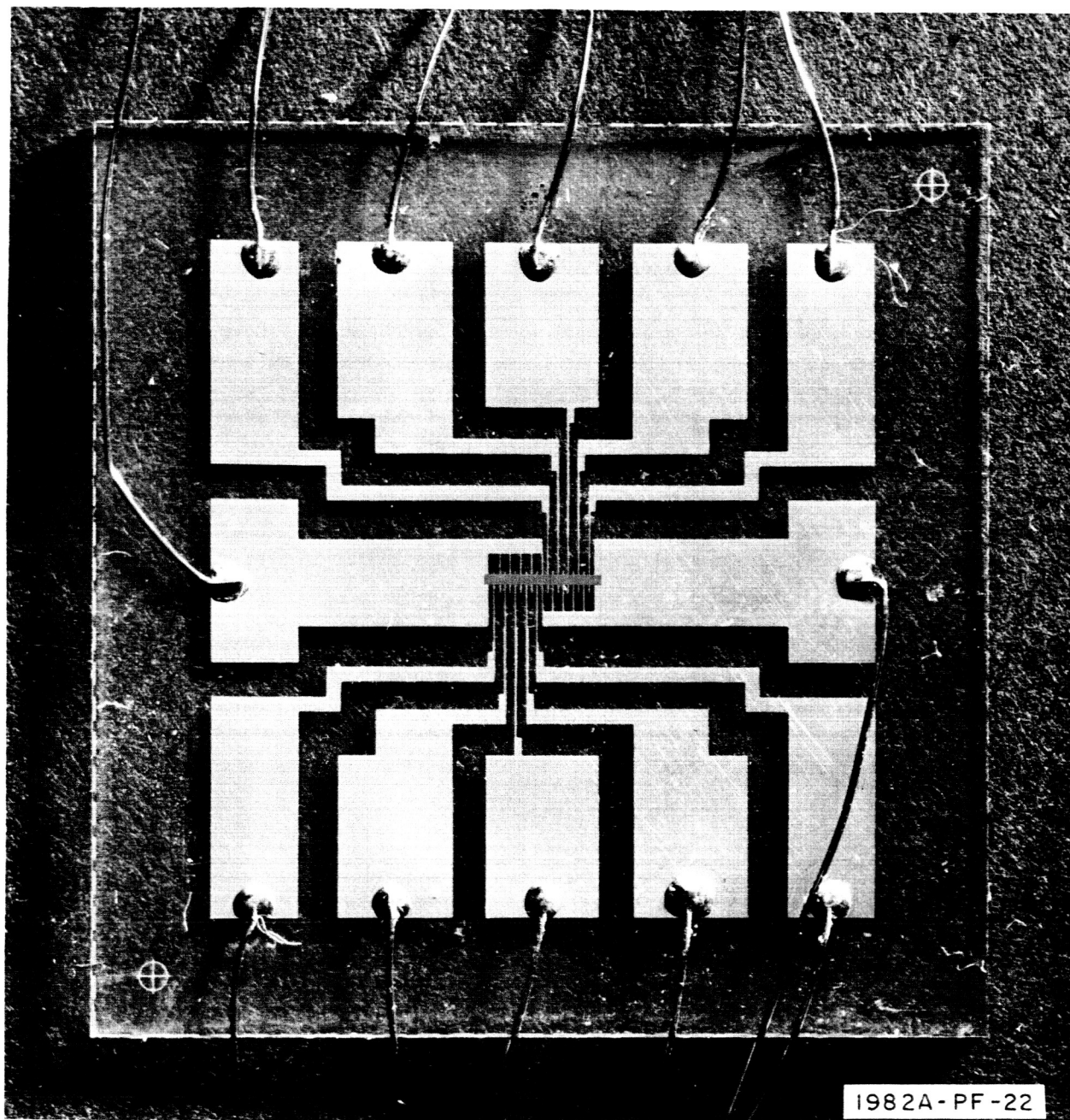


Figure 30. Array Detector

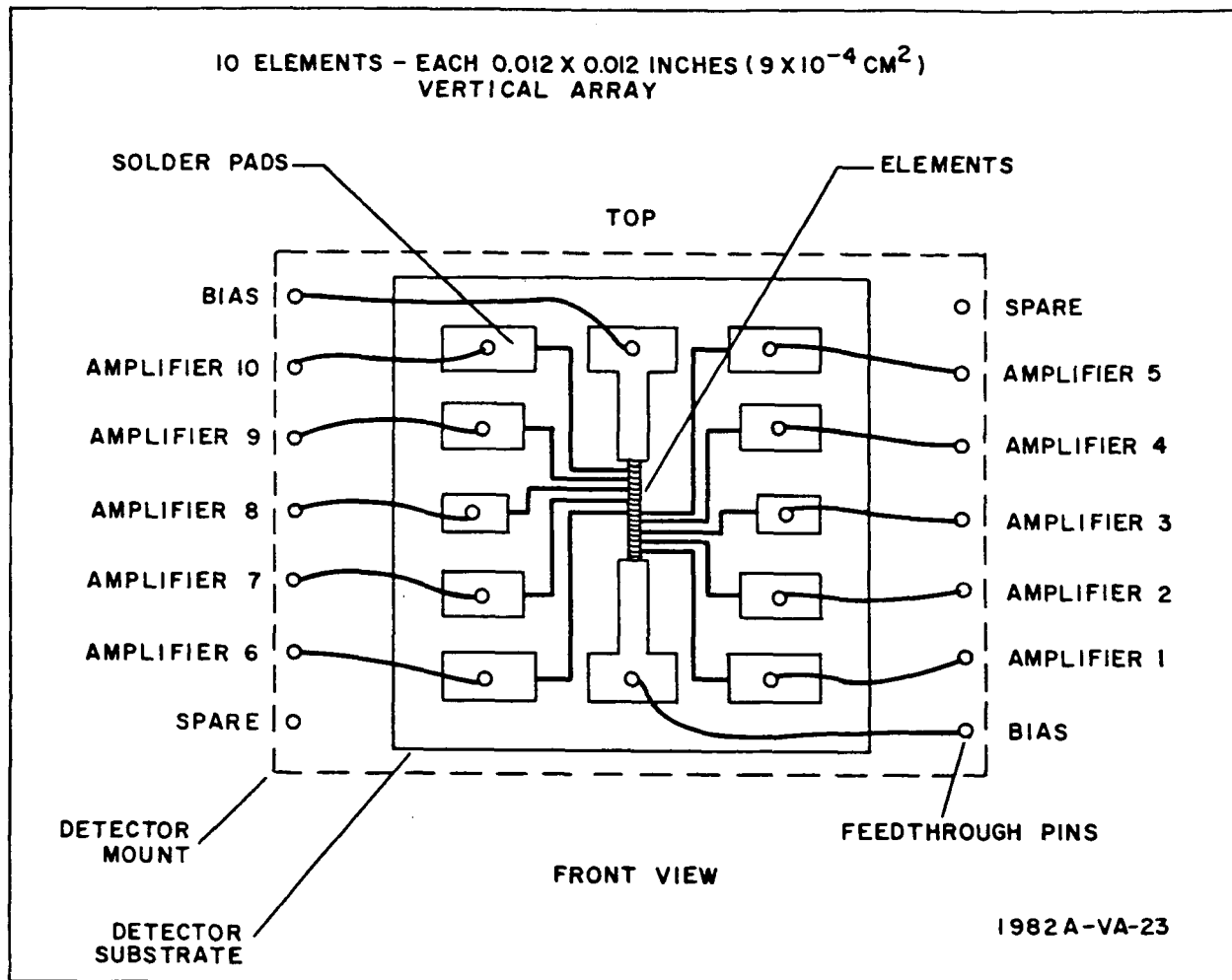


Figure 31. Detector Electrode Connection

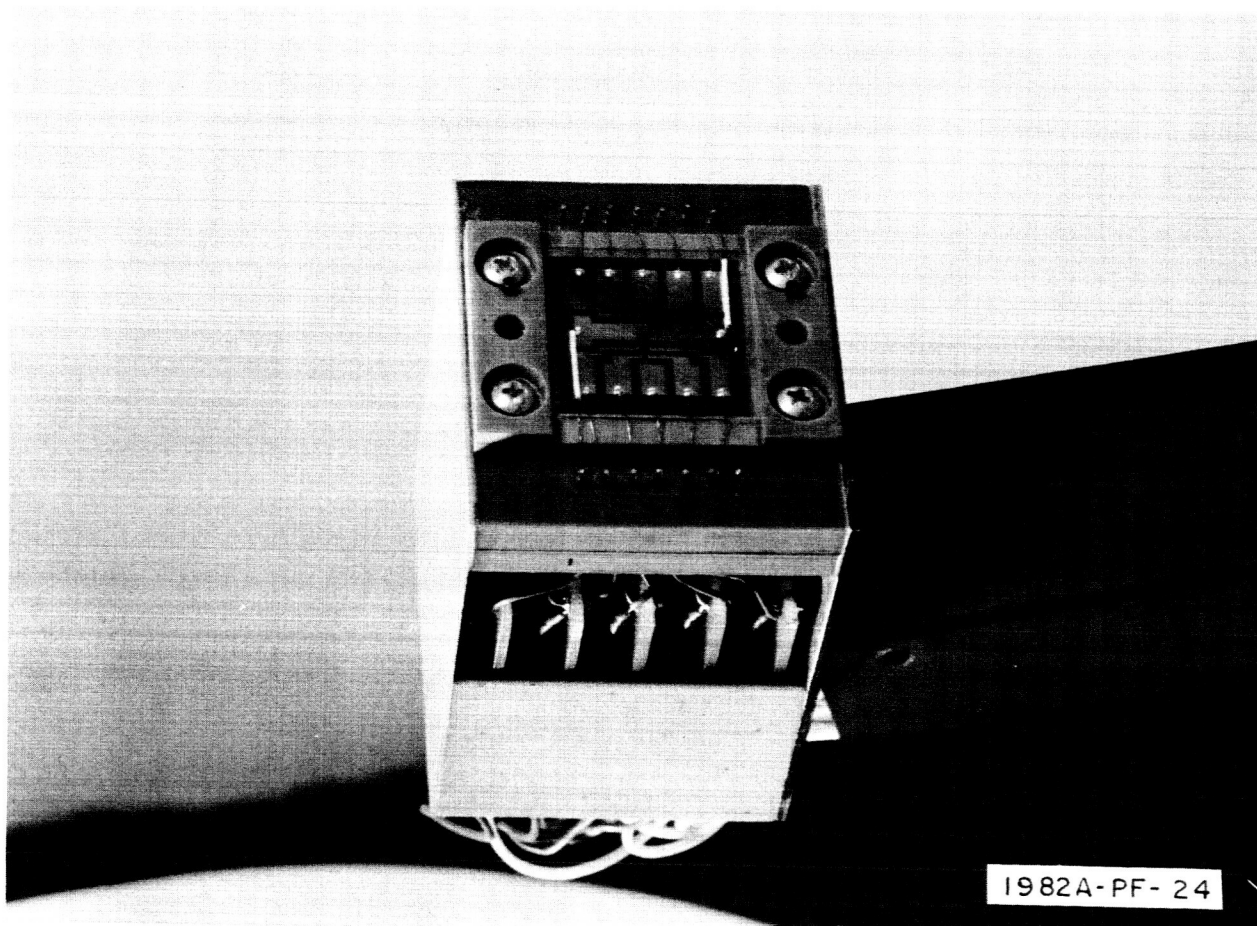


Figure 32. Detector-Amplifier Mount

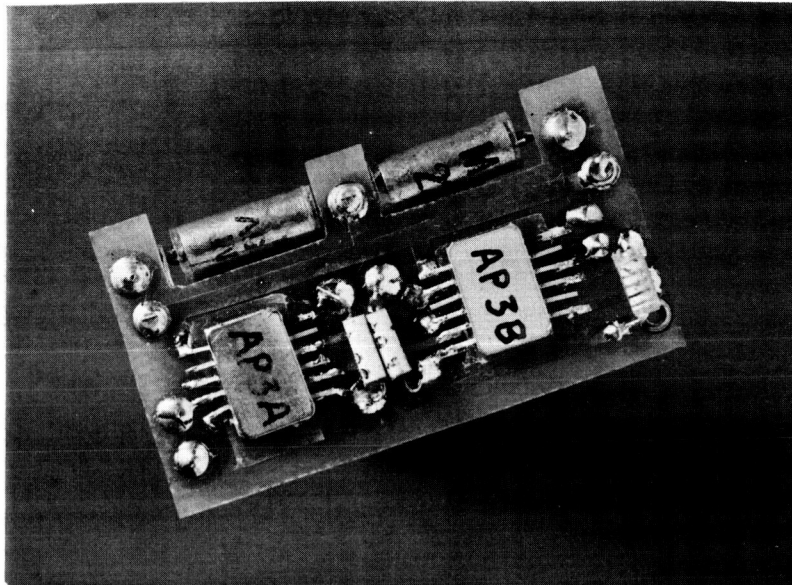
noise figure and/or power dissipation to a great degree. The design settled upon employs electronic filtering between the detector and preamplifier input and low-frequency interstage coupling with diode limiting. This is illustrated in the schematic of figure 33.

The employment of the electronic filter up front and the use of large valued coupling capacitors necessitated using some conventional components with the molecular amplifiers. These are the components shown in figure 34 mounted on both sides of the board containing the molecular amplifiers.

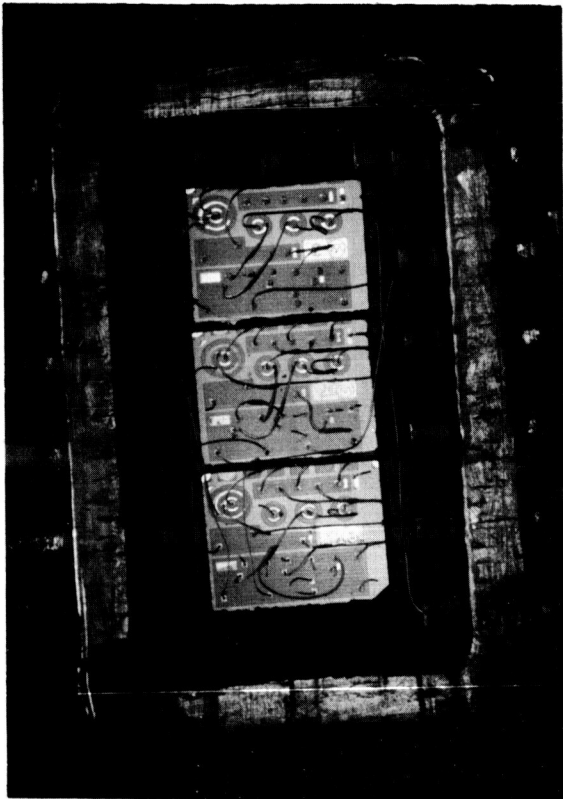
A previously developed molecular stage was used extensively in the scanner preamplifiers, and this stage contained diffused resistors. At least one wafer (≈ 50 stages) was fabricated with thin-film resistors. These stages were intended for front end use as the film resistors have lower current noise levels and higher resistivities than diffused resistors. (The higher resistance value is needed for base bias on the first stage as loading seriously affects noise figure.) It was found that the wire bonds of the film resistors became noisy after several weeks in use.

When the problem was discovered, the molecular laboratory personnel modified the stage resistor contact pads. The noisy bonds were apparently made through the resistance film to a metal pad. The bond is only good where metal-to-metal contact is made. The idea was to apply just the slight pressure and temperature to obtain the metal-to-metal bond through the oxide resistor film. The metal pad is now run out from beneath the resistor film and a good metallic bond can easily be made.

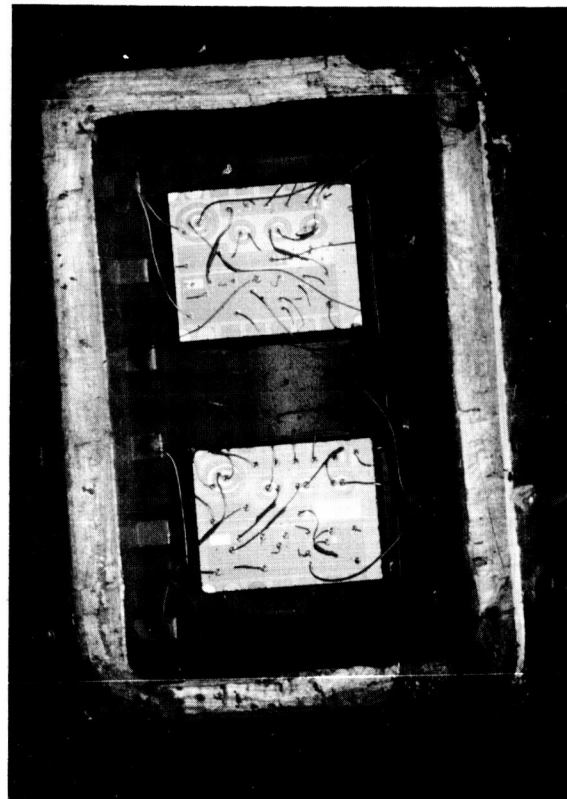
To avoid delay in system fabrication and test, a small external resistor was used on each preamplifier input stage to obtain the desired results. The new thin-film stages are now available for any additional system fabrication.



a. COMPLETE UNIT



b. CHIPS AP3A



c. CHIPS AP3B

1982A-PF-25

Figure 34. Molecular Amplifier

Table 2 lists the amplifier characteristics.

TABLE 2
MOLECULAR AMPLIFIER PERFORMANCE CHARACTERISTICS

G	= Adjustable from 1,000 to 20,000
NF	= 6 db
R_o	< 1 k Ω
R_{in}	\approx 100 k Ω
f_h	= 5 kc
f_L	= 450 cps
E_o MAX	= 5 vp
P_d	< 20 mw

6.7 COMMUTATOR

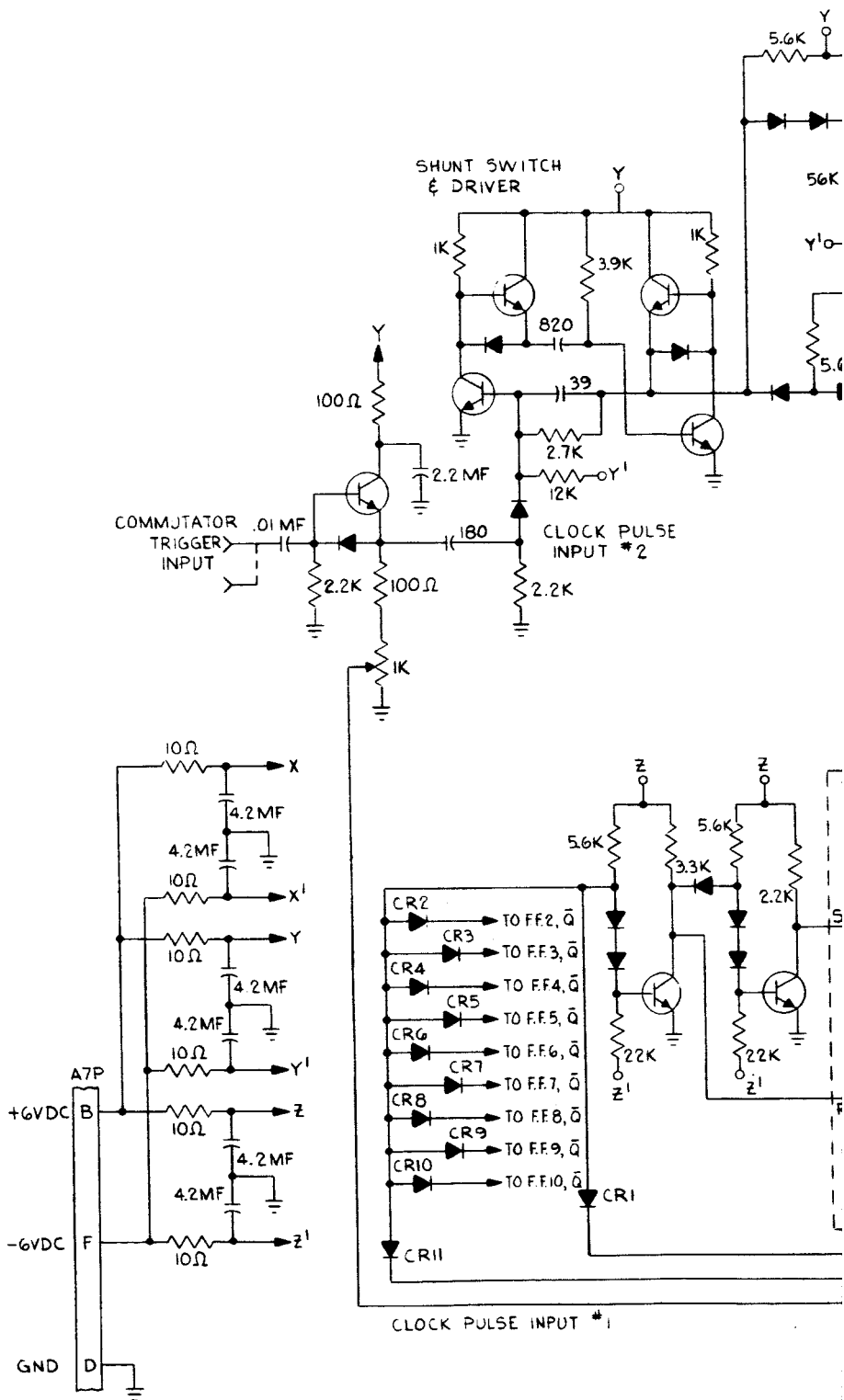
The commutator design is shown schematically in figure 35. Pertinent characteristics of the commutator are:

Commutation frequency	= 70 kc
Sample time	= 10 μ sec
Open-state impedance	\geq 10 megohms
Closed-state impedance	\leq 15 ohms
Offset voltage	$< \pm 200 \mu$ v
Switch spike	< 100 mv
Max. signal	= 8 v
Dynamic range	= 40

In general, a commutator can be thought of as a type of switching device which sequentially controls the transmission of "N" multiple inputs to a common load. To effect the method of time sharing electronically, a sequential generator supplying N electrical discrete clocked outputs is usually employed. The sequential generator outputs govern the transmission path of N series switching elements which connect multiple signal channels to a common load.

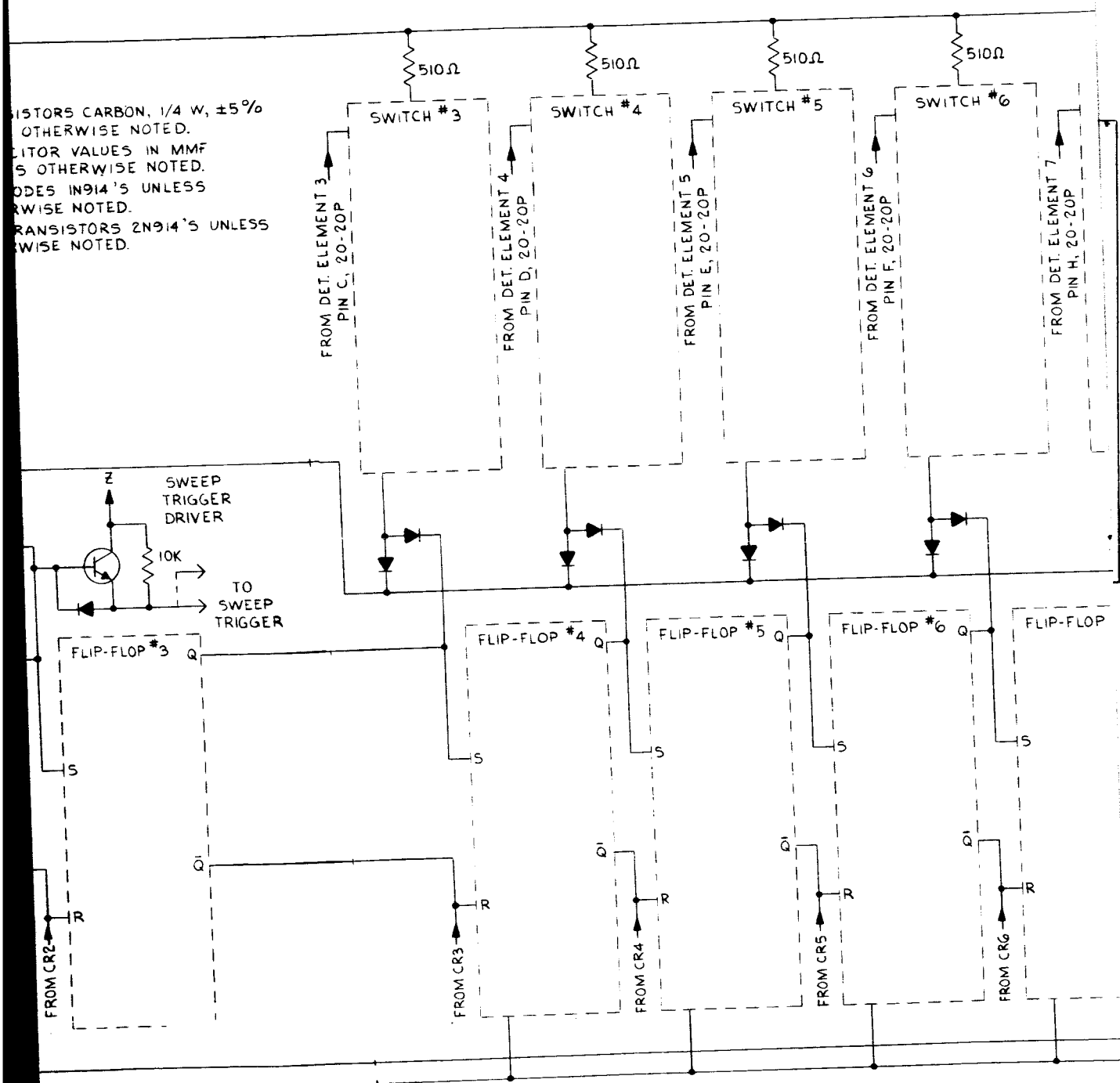
The commutator block diagram, figure 36, shows an open-end counter employed as the sequential generator, and switching elements which utilize integrated chopper transistors in the Bright configuration. A monostable multivibrator, referred to as the sample mono, is employed to provide a finite time separation between samples via NAND logic driver circuitry. During this time separation interval a shunt switch short circuits the common load, and discharges any existing capacity across the load, clearly defining each sample. The action of the shunt switch also establishes a definable reference level between samples and aids in minimizing switching transient effects introduced by imperfect isolation of the switching elements' drive circuitry.

The open-ended counter portion in the commutator block diagram shows the components and logical arrangement required for a counter with 12

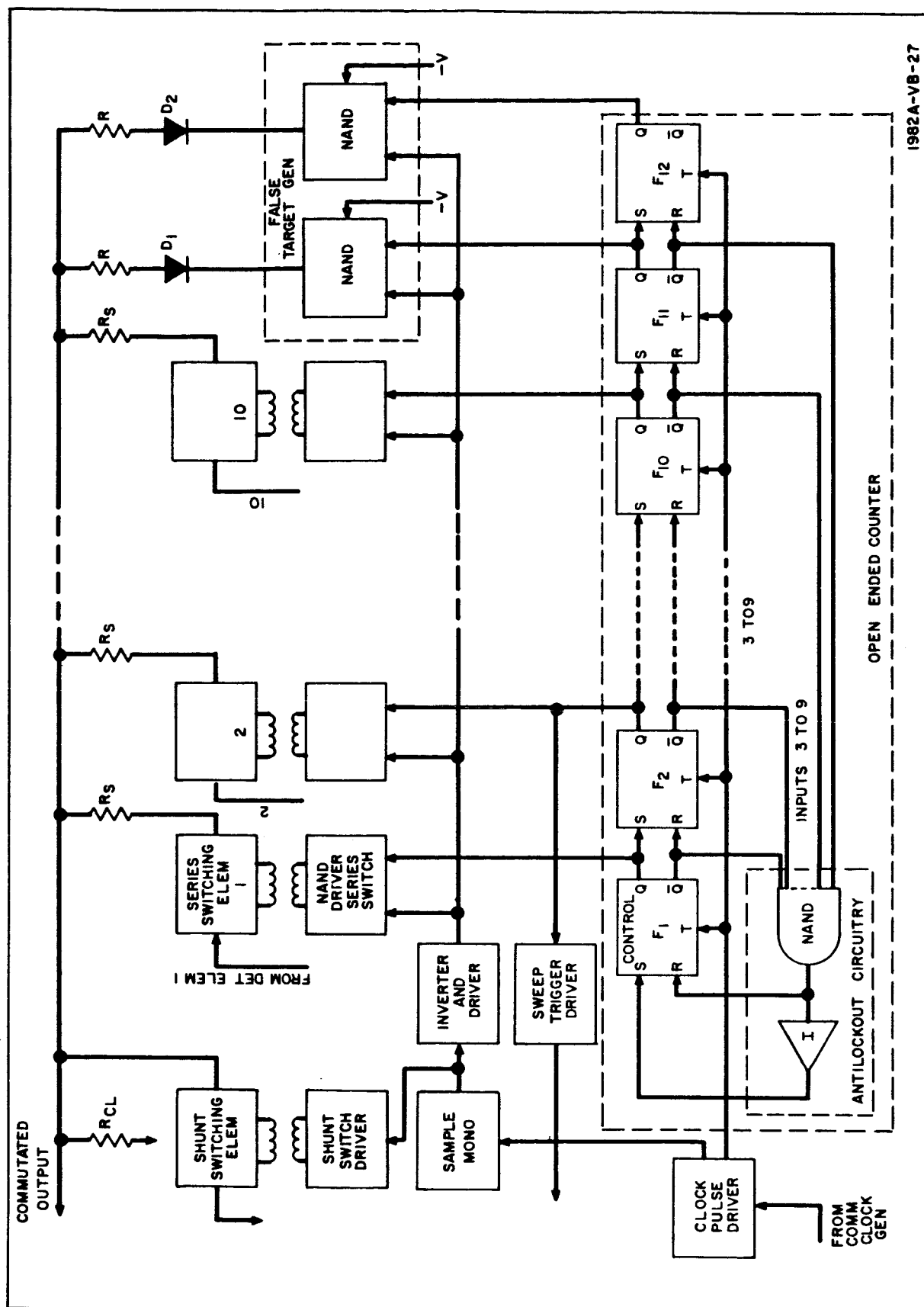


6-17-1

RESISTORS CARBON, 1/4 W, $\pm 5\%$
 OTHERWISE NOTED.
 CAPACITOR VALUES IN MMF
 UNLESS OTHERWISE NOTED.
 DIODES IN 914'S UNLESS
 OTHERWISE NOTED.
 TRANSISTORS 2N914'S UNLESS
 OTHERWISE NOTED.



6-18-1



positions. The first flip-flop, F1, is the control flip-flop for the counter, and its inputs monitor the condition of the counter in order to ensure that proper operation is obtained. In this type of arrangement, the condition of the final flip-flop, F12, is not monitored since the logic is open ended. The flip-flops are basically connected in a manner similar to a shift register which transfers the condition of flip-flop F1 down the counter. This type of logic provides that within 11 clock pulses (N-1), the counter will be operating correctly regardless of the initial conditions of the 12 flip-flops or any improper state that may be accidentally introduced.

The clocked pulses which are transferred down the counter are combined with the sample mono's inverted output via NAND circuitry to determine the conduction time of each series switching element. A positive clock pulse is used and a combination of lead edge triggering for the sample mono and trail edge triggering for the counter is utilized. A shunt switch is activated once per clock pulse during the time interval between samples; this action is depicted in the timing diagram (figure 37) where the signal appearing at the common load for two random samplings and the two internally generated false targets are shown. This signal pulse train corresponds to a complete elevation scan where sampled signals appear at positions 5 and 6, and false targets are internally generated and appear at positions 11 and 12 in the absence of system noise in any channel.

The last two flip-flops, F11 or F12, act together with the sample mono in a similar manner as do the logic blocks determining the conduction interval of the series switching elements. However in the case of the last two positions, predetermined artificial signals are internally generated and diode coupled to the common load via diodes D1 or D2.

A clock pulse driver and a sweep trigger driver are also shown in the block diagram. The clock pulse driver accepts clock pulses from the clock generator and supplies coincident clock pulse outputs of different amplitude to the counter and sample mono. The sweep trigger driver couples the output from flip-flop F2, to the sweep circuit for the purpose of synchronized sweep generation.

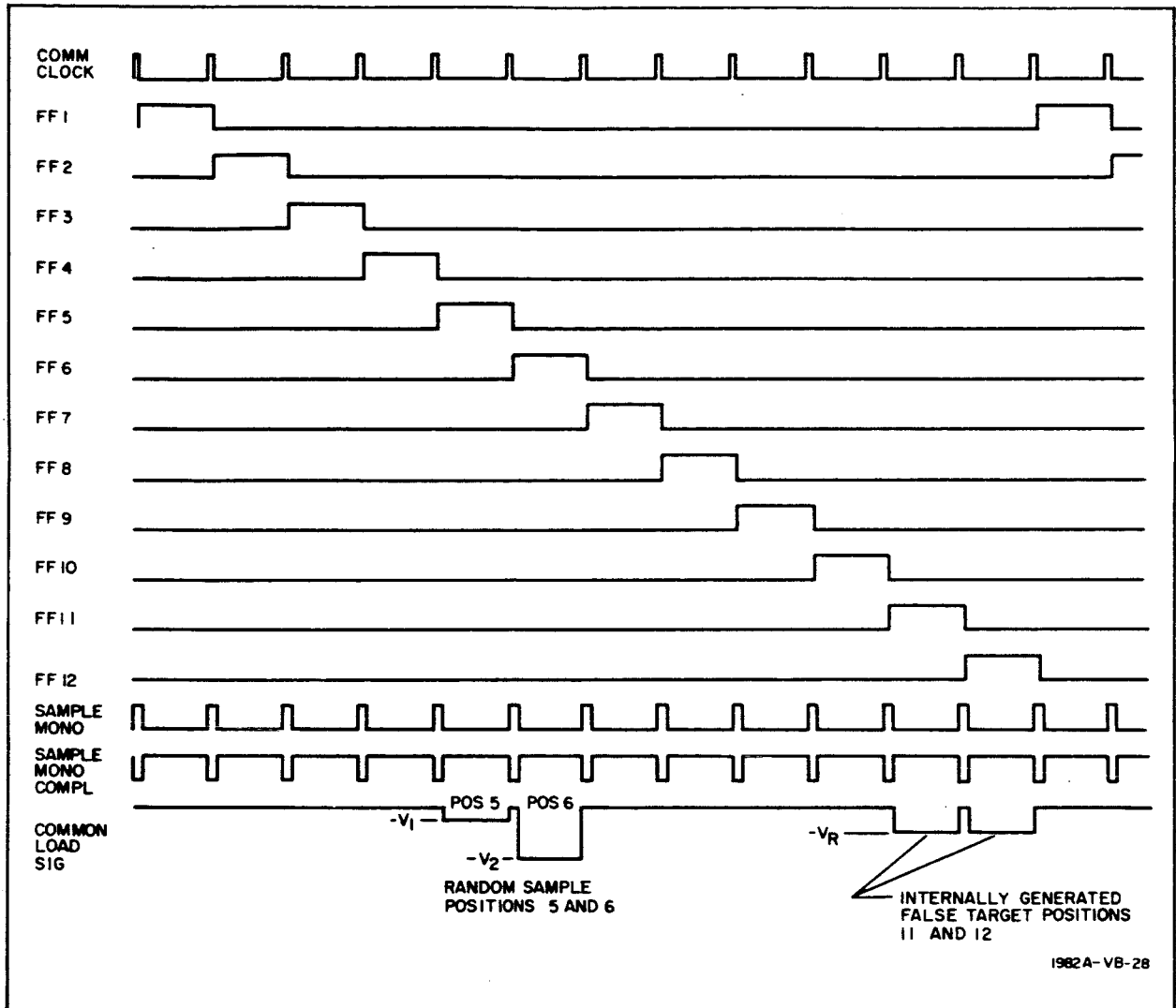
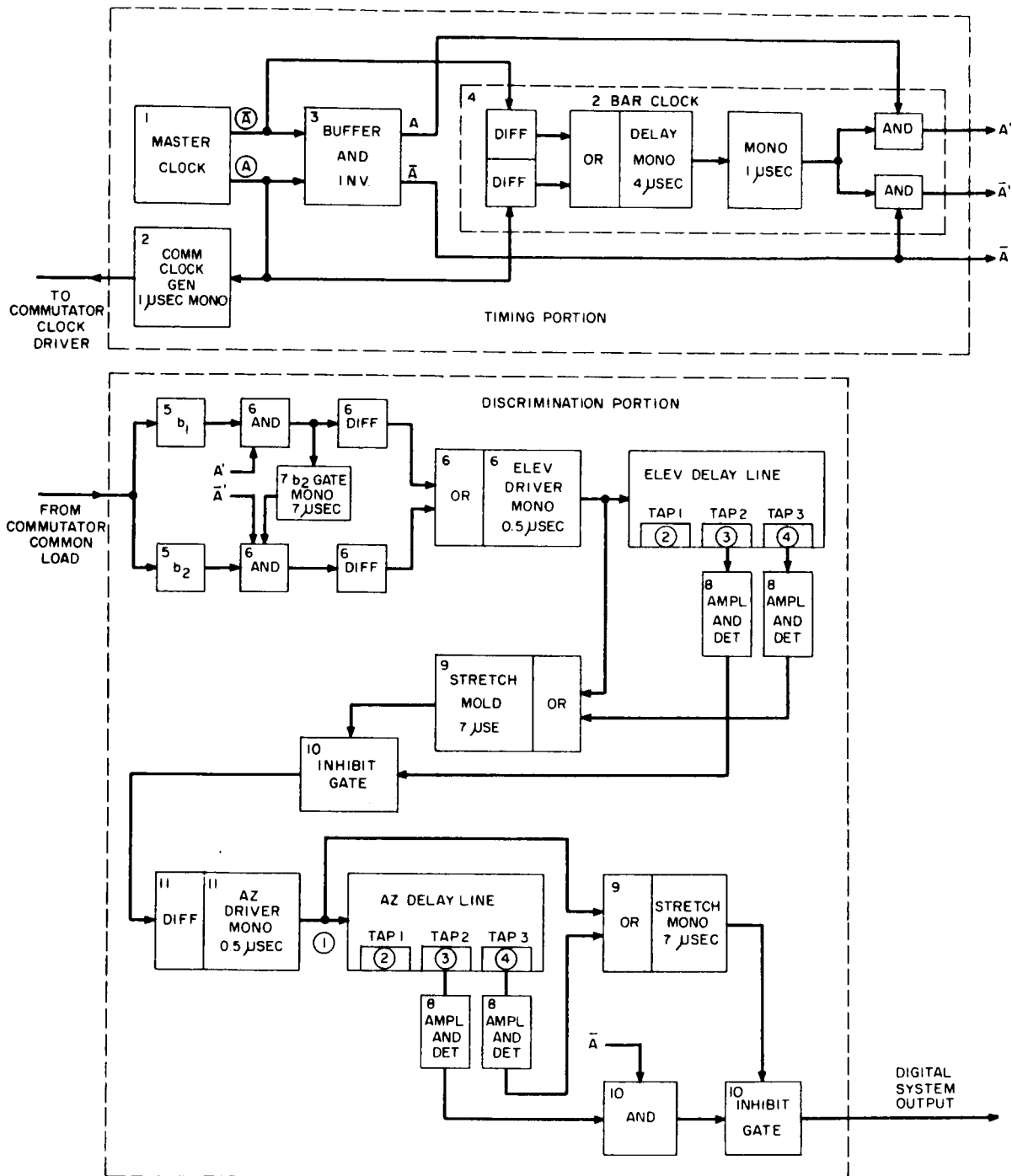


Figure 37. Commutator Timing Diagram

6.8 DELAY LINE LOGIC

6.8.1 Timing

The master clock generates a pair of complementary square wave trains which are labeled \textcircled{A} and $\textcircled{\bar{A}}$ on the block diagram in figure 38. The \textcircled{A} function is utilized to synchronize the commutator clock generator which generates a positive 1- μsec clock pulse for the purpose of synchronizing the



1982A-VB-30

Figure 38. Discrimination Circuit Block Diagram

commutator portion of the system. The positive edge of \textcircled{A} and $\textcircled{\bar{A}}$ are also utilized to successively synchronize a 4- μ sec delay monostable which in turn synchronizes a 1- μ sec monostable. The positive 1- μ sec pulse train contains two pulses per clock period and is logically combined via a separate AND gate with the functions A and \bar{A} for the purpose of obtaining two separate pulse trains. The two line outputs, A' and \bar{A}' are shown in the clock timing diagram (figure 39) where A' and \bar{A}' are shown coincident with A and \bar{A} respectively.

6.8.2 Discrimination

The commutated system output is dc coupled to the double threshold circuits b_1 and b_2 . The outputs from the threshold circuits are normalized output pulses generated whenever the signal is in excess of 3 times total system noise for b_1 and 6 times total system noise for b_2 . The b_1 normalized output is logically combined via an AND gate with A' from the two-bar clock. The output from this logic circuit is a pulse coincident in time with A' whenever the b_1 output pulse is present. The b_2 normalized output is logically combined via an AND gate with A' from the two-bar clock and an output from a gate mono which is activated for 7 μ sec each time that b_1 is present and logically combined with A' . This technique is utilized to obtain two bits of information per sample time with the imposed restriction that no b_2 information can be put into the elevation delay line in the absence of b_1 information. It should be mentioned at this point that b_1 and b_2 information could be obtained coincidentally in time and then separated for subsequent storage and processing, but the present method was adapted because it proved to be adequate and simpler to implement at the time of conception. The b_1 and b_2 information is then sent to the elevation delay line drive mono via an OR gate input. The drive mono generates a positive 0.5- μ sec pulse required to drive the sonic delay line used for elevation storage.

The outputs from tap 2, hereafter referred to as function 3, and the output from tap 3, hereafter referred to as function 4, are amplified and squared into 0.5- μ sec pulses, consistent with the logic levels required in the digital

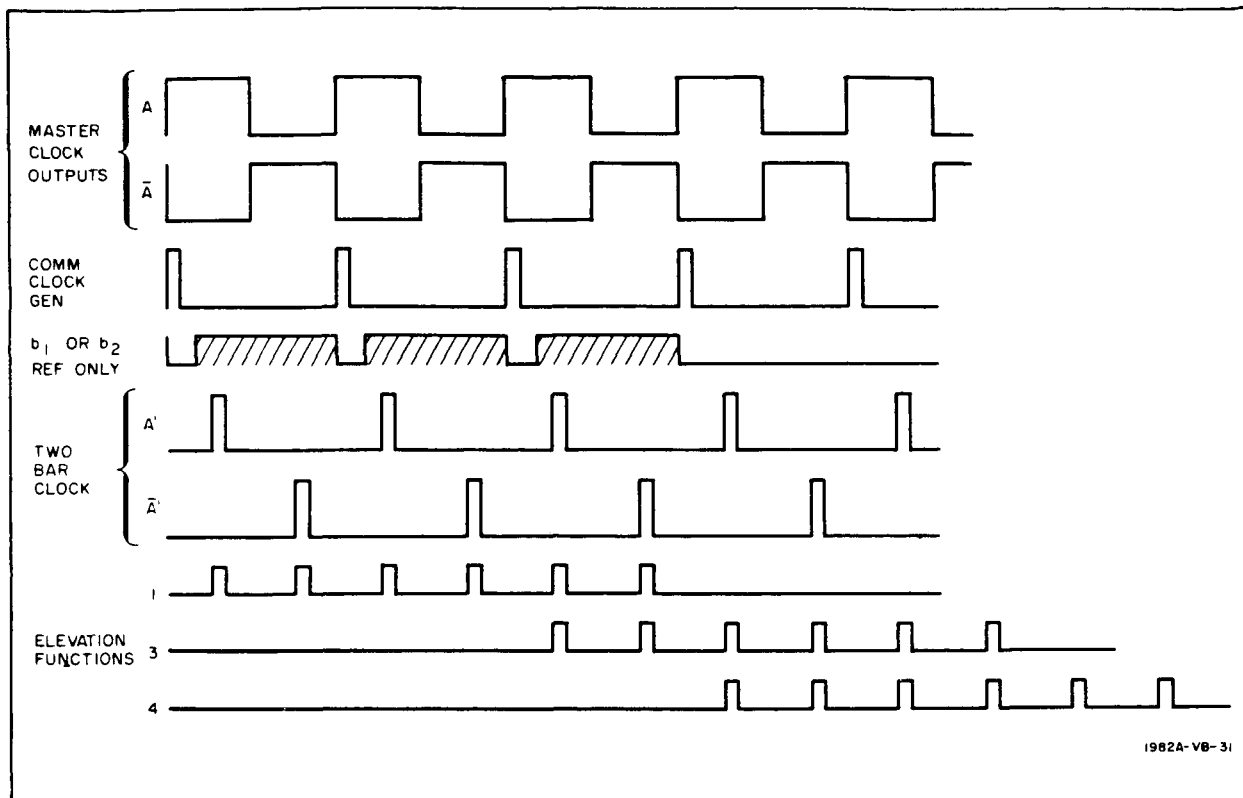


Figure 39. Timing Diagram of Logic Functions

processing circuitry under discussion. The input pulse to the elevation delay line, hereafter referred to as function 1, and function 4 are logically combined in an OR gate which activates a stretch mono of 7- μ sec duration. The stretch mono output and function 3 are dc coupled to the inhibit gate. Timing provisions are made for the b_1 information pulse to slip through the inhibit gate for subsequent use in the azimuth channel. The b_2 information is inhibited whenever time coincidence exists between the stretch mono outputs activated by functions 1 or 4, and b_2 outputs.

The information present after the inhibit gate is reconditioned by the azimuth drive mono for subsequent storage in the azimuth delay line consists of all b_1 information and only b_2 information which was previously accepted in elevation.

After the information is prepared for the azimuth delay line, a logical scheme, similar to that utilized in the elevation channel, is used. The bit

information rate appears at intervals prescribed by the A' and \bar{A}' two-bar clock functions, but the information pulse pattern is altered by the condition of b_2 elevation acceptance. The tapped outputs in the azimuth delay line are multiples of the clock period but are consistent with a dwell time in that 12 samples are made every dwell time. The difference that exists in the azimuth channel is the separation of accepted b_2 elevation information from the associated b_1 information that occurs within the same sample time. This function is accomplished via an AND gate which allows only the b_2 information to pass to the inhibit gate because it is coincident in time with \bar{A} . The b_2 information that was acceptable in the elevation channel and again in the azimuth channel appears at the output of the inhibit gate as an acceptable target. Figure 40 shows the discrimination circuit logic.

6.9 MISCELLANEOUS

Power supplies are purchased outside items. They are regulated 12, 9, and ± 6 volt dc supplies. This type of supply was found to be desirable in view of the low internal supply impedance required to provide sufficient low-frequency decoupling between channels.

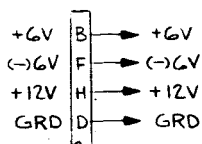
The display utilizes a laboratory type oscilloscope (not supplied with the engineering model). A sawtooth generator synchronized with the ring counter on the commutator is provided to generate an elevation sweep. The azimuth sweep derives its trigger from the microswitch attached to the turntable.

A wiring diagram of the power supply and sweep circuits is shown in figure 41.

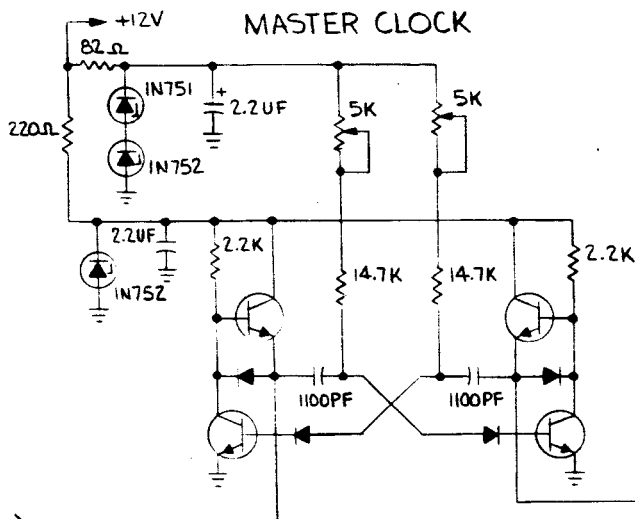
6.10 TIME RELATIONSHIPS

Turntable speed	=	33-1/3 rpm
Flat rotation angle	=	1/2 scan angle
Scan angle	=	60 degrees
Resolution	=	1 milliradian
Scan velocity	=	7 radians/second
Dwell time	=	143 microseconds

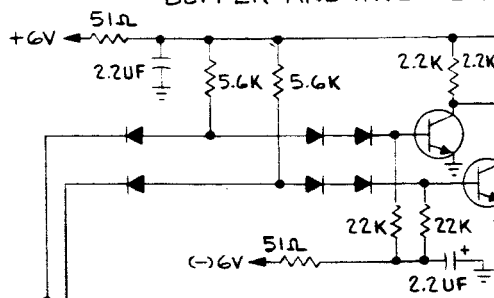
Sample time	=	11.9 microseconds
Commutation rate	=	84 kcp
Elevation delay	=	36 microseconds
Azimuth delay	=	430 microseconds



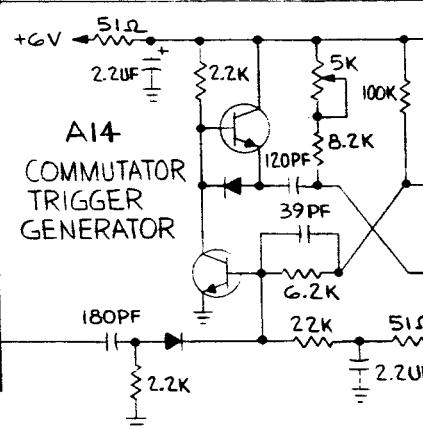
A1 MASTER CLOCK



A2 BUFFER AND INVERTER



A14 COMMUTATOR TRIGGER GENERATOR

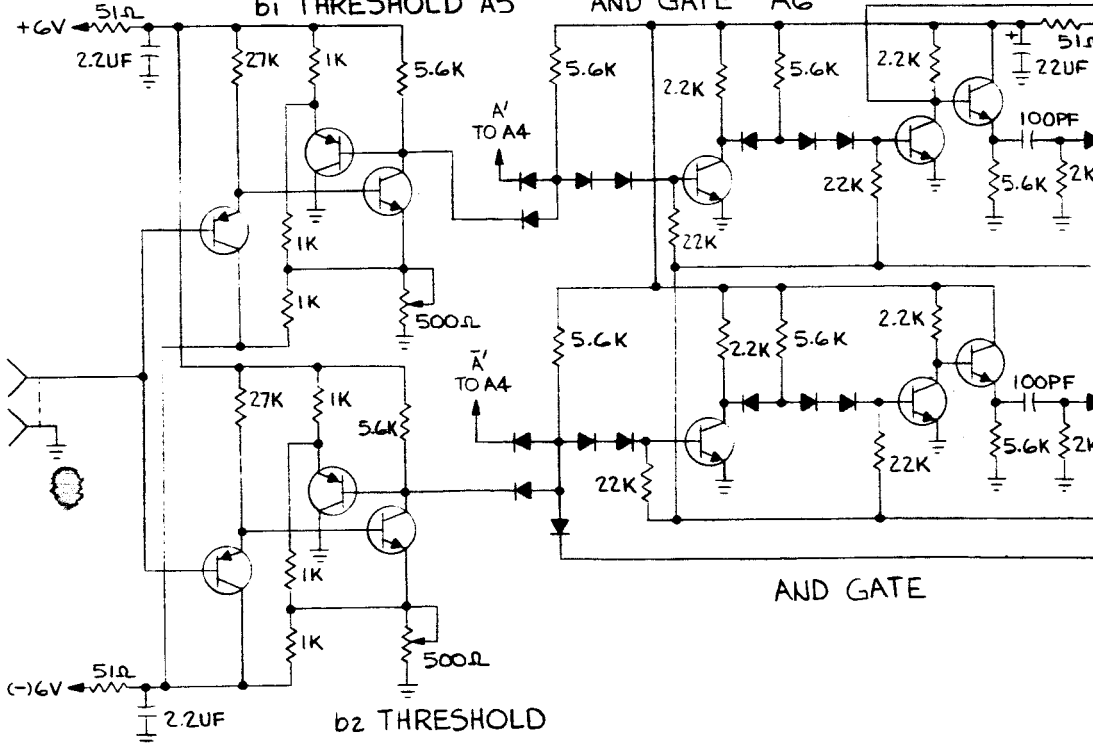


TO
COMMUTATOR
TRIGGER
DRIVER

b1 THRESHOLD A5

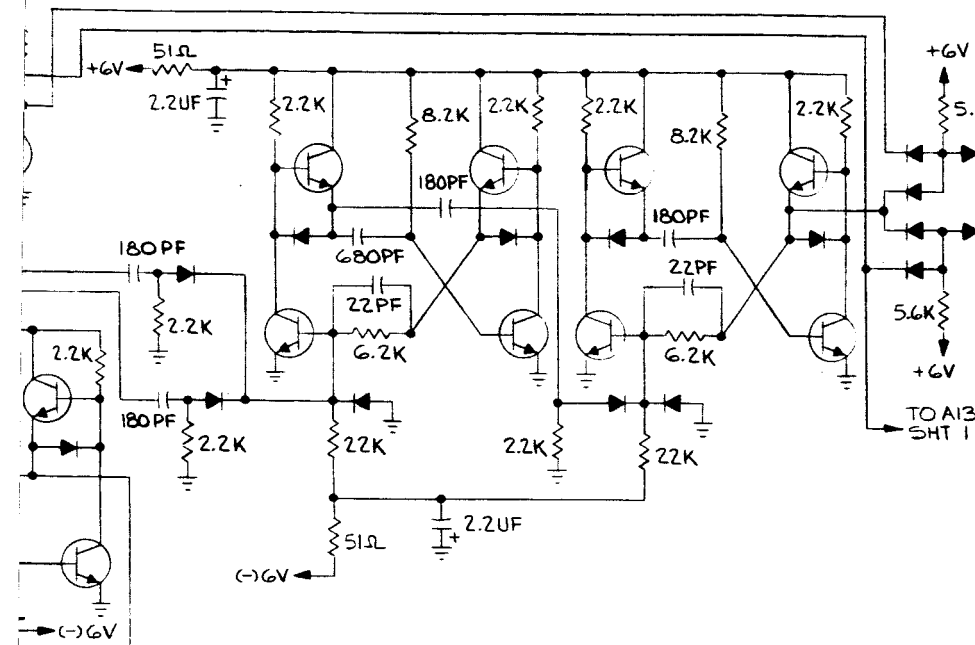
AND GATE A6

INPUT
FROM
COMMUTATOR

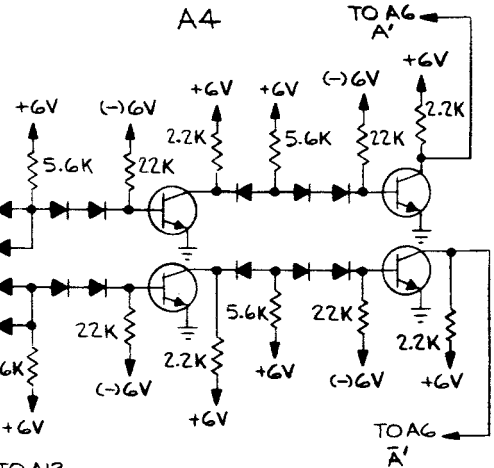


6-27-1

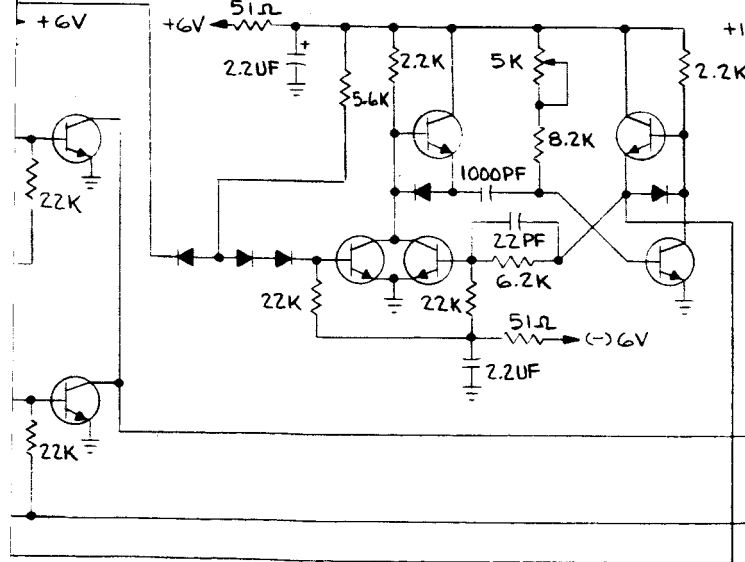
A3 TWO BAR CLOCK



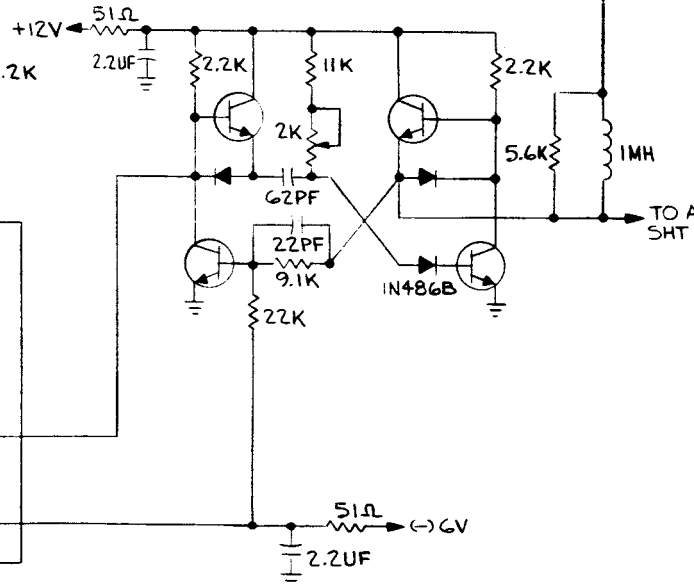
A4



A7 b2 GATE MONO

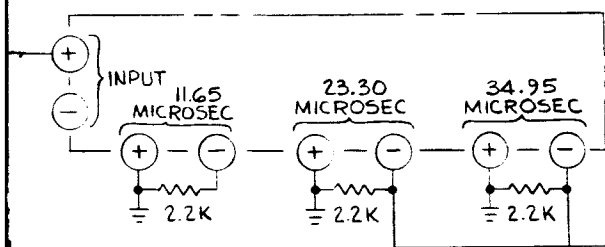


A8 .5 MICROSEC MONO

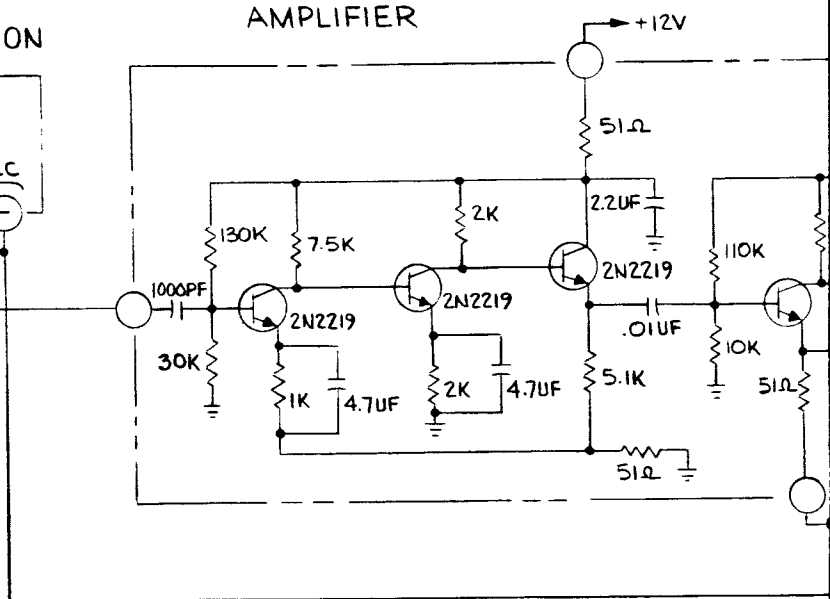


6-27-2

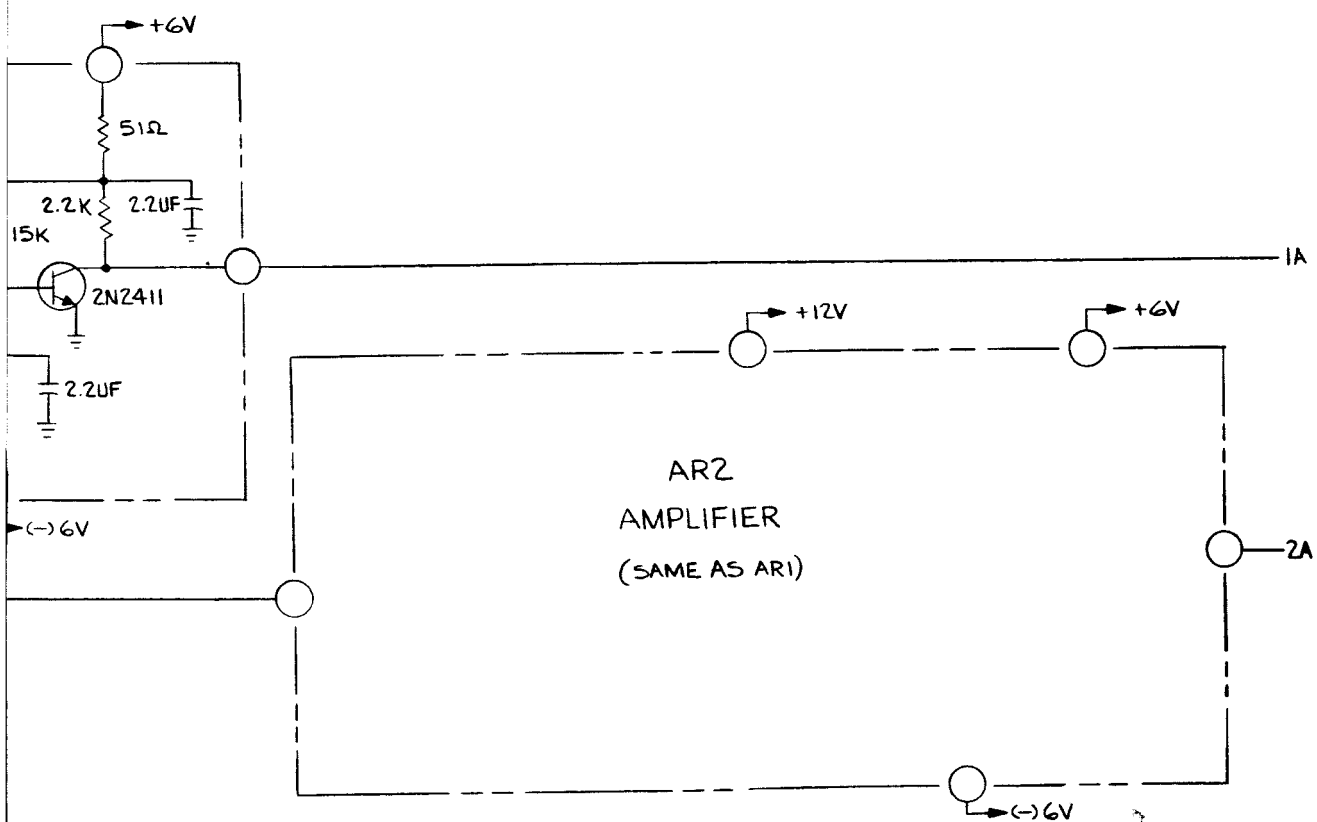
DLI
WIRESONIC DELAY LINE - ELEVATION



ARI
AMPLIFIER

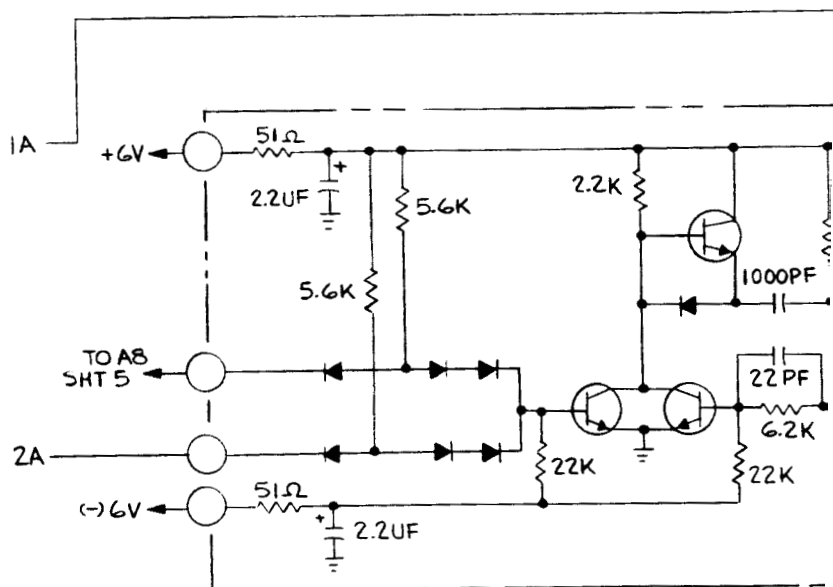


6-28-1



1982A-VH-29-A

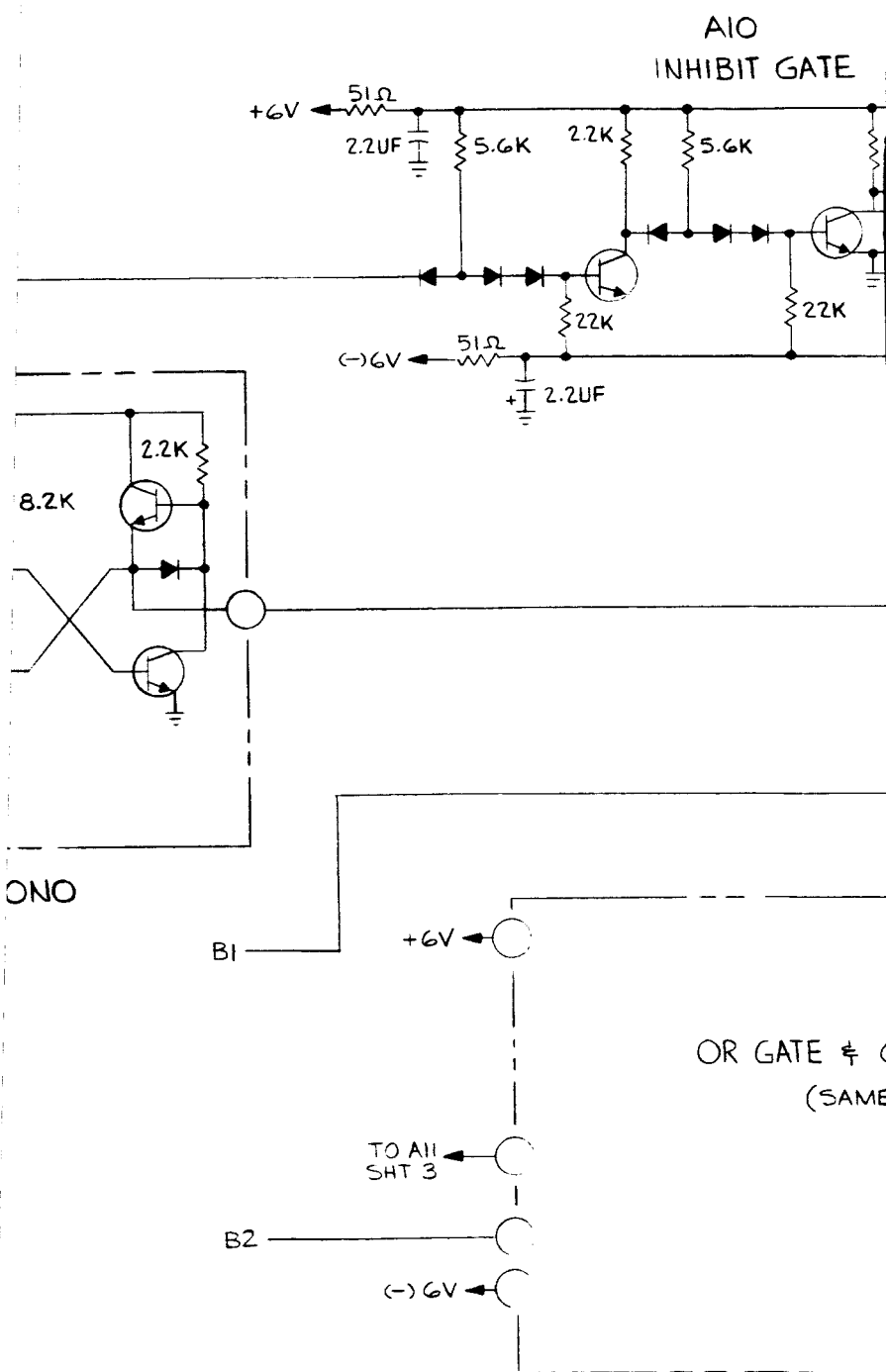
Figure 40. Discrimination Circuit Schematic (Sheet 1 of 2)



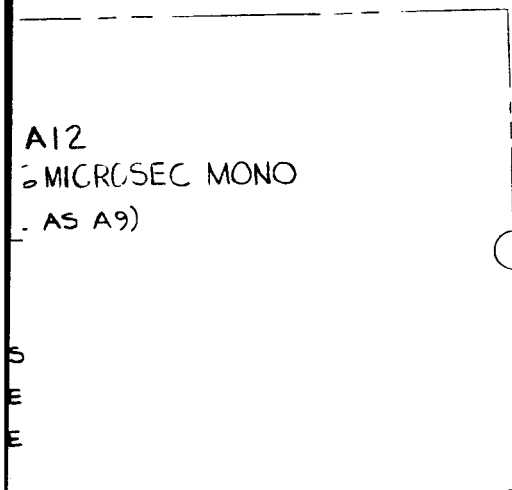
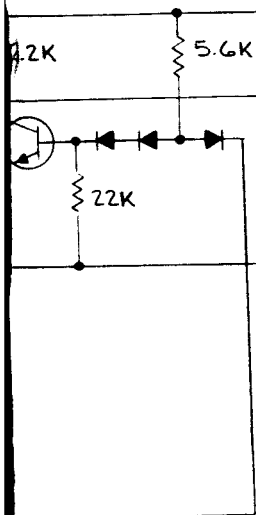
OR GATE & 6 MICROSEC M

A9

6-29-1

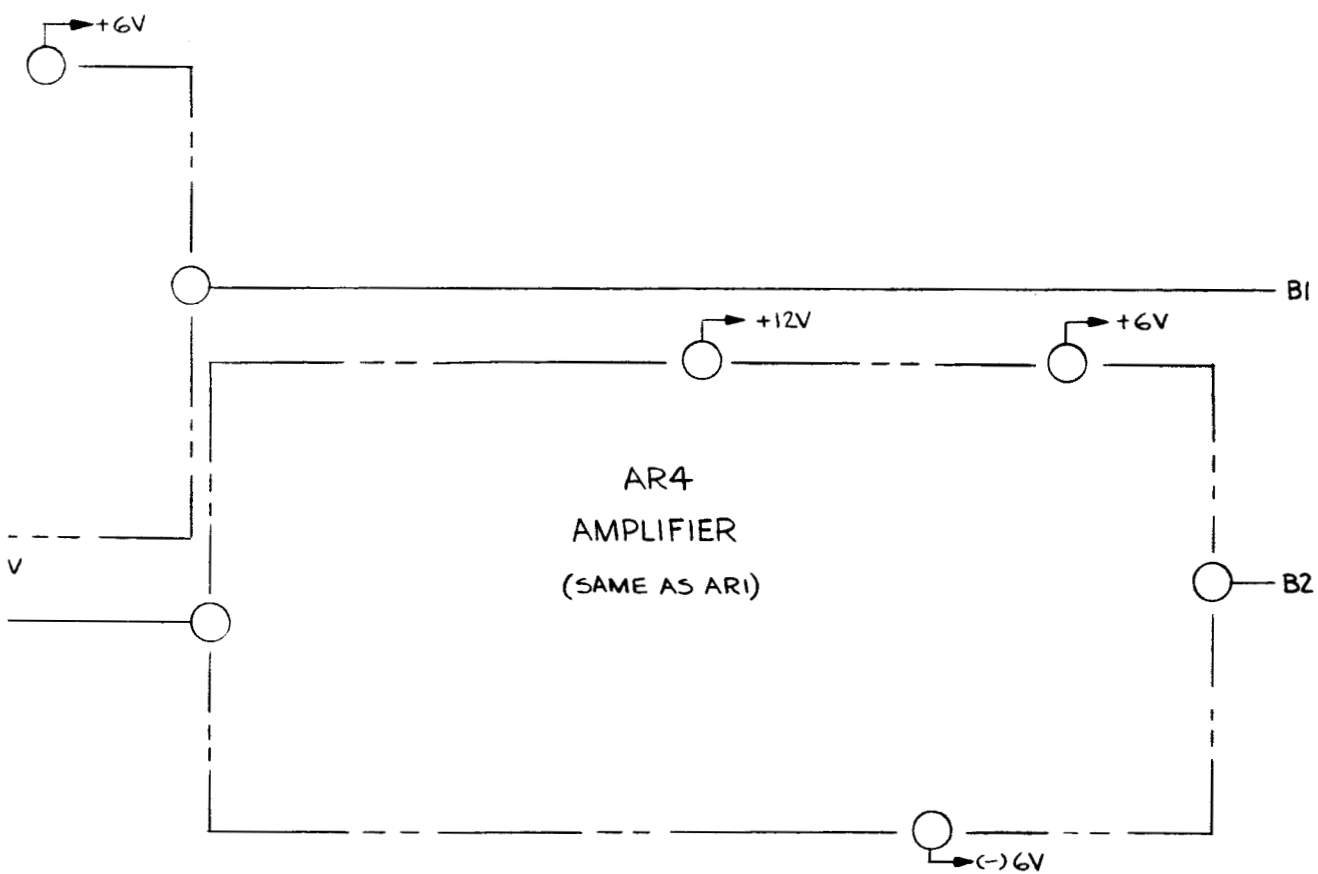


6-24-2



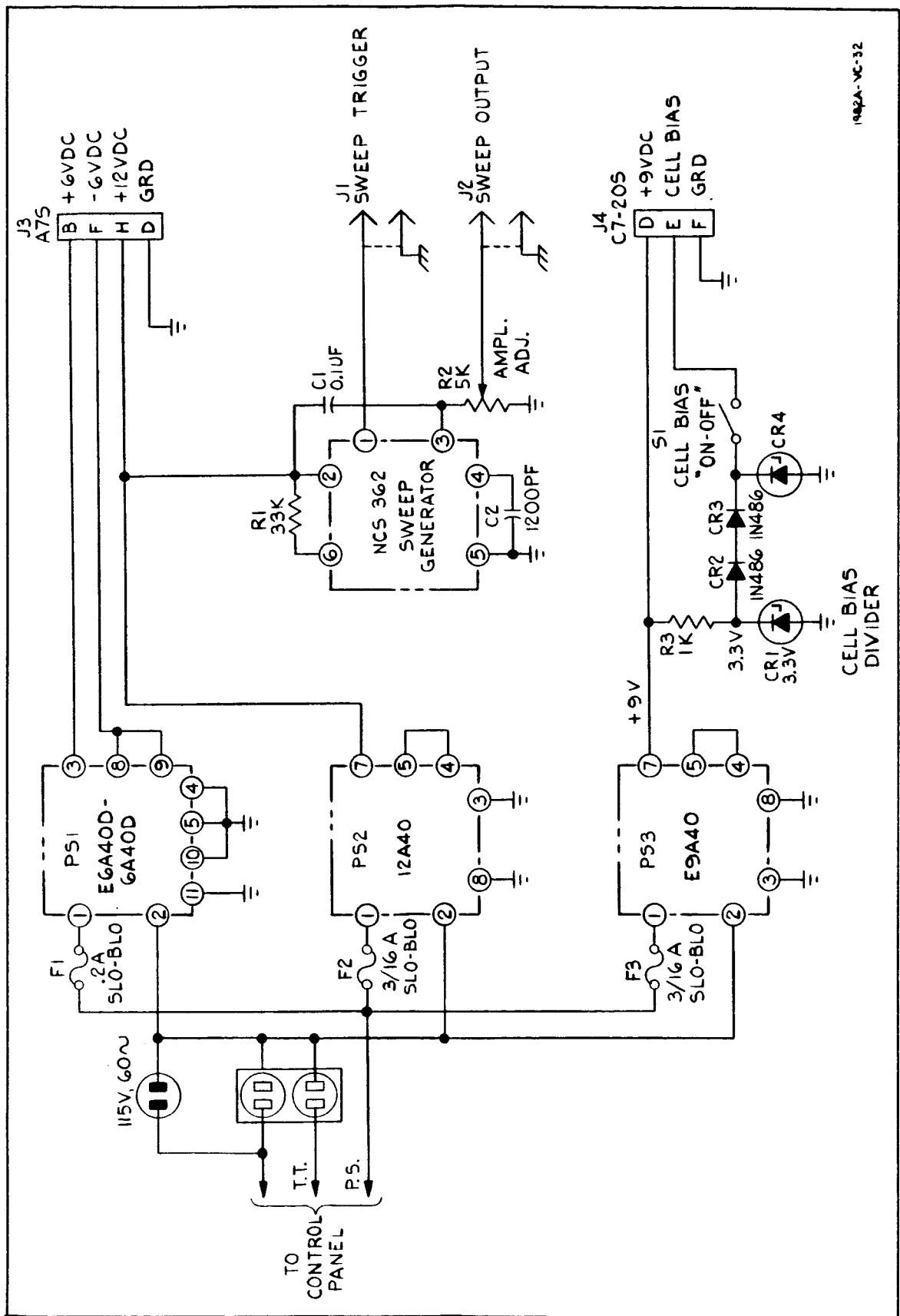
Q u e s t i o n s

- 6-29-3



1982A-VH-29-B

Figure 40. Discrimination Circuit Schematic (Sheet 2 of 2)



1002A-VC-32

Figure 41. Power Supply Wiring Diagram

7. PERFORMANCE

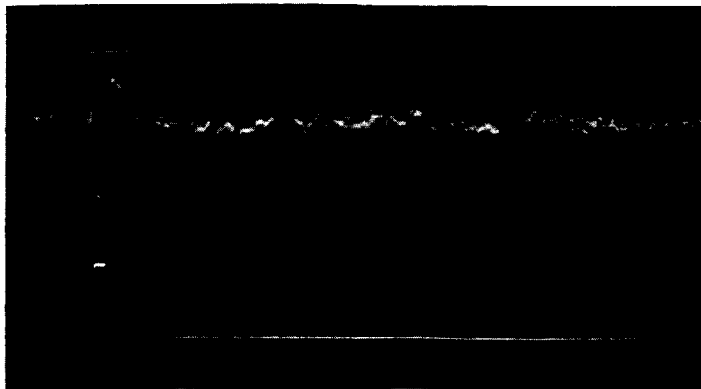
The laboratory performance of the feasibility model has been measured and found to reflect the desired design values. The noise equivalent sensitivity was found to be better than expected, primarily due to high detectivity detectors and better optical efficiency than used in the design predictions. Pertinent parameters evaluated are reported below.

7.1 RECOVERY TIME

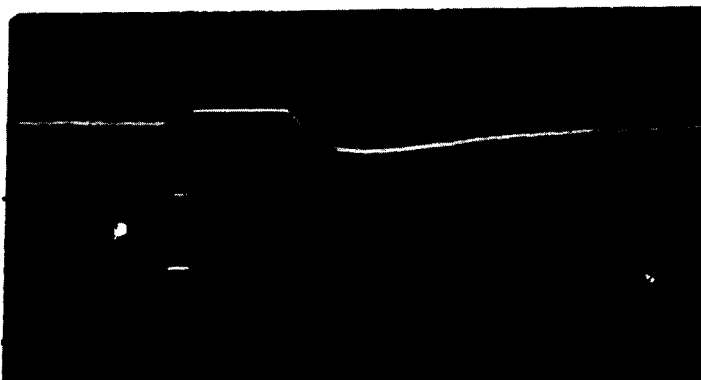
An evaluation of the amplifier recovery times as a function of large signal inputs was made. The results are discussed below.

Figure 42 illustrates this result. An extended area background signal is represented by a single square-wave 5 milliseconds in duration and 0.1 volt in amplitude in the top trace of figure 42. For a scan rate of 360 degrees per second this represents a cloud 1.8 degree wide, and with a detector noise level of 10 microvolts, this represents a background signal-to-noise ratio of 10^4 . The top trace of figure 42b represents a target 160 microseconds wide, which corresponds to the dwell time of a 1 milliradian detector on a point source with a 360 degree per second scan rate, and 200 microvolts amplitude, which gives a 20:1 S/N.

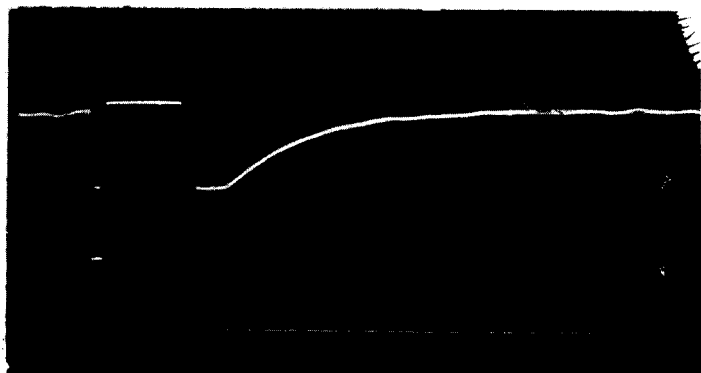
Both the target and the background simulated signals were fed into the preamplifier concurrently with the time displacement indicated by their respective positions in the top traces. The output is then recorded on the bottom trace of both 42a and 42b. (That is the target and background signals could not be recorded on the same trace because of the difference in amplitude, approximately 10^3 , therefore, they were recorded separately and the composite output signal was merely repeated with each separate recorded input.)



SWEEP: 1 msec/cm
 TOP TRACE: 1v/cm
 BOTTOM TRACE: 0.1mv/cm



SWEEP: 0.5 msec/cm
 TOP TRACE: 5v/cm
 BOTTOM TRACE: 10 mv/cm



SWEEP: 1 msec/cm
 TOP TRACE: 5v/cm
 BOTTOM TRACE: 1v/cm

1982A-PF-34

Figure 42. Large Signal Recovery Time

From left to right, the output signal is seen to consist of a large negative pulse (corresponding to the leading edge of the background signal) followed by a positive pulse (period where amplifier is blocked). The amplifier is seen to recover at the 5-millisecond point when the trailing edge of the background pulse drives the amplifier into saturation again. Recovery occurs about 5 milliseconds later where the target pulse is introduced.

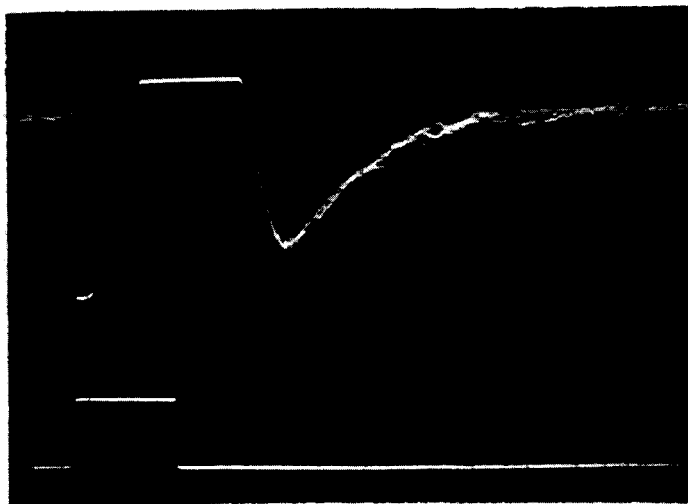
The significant features of this composite output signal are that the waveform due to the background transients (cloud edges) are broad compared to the target width thus facilitating discrimination by the background suppression circuits, and even though the background signal is some 3 orders of magnitude larger than the target, the target signal is readily identifiable at the output. This is made more evident in figure 42c where the target has been moved closer in time to the background signal.

Recovery of the amplifier from extended area targets is shown more vividly in the sequence of figure 48. Here the simulated background signal width is 1.5, 5, and 10 milliseconds respectively, (corresponding to 0.54, 1.8, and 3.6 degrees in space). Recovery is seen to be complete within 5 milliseconds or 2 degrees of a cloud edge for this maximum background S/N case, 10^4 . Recovery time is less for lower levels.

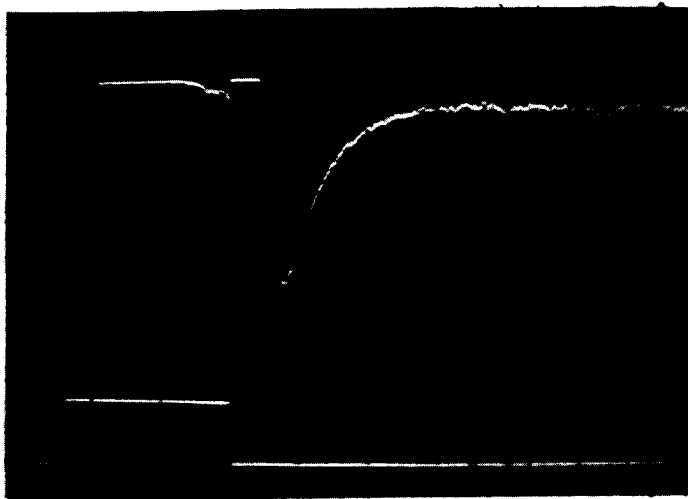
A target sequence is shown in figure 44 for S/N ratios of 10 to 10^5 . These results show that the target is not stretched over the dynamic range of signal. The amplifier is seen to require approximately 4 milliseconds to recover after the maximum target signal (approximately 1.5 degrees). The overshoot accompanying the recovery phenomenon is easily discriminated because of its width and will not reflect as a false target.

7.2 OPTICAL RESOLUTION

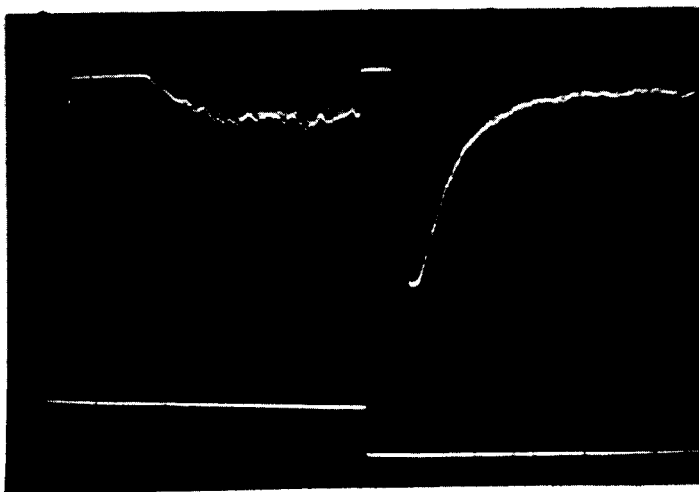
The 12-inch diameter F/1 parabola was tested by Tinsley Laboratories in the following manner with the given results.



SWEEP: 1 msec/cm
 TOP TRACE: 2v/cm
 BOTTOM TRACE: 0.1v/cm



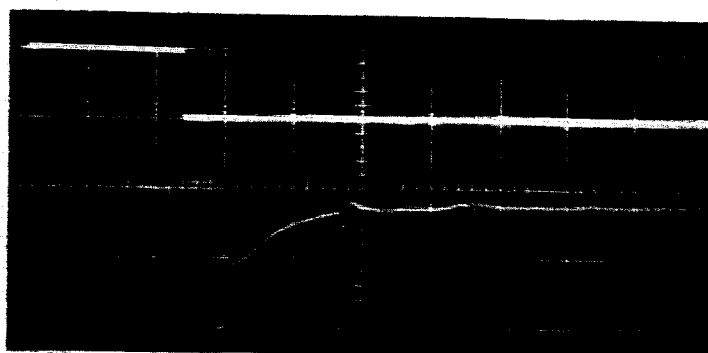
SWEEP: 2 msec/cm
 TOP TRACE: 2v/cm
 BOTTOM TRACE: 0.1v/cm



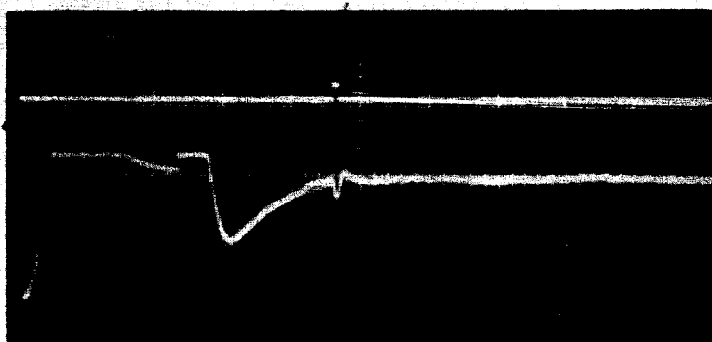
SWEEP: 2 msec/cm
 TOP TRACE: 2 v/cm
 BOTTOM TRACE: 0.1 v/cm

1982A-PF-35

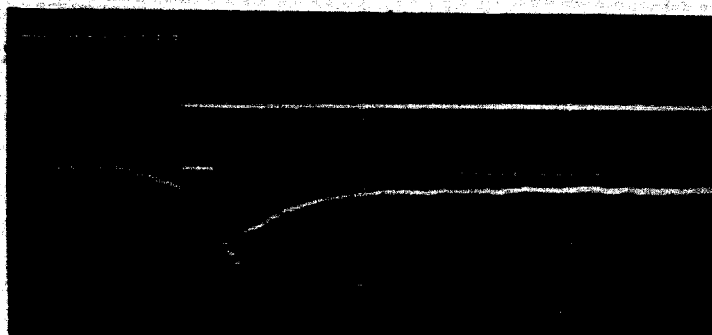
Figure 43. Extended Area Recovery Time



SWEEP: 2 msec/cm
 TOP TRACE: 1V/cm
 BOTTOM TRACE: 2V/cm



SWEEP: 2 msec/cm
 TOP TRACE: 1 mv/cm
 BOTTOM TRACE: 2 v/cm



SWEEP: 2 msec/cm
 TOP TRACE: 0.1v/cm
 BOTTOM TRACE: 2v/cm

1982A-PF-36

Figure 44. Target Stretching

A 2-watt Zirconium arc (0.005-inch diameter) was placed at the focus of a 12-inch diameter 72-inch focus collimating paraboloid. The parallel beam produced by the collimator was brought to a focus by the 12-inch diameter F/1 mirror. The ratio of the two focal lengths (72 and 12 inches) would make the theoretical image size just under 0.001 inch.

The tolerance of an on-axis blur circle diameter of 1.5 arc minutes equals 0.0052 inch diameter at 12 inches. Measurement of the actual blur circle diameter under the conditions stated above was approximately 0.007 inch. Allowing for image enlargement due to alignment errors, diffraction effects, etc. Tinsley feels that the mirror meets the tolerance of 1.5 arc minute diameter blur circle.

Independent caustic test of the mirror covering areas 0.2-inch wide at every 0.5 inch across a diameter confirm that the slope errors at these points do not exceed 22.5 arc seconds, the amount allowable to meet 1.5 arc minute blur circle diameter.

Westinghouse made similar tests on a 129-inch collimator using a 0.005 inch diameter pin hole aperture. The result was an image diameter of 0.010 inch or 0.8 milliradian which was maintained over a field of view of ± 5 milliradians.

This result is not in agreement with Tinsley's; however both are sufficient to satisfy the feasibility model requirements of 1 milliradian resolution.

7.3 DETECTOR

The following table summarized the characteristics measured on the three detectors procured for the feasibility model. Cell No. 2 is presently mounted in the system.

TABLE 3
DETECTOR CHARACTERISTICS

Cell No.	Element No.	Resistance (megohms)	Time Constant (μ secs)	Detectivity 10^{10} $D^* (\lambda_{\max} 90, 1)$
2	1	0.11	50	3.94
	2	0.11	35	3.94
	3	0.10	35	4.26
	4	0.095	35	4.05
	5	0.11	35	3.40
	6	0.12	35	3.17
	7	0.11	35	3.54
	8	0.095	35	3.70
	9	0.090	35	3.40
	10	0.13	35	3.54
5	1	0.300	50	3.52
	2	0.200	50	3.27
	3	0.180	50	3.46
	4	0.180	35	2.93
	5	0.190	35	3.54
	6	0.520	35	3.04
	7	0.160	50	2.94
	8	0.170	50	2.56
	9	0.140	50	2.72
	10	0.130	50	2.52
7	1	0.160	60	3.80
	2	0.120	50	3.56
	3	0.120	60	3.56
	4	0.140	50	3.92
	5	0.110	50	3.96

TABLE 3 (Continued)

Cell No.	Element No.	Resistance (megohms)	Time Constant (μ secs)	Detectivity $\times 10^{10}$ $D^* (\lambda_{\max}^{90, 1})$
7	6	0.130	60	3.80
	7	0.130	50	3.18
	8	0.130	50	3.68
	9	0.130	50	3.80
	10	0.130	50	4.17

7.4 SENSITIVITY

The sensitivity of one element selected at random was measured by chopping at the source with the scanner turntable stopped.

a. Test conditions:

Black-body temperature, T = 500°K
 Distance, D = 920 inches
 Aperture diameter, d = 1/16 inch
 Chopping frequency, f = 2 kc

b. Measurements:

Detector element = #6
 Signal, S = 850 mv rms
 Noise, N = 103 mv rms

c. Calculations:

$$\text{Effective flux density} = H_{\text{rms}} = \frac{\sigma \epsilon T^4}{4} \left[\frac{d}{D} \right]^2 0.45 CF \text{ w/cm}^2 \text{ rms}$$

$$\text{Noise equivalent sensitivity} = \phi_c = \frac{H_{\text{rms}}}{S/N} \text{ w/cm}^2$$

where: σ = Stefan Boltzmann constant $\approx 5.7 \times 10^{-12} \text{ w/cm}^2/\text{deg}^4$

ϵ = Emissivity (assumed to be unity)

CF = Correlation factor (\approx percent black-body radiation within system spectral response) 0.01

0.45 = RMS component of square wave flux

d. Results:

$$H_{\text{rms}} = \frac{0.36}{4} \left[\frac{0.063}{920} \right]^2 \times 0.01 \times 0.45 = 1.85 \times 10^{-12} \text{ w/cm}^2$$

$$S/N = \frac{0.850}{0.103} = 8.25$$

$$\phi_c = \frac{1.85 \times 10^{-12}}{8.25} = 2.24 \times 10^{-13} \text{ w/cm}^2$$

The sensitivity of this same element was then measured by scanning the source.

a. Test conditions:

Same as above except no chopper and the turntable operating.

b. Measurements:

Detector element = #6

Signal, \hat{S} = 2.25 V_{peak}

Noise, N = 103 mv/rms

c. Calculations:

$$\text{Effective flux density} = H = \frac{\epsilon \sigma T^4}{4} \left[\frac{d}{D} \right]^2 \text{ CF w/cm}^2$$

$$\text{Noise equivalent sensitivity } \phi_s = \frac{H}{\frac{\hat{S}}{S/N}} \text{ w/cm}^2$$

d. Results:

$$H = \frac{0.36}{4} \left[\frac{0.063}{920} \right]^2 \times 0.01 = 4.1 \times 10^{-12} \text{ w/cm}^2$$

$$\frac{\hat{S}}{S/N} = \frac{2.25}{0.103} = 21.8$$

$$\phi_s = \frac{4.1 \times 10^{-12}}{21.8} = 1.89 \times 10^{-13} \text{ w/cm}^2$$

The relative sensitivity of the remaining elements was measured scanning, using element 6 as a reference. This distribution and corresponding sensitivities are listed on the next page:

Detector Element	Relative Sensitivity	Absolute Sensitivity x 10^{-3} (w/cm ²)
1	0.835	1.58
2	1.05	1.97
3	0.835	1.58
4	0.835	1.58
5	1.120	2.12
6	1.000	1.89
7	0.835	1.58
8	0.575	1.09
9	1.12	2.12
10	1.31	2.48

7.5 OPTICAL CROSSTALK

Optical resolution measurements showed the blur circle size to be less than 1 milliradian. However, these measurements were made at infinity, which of course reflects the situation in the system application. However for laboratory tests of the discrimination functions, it is desirable to focus at some near range. Unfortunately, the blur circle increases when focusing the parabola at other than infinity. Tests show that about 80 feet is the minimum distance one can focus these optics and still maintain a blur circle less than 1 milliradian.

The optical crosstalk between adjacent channels was measured chopping at the source under these conditions and the results show less than 1/2 percent crosstalk. This is expected to be even less when focused at infinity.

7.6 DELAY LINE DISCRIMINATION

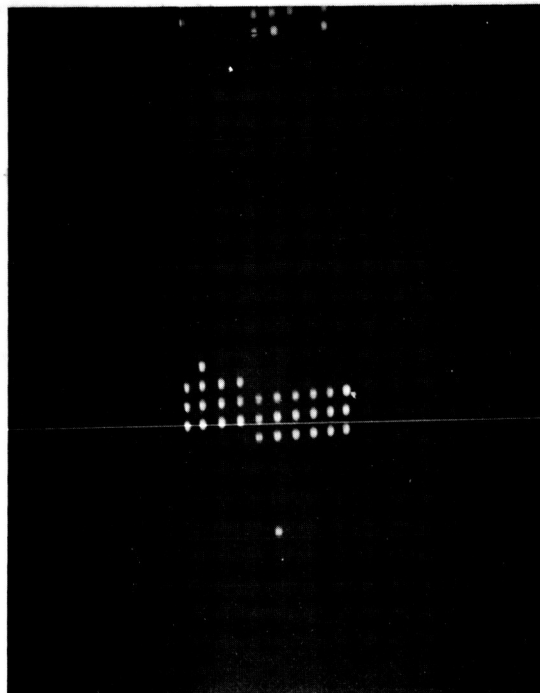
The delay line discrimination circuits have been tested using ideal waveforms from laboratory function generators and perform their desired logic functions.

Some simulated extended area targets have also been scanned in the laboratory and successfully rejected. All vertical and horizontal lines and large extended areas were completely rejected.

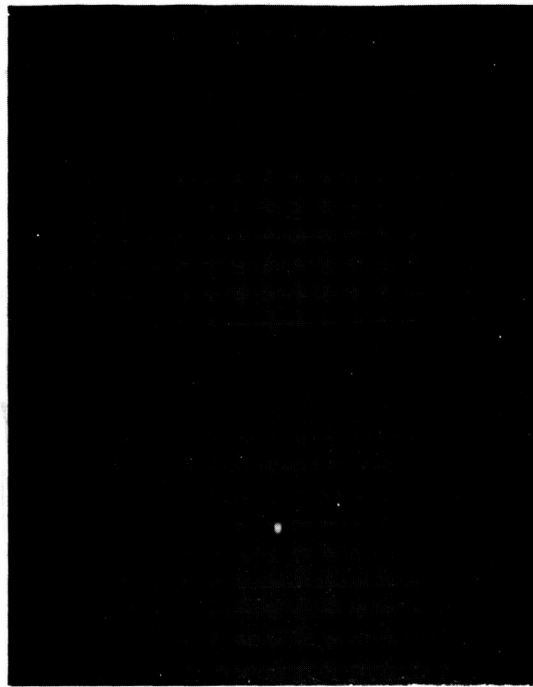
Figure 45 shows the result of scanning an extended area target with and without the delay line discrimination. The extended area source used here was a 1-square-foot black-body source which subtended an angle of approximately 15 milliradians. Just to one side of the extended area source was placed a point-source target. The result without discrimination is shown in figure 45a. Here the return from the extended area source is seen to illuminate all 10 elements in elevation. The low-frequency droop only holds the signal up for three to four dwell times. Some amplifier overshoot, resulting from the opposite polarity signal generated when leaving the extended area source, is seen at the extreme right of the photograph. Just preceding the extended area the point source is seen on the left. Figure 45b shows the result when the discrimination circuits are added. The extended area source as well as the overshoot are completely rejected. Only the point source appears.

Figure 46 shows the results of using a more exotic target shape, the letter W. The result without discrimination is shown in figure 46a. Figure 46b shows the result with discrimination. The point source target is seen in both figures. This particular pattern gave rise to an occasional false target from within the W. One such case was selected for printing to illustrate this result. The percentage of rejection is estimated to be better than 99 percent based on the average number of elements making up the W that are rejected.

These cursory tests indicate that the discrimination circuit functions are operating properly. The technique is ready for evaluation against real sky backgrounds, however, this is beyond the scope of this contract.



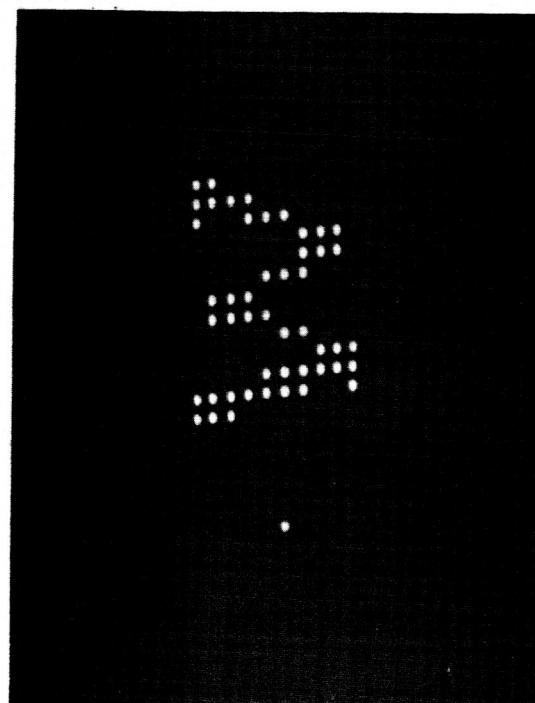
a. WITHOUT DISCRIMINATOR



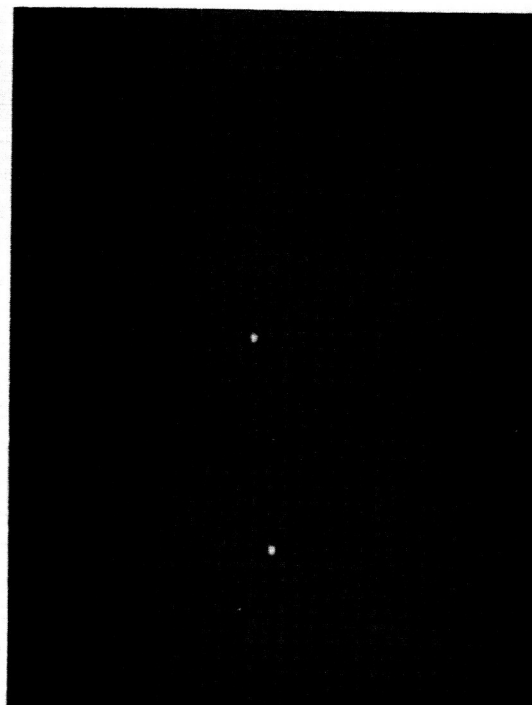
b. WITH DISCRIMINATOR

1982A-PF-37

Figure 45. Extended Area Target



a. WITHOUT DISCRIMINATOR



b. WITH DISCRIMINATOR

1982A-PF-38

Figure 46. Exotic Target

8. NEW TECHNOLOGY

The new technology developed under this contract consisted of implementing a proprietary two-dimensional space filtering background suppression concept employing electronic delay lines.

The original concept was disclosed on a patent disclosure prior to the award of this contract. However, it had heretofore never been applied in practice. During the course of this contract the scheme was implemented and several improvements incorporated.

Much of the text in this final report describes this new technique. Rather than reiterate here, the sections of this report pertinent to this new technology are listed below.

4.5	SPATIAL DISCRIMINATION
4.6	DIGITAL SPACE CORRELATION
5.1	DELAY LINE DISCRIMINATION
5.2	THRESHOLD LEVELS
5.3	ELECTRONIC FILTER
6.8	DELAY LINE LOGIC
7.7	DELAY LINE DISCRIMINATION

9. REFERENCES

1. Plotkin, H.H., Infrared Re-entry Tracking; NASA report X-524-62-136, August 10, 1962.
2. Lehnert, R. and Rosenbaum, B., Plasma Effects on Apollo Re-entry Communications; NASA report X-513-64-8, January 1964.
3. Vonbun, F.O., Re-entry Tracking for Apollo; NASA report X-513-64-85, March 1964.
4. Little, B.H., Jr., Aerodynamic Heating for Lunar Re-entry Vehicles; Vol XI, Advances in the Astronautical Sciences, American Astronautical Society, 1963, pp. 767-797.
5. Lees, L., Recovery Dynamics-Heat Transfer at Hypersonic Speeds in a Planetary Atmosphere; Chapter XII, Space Technology, John Wiley & Sons Inc., New York 1959.
6. Page, W.A., Shock-layer Radiation of Blunt Bodies Traveling at Lunar Return Entry Velocities; IAS Paper No 63-41, Institute of the Aerospace Sciences, January 1963.
7. Kivel, B., Radiation from Hot Air and Its Effect on Stagnation-Point Heating; Journal of the Aerospace Sciences, February 1961, pp. 96-102.
8. Meyerott, R.E. and Sokoloff, J., Absorption Coefficients of Air; Geophysical Research Papers No 68, ARDC, Bedford, Mass., AD 252003.
9. Wentink, T. Jr., Planet, W.; Hammerling, P. and Kivel, B., Infrared Continuum Radiation from High-Temperature Air; Journal of Applied Physics, Vol 29, No. 4, April 1958, pp. 742-743.
10. Kivel, B. and Bailey, K., Tables of Radiation from High Temperature Air; AVC Research Laboratory, Research Report 21, AD 212014.
11. Craig, R.A. and Davey, W.C., Thermal Radiation from Ablation Products Injected into a Hypersonic Shock Layer; NASA report TND-1978, September 1963.

12. Altshuler, T.L., Infrared Transmission and Background Radiation by Clear Atmospheres; General Electric Technical Information Series, Report No 61SD199, December 1, 1961, AD 401923.
13. Murcray, D.G.; Murcray, F.H. and Williams, W.J., Variation of the Infrared Solar Spectrum between 2800 and 5100 cm^{-1} with Altitude; Journal of the Optical Society of America, Vol 54, No. 1, January 1964, pp. 23-27.
14. Jones, R.A., Measured Heat Transfer and Pressure Distributions on the Apollo Face at a Mach Number of 8 and Estimates for Flight Conditions; NASA report TMX-919, April 1964. Confidential.
15. Walters, E.E., Free-Flight Measurements of Radiative Heating to the Front Face of Apollo Reentry Capsule as a Function of Angle of Attack; NASA report TMX-851, February 1964. Confidential.
16. Petritz, R.L., Theory of Photoconductivity in Semiconductor Films; Physical Review, Volume 104, No. 6, December 15, 1956.
17. Bratt, P., Engeler, W., Levinstein, H., Mac Rae, A. and Pehek, J., A Status Report on Infrared Detectors; Infrared Physics, Volume 1, 1961, pp. 27-38.
18. Vandehei P.T. and Taylor B.J., Spectral Ground and Sky Backgrounds; GRD Research Notes No 46, November 1960, pp. 187-211.
19. Duntley, S.Q., Boilean, A., Gorden, J. and Harris, J.L., Maps of Sky Luminance at Various Altitudes; GRD Research Notes No. 46, November 1960, pp. 180-186.
20. Higby, R.F., The Relationship Between Probability of Detection and Infrared Surveillance System Sensitivity; SDTM No. 266, Westinghouse, Aerospace Division, September 1963.
21. Higby, R.F., Evaluation of the S/N Enhancement Factor Γ for Point Detection by the Scanning Infrared Surveillance System; SDTM No. 276, Westinghouse, Aerospace Division, November 1963.
22. Adkins, Harold, Relays, Remote Switching and Commutating Devices; Military Systems Designs (Periodical) Vol. 7, No. 3, June 1963.
23. Higby, R.F., Derivation of the General Equation for Predicted Infrared Surveillance System Sensitivity; SDTM No. 245, Westinghouse, Aerospace Division, August 1963.

10. SYMBOL GLOSSARY

A	= Area of source, cm^2
D_λ	= Detector spectral response
H	= Irradiance, w/cm^2
J	= Radiant intensity, w/ster
Q_B	= Background photon flux density, $\text{photons/cm}^2 - \text{sec}$
R	= Slant Range, km
R_o	= Nose radius, feet
T_{eq}	= Equilibrium temperature, $^\circ\text{K}$
T_{ST}	= Stagnation temperature, $^\circ\text{K}$
T_λ	= Atmospheric transmission
W_λ	= Radiant emittance, w/cm^2
η_λ	= Quantum efficiency
P	= Stagnation density, slugs/ft^3
P_o	= Atmospheric density, slugs/ft^3
P_∞	= Free stream density, slugs/ft^3
\dot{q}_c	= Convective heating rate, w/cm^2
\dot{q}_r	= Radiative heating rate, w/cm^2
u_∞	= Free stream velocity, feet/sec
\dot{q}_a	= Ablation product radiation heating rate, w/cm^2
α	= Elevation look angle, deg
\mathcal{E}	= Emissivity
δ_e	= Excitation distance
δ_r	= Relaxation distance
δ_s	= Shock stand off distance
σ	= Stefan - Boltzman constant, $5.7 \times 10^{-12} \text{ w/cm}^2 - \text{deg}^4$
λ	= Wavelength, microns

S = Ground range
 θ = Angle subtended at Earth's center by target and observer, radians
 r_e = Radius of Earth
 h_o = Altitude of observer
 h_t = Altitude of target